UC Berkeley
UC Berkeley Electronic Theses and Dissertations

Title
Atomic Parity Violation and Related Physics in Ytterbium

Permalink
https://escholarship.org/uc/item/6tx331dx

Author
Dounas-Frazer, Dimitri Robert

Publication Date
2012

Peer reviewed|Thesis/dissertation

eScholarship.org Powered by the California Digital Library
University of California

Atomic Parity Violation and Related Physics in Ytterbium

by

Dimitri Robert Dounas-Frazer

A dissertation submitted in partial satisfaction of the
requirements for the degree of
Doctor of Philosophy

in

Physics

in the

Graduate Division

of the

University of California, Berkeley

Committee in charge:

Professor Dmitry Budker, Chair
Professor Hartmut Häffner
Professor Robert Harris

Fall 2012

Atomic Parity Violation and Related Physics in Ytterbium

Copyright 2012
by
Dimitri Robert Dounas-Frazer

Abstract

Atomic Parity Violation and Related Physics in Ytterbium

by

Dimitri Robert Dounas-Frazer

Doctor of Philosophy in Physics

University of California, Berkeley

Professor Dmitry Budker, Chair

Atomic parity violation has been observed in the 408 nm $6s^2\,{}^1S_0 \to 5d6s\,{}^3D_1$ forbidden transition of ytterbium. The parity-violating amplitude is $8.7(1.4) \times 10^{-10}\ ea_0$, two orders of magnitude larger than in cesium, where the most precise experiments to date have been performed. This is in accordance with theoretical predictions and constitutes the largest atomic parity-violating amplitude yet observed. This also opens the way to future measurements of neutron skins and anapole moments by comparing parity-violating amplitudes for various isotopes and hyperfine components of the transition.

We present a detailed description of the observation. Linearly polarized 408 nm light interacts with ytterbium atoms in crossed electric ($\mathbf{E}$) and magnetic fields ($\mathbf{B}$). The probability of the $6s^2\,{}^1S_0 \to 5d6s\,{}^3D_1$ transition contains a parity-violating term, proportional to $(\boldsymbol{\mathcal{E}} \cdot \mathbf{B})[(\boldsymbol{\mathcal{E}} \times \mathbf{E}) \cdot \mathbf{B}]$, arising from interference between the amplitudes of transitions induced by the electroweak interaction and the Stark effect ($\boldsymbol{\mathcal{E}}$ is the optical electric field). The transition probability is detected by measuring the population of the metastable $6s6p\,{}^3P_0$ state, to which 65% of the atoms excited to the $5d6s\,{}^3D_1$ state spontaneously decay. The population of the $6s6p\,{}^3P_0$ state is determined by resonantly exciting the atoms with 649 nm light to the $6s7s\,{}^3S_1$ state and collecting the fluorescence resulting from its decay. Systematic corrections due to imperfections in the applied electric and magnetic fields are determined in auxiliary experiments. The statistical uncertainty is dominated by parasitic frequency excursions of the 408-nm excitation light due to imperfect stabilization of the optical reference with respect to the atomic resonance. The present uncertainties are 9% statistical and 8% systematic. Methods of improving the accuracy for the future experiments are discussed.

We further present a measurement of the dynamic scalar and tensor polarizabilities of ytterbium's $5d6s\,{}^3D_1$ state. The polarizabilities were measured by analyzing the spectral lineshape of the $6s^2\,{}^1S_0 \to 5d6s\,{}^3D_1$ transition. Due to the interaction of atoms with the standing wave, the lineshape has a characteristic polarizability-dependent distortion. A theoretical model was used to simulate the lineshape and determine a combination of the polarizabilities of the ground and excited states by fitting the model to experimental data. This combination was measured with a 13% uncertainty, only 3% of which is due to uncertainty

in the simulation and fitting procedure. By comparing two different combinations of polarizabilities, the scalar and tensor polarizabilities of the state $5d6s\,^3D_1$ were measured to be $\alpha_0(^3D_1) = 0.151(36)$ Hz $\cdot$ (V/cm)$^{-2}$ and $\alpha_2(^3D_1) = -0.205(53)$ Hz $\cdot$ (V/cm)$^{-2}$, respectively. We show that this technique can be applied to similar atomic systems.

Finally, we propose two methods for improving future measurements of atomic parity violation using two-photon transitions. The first method is characterized by the absence of static external electric and magnetic fields. Such measurements can be achieved by observing the interference of parity-conserving and parity-violating two-photon transition amplitudes between energy eigenstates of zero electronic angular momentum. General expressions for induced two-photon transition amplitudes are derived. The two-photon scheme using the $6s^2\,^1S_0 \rightarrow 6s6p\,^1P_1 \rightarrow 6s6p\,^3P_0$ transition in ytterbium ($\lambda_1 = 399$ nm, $\lambda_2 = 1280$ nm) is proposed as a crosscheck of the APV experiment which uses the single-photon 408 nm $6s^2\,^1S_0 \rightarrow 5d6s\,^3D_1$ transition. We estimate that the signal-to-noise ratio of the proposed experiment is comparable to that achieved in the 408 nm system.

The second method allows for measurement of nuclear spin dependent atomic parity violation without nuclear spin independent background. Such measurements can be achieved by driving parity-violating two-photon $J = 0 \rightarrow 1$ transitions driven by identical photons in the presence of an external static magnetic field. We discuss two promising applications: the 462 nm $5s^2\,^1S_0 \rightarrow 5s9p\,^1P_1$ transition in strontium-87, and the 741 nm $7s^2\,^1S_0 \rightarrow 7s7p\,^3P_1$ transition in unstable radium-225.

To my brother, Alexi,
for being a constant reminder that there are things in life more important than physics.

Contents

List of Figures

List of Tables

Acknowledgments

When I started grad school at Berkeley in 2007, the Physics Department was still in the habit of administering two sets of preliminary exams: written exams and oral ones. They were tough, but the Colorado School of Mines prepared me well enough that I passed them all on the first try. I sent a jubilant email to several CSM faculty and staff thanking them for being such great teachers and mentors, so I won't list them all by name here; instead, I'll just acknowledge the wonderful education I received at CSM.

The preliminary exams served not only as an introduction to the Berkeley Physics Department, but as an introduction to Dima Budker as well. Dima co-administered my oral exam on modern physics. By the end of my first year, I'd joined his research group and started working on the ytterbium experiment. Throughout my time in his group, Dima has been a great mentor, striking a good balance between skepticism, curiosity, and friendliness. He's also been supportive of my interest in physics education. I'm incredibly grateful to Dima for his guidance over the years.

The results in this dissertation are due to the hard work of a number of people over the course of about 17 years. During my relatively short time at Berkeley, I've only had the pleasure of meeting a small handful of them. I've been fortunate to work with a talented team of people, including: Kostya Tsigutkin, who led the ytterbium project when I first joined the group; Damon English, with whom I collaborated on several projects; Nathan Leefer, a good friend and colleague; Afrooz Family, Jim Tang, and Pasha Reshetikhin, all who worked on the ytterbium project as undergraduates; and many others. I thank them all for their mentorship, friendship, and contributions to this dissertation.

The Compass Project, a self-formed community of graduate and undergraduate students at Berkeley, has also had a huge impact on me. The people in that community are dedicated to, and passionate about, the worthy causes of improving education and increasing diversity in the sciences. It's been a pleasure learning from my friends and colleagues in Compass, including: Anna Zaniewski, Jacob Lynn, Nathan Roth, and Geoff Iwata, with whom I co-designed and co-taught inquiry-based physics courses; Ana Aceves, Yongchan Kim, Jaime Flores-Marquez, and Dominic Culver, my mentees; Joel Corbo, Badr Albanna, Angie Little, and Punit Gandhi, with whom I've co-authored publications for the physics education community; and about a hundred other people. Working with these creative, supportive students was an invaluable part of my experience at Berkeley.

There are several faculty at Berkeley whom I'd like to thank as well, including: Robert Harris and Hartmud Häffner, who served on my dissertation committee; Ori Ganor, who served on my qualifying exam committee; Bernard Sadoulet and Holger Müller, Compass's faculty sponsors; and Andrea diSessa, who has been instrumental in helping plan and implement research on the impacts of Compass.

I also acknowledge the love and support of my family and my partner, William Semel. William in particular has been patient, supportive, encouraging, and kind while I focus on physics and physics education. I truly appreciate their compassion and support.

Finally, I'd like to mention that the work in this dissertation appears in several articles published by the American Physical Society and in one article published by the Società Italiana di Fisica (Italian Physical Society).

Chapter 1

Introduction

Symmetry is a powerful tool for understanding the dynamics of physical systems. One particularly useful consequence of symmetric systems is that they are characterized by conservation laws [92]. For example, angular momentum is conserved in systems that have rotational symmetry. Parity, the subject of the present dissertation, is the conserved quantity associated with symmetry under spatial inversion. For many years the laws of physics were thought to be symmetric under a number of geometrical transformations, including spatial inversion. However, in the middle of the 20th Century, the physics community was confronted with irrefutable evidence that the electroweak interaction is *not* symmetric under spatial inversion and hence conservation of parity is violated by electroweak processes.

The mid-1950s saw a flurry of activity related to parity violation. In 1956, Tsung-Dao Lee and Chen Ning Yang pointed out that parity conservation in the electroweak interaction had not yet been tested, and they proposed several experiments for performing such a test [83]. Within a year, Chien-Shiung Wu, Leon Lederman, and their collaborators at Columbia University observed parity-violating effects in the beta decay of cobalt-60 [122] and in the decay of charged pions [61]. Soon after, Jerome Friedman and Valentine Telegdi reproduced the results of the pion decay experiments at the University of Chicago [60], further confirming that parity is not conserved and that our universe is indeed distinguishable from its mirror image. For their work, Lee and Yang were awarded the 1957 Nobel Prize in Physics.

Over the last 60 years, parity violation experiments have evolved from paradigm-shifting observations to tools for placing constraints on physics beyond the Standard Model (SM). This dissertation focuses on *atomic parity violation (APV)* experiments, a small subset of parity violation experiments that nevertheless has far reaching implications, *e.g.*, for high energy particle physics and nuclear physics. In this chapter, we take an historical approach to describing APV, give a rough sketch of the implications of APV experiments, and argue that ytterbium is an ideal candidate for the study of APV. Detailed reviews of APV can be found in Refs. [17, 27, 78, 91].

Figure 1.1: Feynman diagrams for two electron-nucleon radiative processes: (left) one governed solely by electromagnetic processes and (right) a second one involving exchange of the weak neutral gauge boson Z_0.

1.1 History and background

We begin our discussion with the background and history of APV. The theoretical origins of APV trace back to the late 1950s, when Yakov Zel'dovich addressed the question of how electroweak interactions manifest in atoms. His work lead to several predictions, key among them the rotation of the plane of polarization of visible light transmitted through a gas of optically inactive matter [124]. Such optical rotation arises in atomic vapors due to electroweak neutral current interactions between electrons and nucleons. Zel'dovich's initial estimates suggested that the effect was too small to be observed.

To understand the difficulty of detecting electroweak processes in atoms, we perform a naïve order of magnitude estimate, following a similar tack to that taken in Ref. [17]. Consider two different electron-nucleon radiative processes: an electromagnetic one of amplitude A_{em}, and an electroweak one of amplitude A_{w} which involves exchange of the neutral weak gauge boson Z_0 (Fig. 1.1). If we denote the four-momentum transfer between the electron and the nucleon by q, then $A_{\mathrm{em}} \propto e^2/q^2$ and $A_{\mathrm{w}} \propto g_{Z_0}^2/\left(q^2 + M_{Z_0}^2 c^2\right)$, where $g_{Z_0} \sim e$ and $M_{Z_0} = 91$ GeV$/c^2$ are the coupling constant and mass of the Z_0 boson, respectively. In atoms, the four-momentum is given by the inverse of the Bohr radius, *i.e.*, $q \sim \hbar/m_{\mathrm{e}}\alpha c$, where $m_{\mathrm{e}} = 0.51$ MeV$/c^2$ is the electron mass and $\alpha \approx 1/137$ is the fine structure constant. Therefore, our naïve estimate suggests that the electroweak amplitude is incredibly small compared to its electromagnetic counterpart:

$$A_{\mathrm{w}}/A_{\mathrm{em}} \sim \alpha^2 m_{\mathrm{e}}^2/M_{Z_0}^2 \approx 10^{-15}. \tag{1.1}$$

In practice, however, APV effects as large as 10^{-5} have been observed. The estimate (1.1) is too pessimistic because it neglects the impact of several enhancement mechanisms.

In the mid-1970s, Claude and Marie-Anne Bouchiat demonstrated that there exists a mechanism for enhancement of APV effects: the so-called Z^3 law [18]. According to the this law, electroweak effects in atoms grow roughly as the cube of the atomic number Z. The origins of the Z^3 scaling can be understood qualitatively by considering the the electron-nucleus potential due to APV interactions. This interaction is analogous to the Coulomb interaction, but with the Z_0 boson playing the role of the mediating photon. In the non-relativistic limit, an electron with position $\mathbf{r}_{\mathrm{e}}$, spin $\boldsymbol{\sigma}_{\mathrm{e}}$, and velocity $\mathbf{v}_{\mathrm{e}}$, will experience a

potential

$$H_w = \frac{Q_{\rm w} G_{\rm F}}{4\sqrt{2}} \left[\delta^{(3)}(\mathbf{r}_{\rm e})\boldsymbol{\sigma}_{\rm e} \cdot \mathbf{v}_{\rm e}/c + \text{h.c.}\right], \tag{1.2}$$

due to APV effects. Here $Q_{\rm w}$ is the *weak nuclear charge*, analogous to the electric nuclear charge Z, and $G_{\rm F}$ is the Fermi constant, which is proportional to $(g_{Z_0}/M_{Z_0})^2$. The electroweak charge accounts for one factor of Z in the Z^3 law since $Q_{\rm w} \approx -N$ and $N \geq Z$ for most heavy, stable nuclei. The second factor of Z is related to the the term $\delta^{(3)}(\mathbf{r}_{\rm e})$ in $H_{\rm w}$. Because the APV interaction is a contact interaction, its strength depends on the electron density near the nucleus. For orbitals that penetrate the nucleus, the electron density scales linearly with Z. Finally, the third factor of Z is due to the electron helicity $\boldsymbol{\sigma}_{\rm e} \cdot \mathbf{v}_{\rm e}$. Near the nucleus, the electron experiences a Coulombic electric potential and, consequently, the electron velocity is proportional to the nuclear charge Z.

The Z^3 enhancement of APV led researchers to search for parity-violating effects in heavy atoms. In the late 1970s, a few years after the Bouchiats' work and almost two decades after Zel'dovich first predicted APV effects, optical rotation was finally observed in bismuth by Lev Barkov and Max Zolotorev at the Nuclear Physics Institute in Novosibirsk [7]. Since then, optical rotation has been measured by several groups in bismuth [8, 10, 73, 85, 118], lead [87], and thallium [50, 116]. However, the most precise measurement of APV was achieved using a different method: the Stark interference technique.

Proposed by the Bouchiats in 1975 [19], the Stark interference technique measures APV using a difference in two transition rates: the rate $R_{A\to B}$ from initial state $|A\rangle$ to a final state $|B\rangle$ and the rate $R_{\tilde{A}\to\tilde{B}}$ between the "mirror states" $|\tilde{A}\rangle = P|A\rangle$ and $|\tilde{B}\rangle = P|B\rangle$, where P is the spatial inversion operator. The inequality of these two rates can be understood as follows. The Hamiltonian H governing these transitions has two contributions, one from electromagnetic processes and another from electroweak processes. The latter contribution makes H asymmetric under spatial inversion, that is, $[P, H] \neq 0$. It follows that non-commutation with P also applies to the time evolution operator $U(t) = \exp(-iHt/\hbar)$, that is, $[P, U(t)] \neq 0$.[1] Then

$$\begin{aligned} R_{\tilde{A}\to\tilde{B}} = |\langle\tilde{B}|U(t)|\tilde{A}\rangle|^2 &= |\langle B|P^{-1}U(t)P|A\rangle|^2 \\ &\neq |\langle B|U(t)|A\rangle|^2, \end{aligned} \tag{1.3}$$

and hence APV manifests in a difference between the rates of transition between two states and their mirror states,

$$R_{\tilde{A}\to\tilde{B}} \neq R_{A\to B}. \tag{1.4}$$

The Stark interference technique uses electric dipole ($E1$) transitions between atomic states of the same parity. Such transitions are strictly forbidden by QED because it is a spatially symmetric theory. Electroweak neutral currents break this symmetry, giving rise to a small but non-zero electric dipole amplitude $E1_{\rm pv} \sim i \times 10^{-11}\ ea_0$, where the factor of

[1] Non-commutation of P with H has many other consequences as well. For example, if $|A\rangle$ is an eigenstate of H, then its mirror state $|\tilde{A}\rangle$ is not.

i preserves time reversal invariance [78]. A second transition, of amplitude $E1_{\rm s}$, is induced by the Stark effect via application a static electric field $\mathbf{E}$. The Stark-induced amplitude is antisymmetric (odd) under spatial inversion. On the other hand, the weak-induced amplitude is asymmetric and therefore contains a symmetric (even) contribution that gives rise to a parity-violating asymmetry by interference with the much larger Stark-induced amplitude. The transition rate satisfies $R_\pm \propto |\pm E1_{\rm em} + E1_{\rm w}|^2$, where $R_+ \equiv R_{A\to B}$ and $R_- \equiv R_{\tilde{A}\to\tilde{B}}$ are the rates of the transition between the states and the mirror states, and the asymmetry is defined as

$$\mathcal{A} \equiv \frac{R_+ - R_-}{R_+ + R_-} = 2{\rm Im}(E1_{\rm w}/E1_{\rm em}). \tag{1.5}$$

In practice, experimental asymmetries are on the order of 10^{-5}. Because $E1_{\rm s} \propto E$, the strength of the parity-conserving transition is controlled by tuning the strength of the electric field. Nevertheless, the transition is sufficiently weak that it must be detected by fluorescence. We note that the transition rate scales like E^2 whereas the asymmetry scales like $1/E$. Therefore, the shot-noise limited signal-to-noise ratio is, in principle, independent of E.

The Stark-interference technique was successfully employed for the first time by M.-A. Bouchiat and her collaborators in Paris in 1982: they observed parity-violating Stark-weak interference in the 540 nm $6S_{1/2} \to 7S_{1/2}$ transition in cesium [20]. Shortly thereafter, at Berkeley, Persis Drell and Eugene Commins used the Stark interference technique to measure APV in the 293 nm $6P_{1/2} \to 7P_{1/2}$ transition in thallium [41]. Ultimately, the most precise measurement of APV was obtained by Carl Wieman's group in Boulder in 1997. As was the Paris group, the Boulder group was also investigating the 540 nm transition in cesium, achieving sub-1% experimental precision [120].

We conclude our historical outline of APV by noting that the Stark interference technique was also used to measure the most recent (and the largest) APV effect. In 2009, APV was measured in the 408 nm $6s^2\,{}^1S_0 \to 5d6s\,{}^3D_1$ transition in ytterbium [111, 112]. The description of the ytterbium APV experiment is the subject of this dissertation.

1.2 Implications

The three major goals of APV experiments are the determination of the nuclear weak charge $Q_{\rm w}$, verification of the scaling of $Q_{\rm w}$ with neutron number N, and measurement of a parity-violating nuclear moment called the *nuclear anapole moment*. These goals, which require significant theoretical and experimental effort, have significant implications for both nuclear physics and physics beyond the SM.

Testing the Standard Model

The electroweak parameter of utmost importance in APV experiments is the electroweak charge $Q_{\rm w}$ associated with the exchange of the Z_0 boson between an atomic electron and the

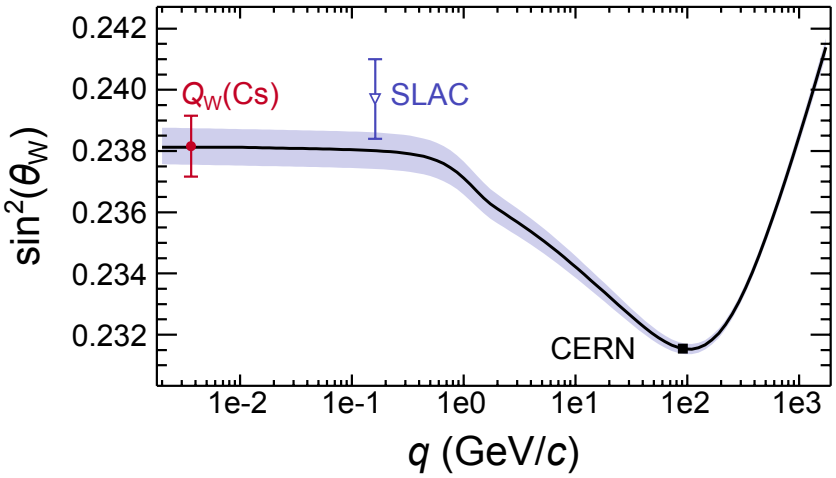

Figure 1.2: Running of the weak mixing angle. Predicted running of $\sin^2\theta_{\rm w}$ as a function of momentum transfer q (solid line) and its theoretical uncertainty (shaded area) is overlaid with results from cesium APV (circle) and high-energy experiments at SLAC (triangle) and CERN (square). See text for references.

nucleus. In the SM, $Q_{\rm w}$ is approximately equal to the neutron number N:

$$Q_{\rm w} = -N - Z(4\sin^2\theta_{\rm w} - 1) \approx -N, \tag{1.6}$$

where $\theta_{\rm w}$ is the weak mixing angle, given experimentally by $\sin^2\theta_{\rm w} = 0.23$. The weak mixing angle is a SM parameter that determines the relative strength of electromagnetic and electroweak couplings. Thus measurements of $Q_{\rm w}$ provide a stringent test of the SM at low momentum transfer ($q \sim$ MeV/c).

The cesium APV experiments yielded a value of $Q_{\rm w}$(Cs) having experimental and theoretical uncertainties of 0.35% [120] and 0.20% [94], respectively. In combination with high-energy experiments at SLAC [93] and CERN [25], the cesium APV results confirm the predicted running of $\sin^2\theta_{\rm w}$ over a momentum transfer spanning four orders of magnitude (Fig. 1.2). Moreover, the excellent agreement between the measured value of $Q_{\rm w}$(Cs) and that predicted by the SM constrains "new physics." For example, some grand unification and string theories hypothesize the existence of extra Z bosons which would contribute to the weak charge. The cesium result implies a stringent lower bound on the mass of such bosons: if they exist, they must be heavier than 1.3 TeV/c^2 [94]. Thus, despite the relatively low energies involved in atomic physics processes, APV experiments are powerful tools for exploring the limits of the SM.

Probing neutron distributions

However, it has not yet been possible to test an important prediction of the SM concerning the variation of Q_{w} along a chain of isotopes. It has been suggested [48] that rare earth atoms may be good candidates for APV experiments because they have chains of stable isotopes, and the APV effects may be enhanced due to the proximity of opposite-parity levels. While the accuracy of atomic calculations is unlikely to ever approach that achieved for atoms with a single valence electron, ratios of APV asymmetries between different isotopes should provide ratios of electroweak charges, without involving, to first approximation, any atomic structure calculations.

Measuring APV in isotopic chains has a second benefit: it can be used to probe neutron distributions. In particular, ratios of APV asymmetries are sensitive to the so-called *neutron skin*. The neutron skin is defined as the difference between the root-mean-square radii of neutron and proton distributions within the nucleus. Originally, sensitivity of APV ratios to the neutron skin was thought to limit their usefulness because uncertainties in neutron distributions would complicate interpretation of the ratios [58]. However, recent work shows that APV ratios can be used as tools to measure the neutron skin [23] and hence to shed light on the open question of neutron distributions [75].

Measuring the nuclear anapole moment

The neutron skin isn't the only nuclear property probed by APV experiments; they provide measurements of a parity-violating nuclear moment called the *anapole moment*. Anapole moments, whose existence was another of Zel'dovich's key predictions in the late 1950s [125], arise from electroweak interactions between nucleons and contribute to differences in APV amplitudes of two different hyperfine lines belonging to the same transition (see, for example, reviews [62, 71, 72]).

In general, the processes that contribute to APV are separated into two categories according to their dependence on nuclear spin [78]. The dominant contributions to APV usually come from nuclear spin-independent (NSI) processes, whereas nuclear spin-dependent (NSD) effects constitute small corrections [55]. Measurements of NSI APV in cesium [120], for example, led to the precise evaluation of $Q_{\mathrm{w}}(\mathrm{Cs})$, and those of NSD APV to the first observation of the cesium nuclear anapole moment [56]. The thallium nuclear anapole moment has likewise been extracted from NSD APV measurements [82].

The values of the cesium and thallium anapole moments result in constraints on electroweak coupling constants that are difficult to reconcile with those obtained from other nuclear-physics experiments and with each other [62, 71, 72]. Future anapole-moment measurements will provide additional insight to this open problem, and are a major goal of ongoing experiments in ytterbium [111], dysprosium [90], francium [64], radium ions [44, 63], and diatomic molecules [35].

Table 1.1: Stable isotopes of ytterbium ($Z = 70$) and corresponding neutron number N, nuclear spin I, and abundance.

Nuclide symbol	N	I	Abundance (%)
^{170}Yb	100	0	3
^{171}Yb	101	1/2	14
^{172}Yb	102	0	22
^{173}Yb	103	5/2	16
^{174}Yb	104	0	32
^{176}Yb	106	0	13

1.3 The case for ytterbium

The subject of the present dissertation is APV in the 408 nm $6s^2\,{}^1S_0 \rightarrow 5d6s\,{}^3D_1$ transition in ytterbium ($Z = 70$). This choice of atomic system was originally inspired by the prediction that the corresponding APV amplitude would be about two orders of magnitude times larger than that in cesium [33]. This prediction was supported by further theoretical work [30, 96] and was ultimately verified experimentally [111].

The 408 nm transition in ytterbium is a particularly attractive candidate for APV measurements because, in addition to exhibiting a large APV effect, ytterbium has several stable isotopes (Table 1.1). Therefore, this system can be used to probe low-energy nuclear physics in two ways: the neutron skin can be extracted from measurements of APV effects on a chain of naturally occurring isotopes, and the nuclear anapole moment can be determined from measurements in different hyperfine components for the same odd-neutron-number isotope. This combination of features makes the ytterbium system a truly versatile tool.

Chapter 2

Observation of APV in ytterbium

In this chapter, we report experimental verification of the predicted APV amplitude enhancement in ytterbium (Yb) using a measurement of the APV effect in the forbidden 408 nm $6s^2\,{}^1S_0 \rightarrow 5d6s\,{}^3D_1$ transition of ^{174}Yb. [111, 112]. We measured the APV induced transition matrix element to be $8.7(1.4) \times 10^{-10}\ ea_0$, which confirms the theoretically anticipated APV enhancement in Yb [33] and constitutes the largest APV effect observed so far. However, the measurement accuracy is not yet sufficient for the observation of the isotopic and hyperfine differences in the APV amplitude, the study of which is the main goal of the present experiments. Here we describe the impact of the apparatus imperfections and systematic effects on the accuracy of the measurements and discuss ways of improving it.

During the initial stage of the experiment, various spectroscopic properties of the $6s^2\,{}^1S_0 \rightarrow 5d6s\,{}^3D_1$ transition were measured, including: radiative lifetimes, Stark-induced amplitudes, hyperfine structure, isotope shifts, and dc-Stark shifts [21]. In addition, the 404 nm $6s^2\,{}^1S_0 \rightarrow 5d6s\,{}^3D_2$ transition has been observed, and the corresponding electric quadrupole transition amplitude and tensor transition polarizability have been measured [22]. The forbidden $M1$ amplitude of the 408 nm transition was measured to be $1.33 \times 10^{-4}\ \mu_0$ using the $M1$-$E1$ Stark interference technique [108]. The ytterbium atomic system, where transition amplitudes and interferences are well understood, has proven useful for gaining insight into the Jones-dichroism effects that had been studied in condensed-matter systems at extreme conditions and whose origin had been a matter of debate (see Ref. [24] and references therein).

An experimental and theoretical study of the dynamic (ac) Stark effect on the $6s^2\,{}^1S_0 \rightarrow 5d6s\,{}^3D_1$ forbidden transition was also undertaken [40, 107]. A model was developed to calculate spectral line shapes resulting from resonant excitation of atoms in an intense standing light wave in the presence of off-resonant ac-Stark shifts. A byproduct of this work was an independent determination of the Stark transition polarizability, which was found to be in agreement with the earlier measurement [22].

The present Yb APV experiment uses an atomic beam. An alternative approach would involve working with a heat-pipe-like vapor cell. Various aspects of such an experiment were investigated, including measurements of collisional perturbations of relevant Yb states [80],

nonlinear optical processes in a dense Yb vapor with pulsed UV-laser excitation [31]. Other proposed schemes for measuring APV in Yb include measurement of optical rotation on a transition between excited states [79] and measurement of parity-violating effects on the two-photon $6s^2\,{}^1S_0 \to 6s6p\,{}^1P_1 \to 6s6p\,{}^3P_0$ transition (Chapter 4).

In this chapter, we address the issues of sensitivity and systematics in the Yb APV experiment. In Sections 2.1 and 2.2, the experimental technique and its application in the present experiment are discussed. In Section 2.3, a method of analyzing the impact of various apparatus imperfections is described based on theoretical modeling of signals recorded by the detection system in the presence of imperfections. In Section 2.4, a detailed description of the experimental apparatus is given, along with a discussion of the origins of the imperfections, which is followed by an account of the measurements of the imperfections in Section 2.5. In Sections 2.6, we discuss measurements and analysis of the APV amplitude and systematic effects.

2.1 Experimental technique for the APV measurement

The idea of the experiment is to excite the forbidden 408 nm transition (Fig. 2.1) with resonant laser light in the presence of a quasi-static electric field. The APV amplitude of this transition arises due to APV mixing of the $5d6s\,{}^3D_1$ and $6s6p\,{}^1P_1$ states. This mixing arises because ${}^1P_1$ has a large admixture of the configuration $5d6p$ [33, 45]. The purpose of the electric field is to provide a reference transition amplitude, which is due to Stark mixing of the same states interfering with the APV amplitude. In such an interference method [19, 28], one is measuring the part of the transition probability that is linear in both the reference Stark-induced amplitude and the one induced by the electroweak interaction. In addition to enhancing the APV dependent signal, the Stark interference technique provides for all-important reversals that separate the APV effects from the systematics.

Even though the APV effect in Yb is relatively large, and the $M1$ transition is strongly suppressed, the $M1$ transition amplitude is still three orders of magnitude larger than the weak-interaction-induced amplitude. As a result, the geometry of the experiment was designed to suppress spurious $M1$-Stark interference. In addition, this effect is minimized by the use of a power-build-up cavity to generate a standing light wave. Since a standing wave has no net direction of propagation any transition rate which is linear in the $M1$ amplitude, will cancel out (see below).

The advantages of the present experimental configuration can be demonstrated by considering Yb atoms in the presence of static electric ($\mathbf{E}$) and magnetic ($\mathbf{B}$) fields interacting with a standing monochromatic wave produced by two counter-propagating coherent waves in an optical cavity. The electric field in the standing wave, $\boldsymbol{\mathcal{E}}$, is a sum of the fields of the two waves. In atomic units ($\hbar = m_{\rm e} = e = 1$), the rate of the resonant transition from the

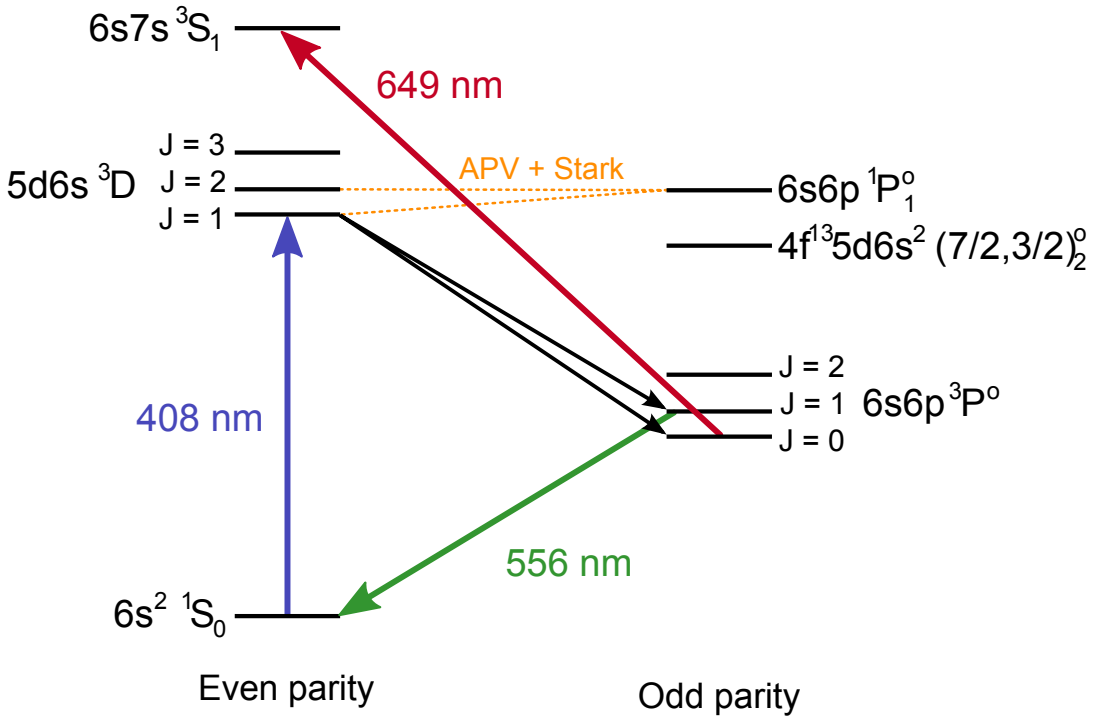

Figure 2.1: Energy eigenstates and transitions relevant to the Yb APV experiment.

ground state $^1S_0$ to the excited state $^3D_1$ is

$$R(M) = (2\pi)^2 \alpha \mathcal{I} |A(M)|^2 \frac{2}{\pi\Gamma}, \tag{2.1}$$

where α is the fine structure constant, $\mathcal{I}$ is the intensity of the 408 nm light, Γ is the natural linewidth of the transition, $A(M)$ is the transition amplitude, and $M \in \{0, \pm 1\}$ is the magnetic quantum number of the excited state. Here and in the rest of this section it is assumed that the individual magnetic sublevels of the $^3D_1$ state are resolved.

The transition amplitude $A(M)$ is the sum of $E1$ and $M1$ transition amplitudes:

$$A(M) = A_{E1}(M) + A_{M1}(M). \tag{2.2}$$

The $E1$ amplitude has two contributions corresponding to the Stark- and electroweak- mixing of the $^3D_1$ and $^1P_1$ states. That is,

$$A_{E1}(M) = A_{\rm s}(M) + A_{\rm w}(M) = i\beta(-1)^M \left(\mathbf{E} \times \boldsymbol{\epsilon}\right)_{-M} + i\zeta(-1)^M \epsilon_{-M}, \tag{2.3}$$

where β is the vector transition polarizability, ζ is related to the reduced matrix element of the Hamiltonian describing the weak interaction, $\boldsymbol{\epsilon}$ is the polarization of the optical field (given by $\boldsymbol{\mathcal{E}} = \mathcal{E}\boldsymbol{\epsilon}$), and $\epsilon_{0,\pm1}$ are the spherical components of the vector $\boldsymbol{\epsilon}$. Although Stark-induced

transitions are generally characterized by scalar, vector, and tensor polarizabilities [19, 22], only the vector polarizability contributes for the case of a $J = 0 \to 1$ transition. Equation (2.3) is derived in Appendix A.1.

Similarly, the $M1$ transition amplitude has two components: one for each of the two counter-propagating laser beams. Let $\boldsymbol{\mathcal{E}}_\pm = \mathcal{E}_\pm\,\boldsymbol{\epsilon}$ denote the electric fields of the beams traveling in the $\pm\mathbf{k}$ directions. Then $\boldsymbol{\mathcal{E}} = \boldsymbol{\mathcal{E}}_+ + \boldsymbol{\mathcal{E}}_-$ and the $M1$ amplitude is given by

$$\begin{aligned} A_{M1}(M) &= \mathcal{M}(-1)^M\,(\mathbf{k}\times\boldsymbol{\mathcal{E}}_+)_{-M} + \mathcal{M}(-1)^M\,(-\mathbf{k}\times\boldsymbol{\mathcal{E}}_-)_{-M} \\ &= \mathcal{M}(-1)^M\,(\delta\mathbf{k}\times\boldsymbol{\mathcal{E}})_{-M}\,, \end{aligned} \tag{2.4}$$

where $\mathcal{M}$ is the reduced matrix element of the $M1$ transition and $\mathbf{k}$ is a unit vector in the direction of the wavevector. Here we have introduced $\delta\mathbf{k} = \delta k\,\mathbf{k}$ with $\delta k = (\mathcal{E}_+ - \mathcal{E}_-)/\mathcal{E}$. For a perfect standing wave, $\mathcal{E}_+ = \mathcal{E}_-$ and hence $\delta k = 0$ and the $M1$ transition is completely suppressed. In practice, $\mathcal{E}_- = \mathcal{E}_+ - \delta\mathcal{E}$ due to the small but nonzero transmission of the back mirror in the cavity. Since $|\delta\mathcal{E}| \ll \mathcal{E}$, $|\delta k| \approx |\delta\mathcal{E}/\mathcal{E}| \ll 1$. Thus, although the $M1$ transition amplitude is not strictly zero, it is highly suppressed.

Without loss of generality, the quantities β, ζ, and $\mathcal{M}$ are assumed to be real. In general, the rate $R(M)$ given by Eq. (2.1) includes terms proportional to $\beta\mathcal{M}$ (Stark-$M1$ interference) and $\beta\zeta$ (Stark-weak interference). A careful choice of field geometry allows for suppression of undesirable Stark-$M1$ interference. From Eq. (2.3), it is evident that the Stark-PV interference is proportional to a pseudoscalar quantity called the *rotational invariant*:

$$(\boldsymbol{\mathcal{E}}\cdot\mathbf{B})[(\mathbf{E}\times\boldsymbol{\mathcal{E}})\cdot\mathbf{B}], \tag{2.5}$$

which is antisymmetric under spatial inversion (P-odd) and symmetric under time reversal (T-even).

In the present experimental apparatus, the electric field $\mathbf{E}$ is applied orthogonally to the magnetic field $\mathbf{B}$ and collinearly with the axis of the linearly-polarized standing light wave, as shown in Fig. 2.2. This geometry is such that the $M1$ and Stark-induced amplitudes are out of phase. Thus, they do not interfere and therefore do not produce spurious APV-mimicking effects (see Section 2.3).

2.2 PV signature: Ideal case

In the ideal case where we neglect the apparatus imperfections, the static magnetic and electric fields are $\mathbf{B} = B\,\hat{\mathbf{z}}$ and $\mathbf{E} = E\,\hat{\mathbf{x}}$, respectively, and the light polarization is

$$\boldsymbol{\epsilon} = \sin\theta\,\hat{\mathbf{y}} + \cos\theta\,\hat{\mathbf{z}}. \tag{2.6}$$

With this field orientation (see Fig. 2.2), Eqs. (2.2) through (2.4) yield

$$|A(0)|^2 = \beta^2E^2\sin^2\theta + 2\zeta\,\beta E\sin\theta\cos\theta, \tag{2.7}$$

$$|A(\pm1)|^2 = (1/2)\beta^2E^2\cos^2\theta - \zeta\,\beta E\sin\theta\cos\theta, \tag{2.8}$$

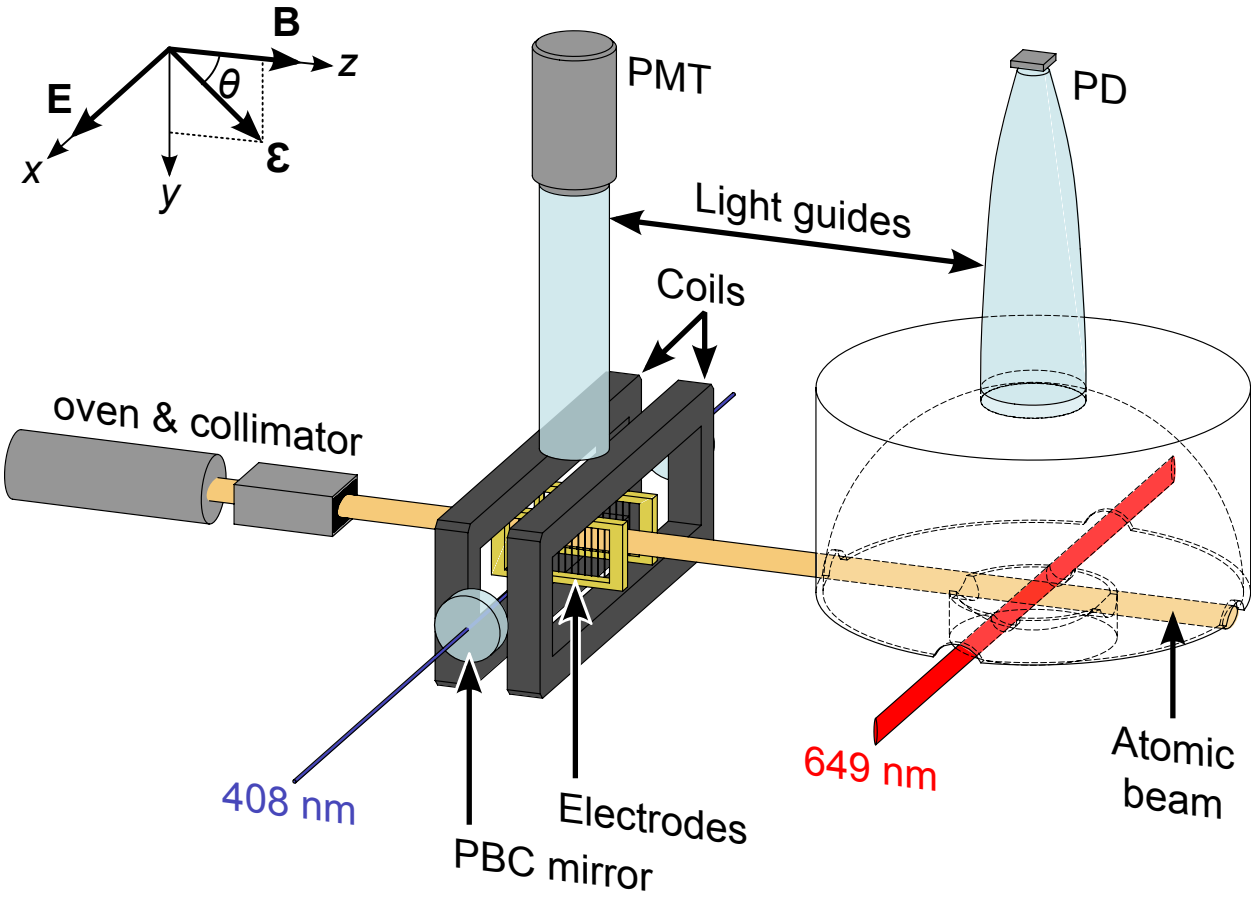

Figure 2.2: Experimental apparatus. An oven and collimator are used to generate a collimated beam of Yb atoms, travelling in the z-direction. Downstream, atoms are illuminated by 408 nm light in the presence of external electric (**E**) and magnetic (**B**) fields, where they undergo the parity-violating $6s^2\,{}^1S_0 \rightarrow 5d6s\,{}^3D_1$ transition. Large optical fields are achieved using a power build-up cavity (PBC). In this region, about a third of the excited atoms fluoresce at 556 nm and the rest decay to the metastable state ${}^3P_0$. Further downstream, the population of ${}^3P_0$ is probed by driving the 649 nm $6s6p\,{}^3P_0 \rightarrow 6s7s\,{}^3S_1$ transition. Parabolic and spherical mirrors ensure optimal collection efficiency of the ${}^3S_1$ fluorescence. Light guides transmit fluorescent light to a photomultiplier tube (PMT) and a photodiode (PD). Not shown is the vacuum chamber, which contains all depicted elements except the PMT and PD.

where terms of order ζ^2 and higher are neglected and $\delta k = 0$ is assumed.

In order to isolate the Stark-weak interference term from the dominant Stark-induced transition rate, we modulate the electric field: $E = E_{\rm dc} + E_{\rm ac}\cos(\omega t)$, where $E_{\rm ac}$ is the modulation amplitude, ω is the modulation frequency, and $E_{\rm dc}$ provides a DC bias. Then Eqs. (2.7) and (2.8) become

$$R(M) = R_0(M) + R_1(M)\cos(\omega t) + R_2(M)\cos(2\omega t), \tag{2.9}$$

where $R_n(M)$ is the amplitude of the nth harmonic of the transition rate $R(M)$. For convenience, we define the amplitudes $A_n(M)$ by

$$R_n(M) = (2\pi)^3 \alpha \mathcal{I} |A_n(M)|^2 \frac{2}{\pi\Gamma}. \tag{2.10}$$

Then $R_n(M) \propto |A_n(M)|^2$. The dominant Stark-induced contribution, which oscillates at twice the modulation frequency, is

$$|A_2(0)|^2 = (1/2)\beta^2 E_{\rm ac}^2 \sin^2\theta, \tag{2.11}$$

$$|A_2(\pm 1)|^2 = (1/4)\beta^2 E_{\rm ac}^2 \cos^2\theta. \tag{2.12}$$

On the other hand, the amplitude $R_1(M)$ contains the Stark-PV interference term:

$$|A_1(0)|^2 = 2\beta^2 E_{\rm ac} E_{\rm dc} \sin^2\theta + 2\zeta\beta E_{\rm ac}\sin\theta\cos\theta, \tag{2.13}$$

$$|A_1(\pm 1)|^2 = \beta^2 E_{\rm ac} E_{\rm dc}\cos^2\theta - \zeta\beta E_{\rm ac}\sin\theta\cos\theta. \tag{2.14}$$

The zeroth harmonic, $R_0(M)$, is a constant "background" to which our measurement technique is insensitive.

For a general polarization angle θ, all three Zeeman components of the transition are present while scanning over the spectral profile of the transition (Fig. 2.3). The first-harmonic signal due to Stark-PV interference has a characteristic signature: the sign of the oscillating terms for the two extreme components of the transition is opposite to that of the central component. The second-harmonic signal provides a reference for the lineshape since it is free from interference effects linear in $\mathbf{E}$. With a non-zero DC component present in the applied electric field, a signature identical to that in the second harmonic will also appear in the first harmonic. The latter can be used to increase the first-harmonic signal above the noise, which makes the profile analysis more reliable.

To obtain the APV asymmetry $\mathcal{A}_{\rm LR}$ from the measured first- and second-harmonic transition rates, we first normalize the first-harmonic signal $R_1(M)$ by its second-harmonic counterpart $R_2(M)$, generating a "partial" asymmetry:

$$\mathcal{A}(M) \equiv R_1(M)/R_2(M). \tag{2.15}$$

The asymmetry is obtained by combining the partial asymmetries in the following way:

$$\mathcal{A}_{\rm LR} \equiv \mathcal{A}(-1) + \mathcal{A}(+1) - 2\mathcal{A}(0) = -\frac{1}{\sin 2\theta}\frac{16\zeta}{\beta E_{\rm ac}}. \tag{2.16}$$

This method has the advantage that the asymmetry $\mathcal{A}_{\rm LR}$ is independent of $E_{\rm dc}$, so that the bias field may be chosen based on technical requirements of the experimental apparatus.

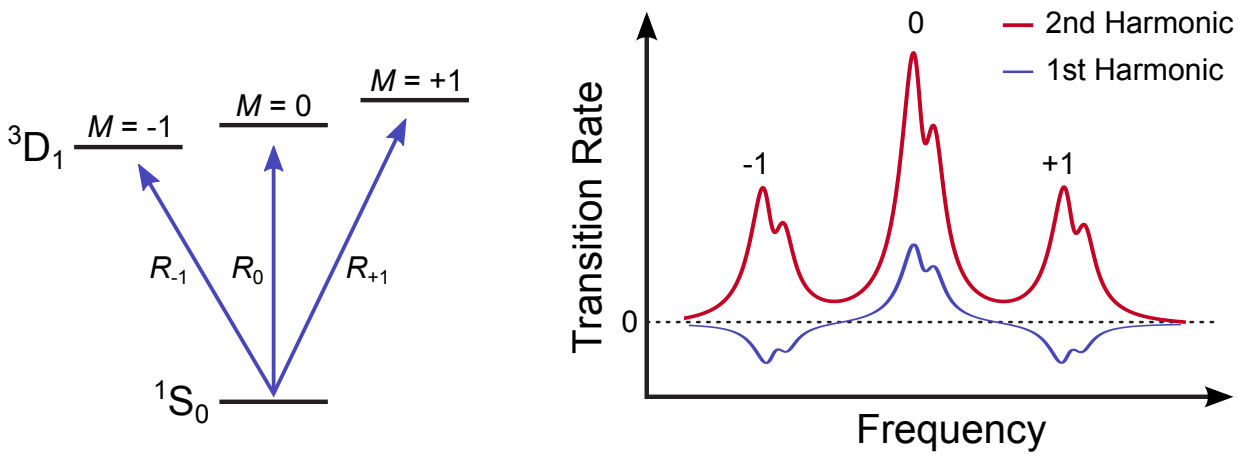

Figure 2.3: Discrimination of the APV-effect by E-field modulation under static magnetic field. Left: Schematic of transitions to different Zeeman sublevels of $^3D_1$. Right: The Zeeman pattern of the spectral profile is shown for the polarization angle $\theta = \pi/4$ for the first and second harmonic components of the transition rate. Effects of the DC bias are omitted.

2.3 PV signature: Impact of apparatus imperfections

While the current Yb-APV apparatus has been designed to minimize systematic effects, the APV mimicking systematics may be a result of a combination of multiple apparatus imperfections. In order to understand the importance of these effects, the electric and magnetic field misalignments and stray fields were included in a theoretical model of the transition rates as well as the excitation light's deviations from linear polarization. In addition, we relax the assumption that $\delta k = 0$ and include the effects of the residual $M1$ transition.

The quantization axis is defined along $\hat{\mathbf{z}}$ and, following the ideal case model, the axis of the standing light wave is collinear with $\hat{\mathbf{x}}$. We model an arbitrarily polarized light field as

$$\boldsymbol{\epsilon} = (\sin\theta\cos\phi + i\cos\theta\sin\phi)\hat{\mathbf{y}} + (\cos\theta\cos\phi - i\sin\theta\sin\phi)\hat{\mathbf{z}} \tag{2.17}$$

where θ is the polarization angle and ϕ is the ellipticity. Electric field imperfections are included by taking

$$\mathbf{E} \to \mathbf{E} = \tilde{\mathbf{E}} + \mathbf{E}',$$

where

$$\tilde{\mathbf{E}} = (E_{\mathrm{ac}}\hat{\mathbf{x}} + \tilde{e}_y\hat{\mathbf{y}} + \tilde{e}_z\hat{\mathbf{z}})\cos(\omega t) \quad \text{and} \quad \mathbf{E}' = E_{\mathrm{dc}}\hat{\mathbf{x}} + e_y\hat{\mathbf{y}} + e_z\hat{\mathbf{z}},$$

are the AC and DC components of the electric field. It is assumed that the y- and z-components of the AC field are in phase with the leading oscillating electric field. Out-of-phase AC reduce to sums of in-phase and DC components and are implicitly included in this model. The AC components are due to misalignments of the applied electric field with

Table 2.1: Lowest-order terms contributing to the partial asymmetry $\mathcal{A}(M)$.

	$\mathcal{A}_{\rm w}(M)$	$\mathcal{A}_{M1}(M)$	$\mathcal{A}_{\phi}(M)$
$M=0$	$+\dfrac{4\,\zeta\cot\theta}{\beta E_{\rm ac}}$	0	0
$M=-1$	$-\dfrac{4\,\zeta\tan\theta}{\beta E_{\rm ac}}$	$+\dfrac{4\,\delta k\,\mathcal{M}(\tilde{e}_y-\tilde{e}_z\tan\theta)}{\beta E_{\rm ac}^2}$	$+\dfrac{4\,e_z\phi\sec^2\theta}{E_{\rm ac}}$
$M=+1$	$-\dfrac{4\,\zeta\tan\theta}{\beta E_{\rm ac}}$	$-\dfrac{4\,\delta k\,\mathcal{M}(\tilde{e}_y-\tilde{e}_z\tan\theta)}{\beta E_{\rm ac}^2}$	$-\dfrac{4\,e_z\phi\sec^2\theta}{E_{\rm ac}}$

respect to the light wave axis as well as to the quantization axis $\hat{\mathbf{z}}$. The DC components arise due to a misalignment of the DC-bias field and also due to stray electric fields in the interaction region. The magnetic field imperfections are defined within the same frame of reference by taking analogously

$$\mathbf{B}\to\mathbf{B}=\tilde{\mathbf{B}}+\mathbf{B}',$$

where

$$\tilde{\mathbf{B}}=\tilde{b}_x\hat{\mathbf{x}}+\tilde{b}_y\hat{\mathbf{y}}+B\hat{\mathbf{z}}\quad\text{and}\quad\mathbf{B}'=b'_x\hat{\mathbf{x}}+b'_y\hat{\mathbf{y}}+b'_z\hat{\mathbf{z}},$$

where $\tilde{\mathbf{B}}$ and $\mathbf{B}'$ are reversing and stray non-reversing magnetic fields, respectively. The geometry of the ideal case is reproduced when $\phi=0$, $\tilde{e}_{y,z}=e_{y,z}=0$, and $\tilde{b}_{x,y}=b_{x,y,z}=0$.

Equations (2.1) through (2.4) apply when the quantization axis is along the magnetic field, thus a rotation $\mathbb{D}$ is applied to each of the vectors $\mathbf{E}$, $\mathbf{B}$, $\boldsymbol{\mathcal{E}}$, and $\mathbf{k}$ such that $\mathbb{D}\mathbf{B}\propto\hat{\mathbf{z}}$. That is, we take

$$\mathbf{B}\to\mathbb{D}\mathbf{B},\quad\mathbf{E}\to\mathbb{D}\mathbf{E},\quad\boldsymbol{\mathcal{E}}\to\mathbb{D}\boldsymbol{\mathcal{E}},\quad\text{and}\quad\mathbf{k}\to\mathbb{D}\mathbf{k},\tag{2.18}$$

where

$$\mathbb{D}=\mathcal{D}(-\alpha_y,\hat{\mathbf{y}})\mathcal{D}(\alpha_x,\hat{\mathbf{x}}).\tag{2.19}$$

Here the matrix $\mathcal{D}(\alpha,\hat{\mathbf{n}})$ represents a rotation about an axis $\hat{\mathbf{n}}$ through angle α. The angles α_x and α_y are given by

$$\alpha_{x,y}=(B-b'_z)(b'_{y,x}-\tilde{b}_{y,x})/B^2.\tag{2.20}$$

Thus, the electric field $\mathbf{E}$ and the polarization vector $\boldsymbol{\mathcal{E}}$ acquire additional components after the rotation (besides, for example, e_y and $\tilde{e}_y$).

Due to the imperfections, the partial asymmetries now include additional terms besides the Stark- and the PV effects:

$$\mathcal{A}(M)=\mathcal{A}_{\rm s}(M)+\mathcal{A}_{\rm w}(M)+\mathcal{A}_{M1}(M)+\mathcal{A}_{\phi}(M),\tag{2.21}$$

where $\mathcal{A}_{\rm s}(M)$, $\mathcal{A}_{\rm w}(M)$, $\mathcal{A}_{M1}(M)$, $\mathcal{A}_{\phi}(M)$ are contributions to the partial asymmetry due to $\mathbf{E}$ and $\mathbf{B}$ field imperfections and stray fields, the Stark-weak interference term, the Stark-$M1$ interference term, and the distorted linear polarization of the light. Expressions for the lowest-order terms are summarized in the Table 2.1.

Table 2.2: List of the lowest-order terms contributing to the asymmetry $\mathcal{A}_{\rm LR}$ for $|\theta| = \pi/4$ sorted with respect to their response to the reversals. $\mathcal{A}_{\rm LR,4}$ corresponding to a rather long list of terms that are invariant with respect to all reversals, is not shown in the table.

$\mathcal{A}_{\rm LR,1}$	$\mathcal{A}_{\rm LR,2}$	$\mathcal{A}_{\rm LR,3}$
$\frac{8(\tilde{e}_y e_z + \tilde{e}_z e_y)}{E_{\rm ac}^2} + \frac{16\tilde{b}_x e_y}{BE_{\rm ac}} + \frac{16\zeta}{\beta E_{\rm ac}}$	$\frac{16{b'}_x e_y}{BE_{\rm ac}}$	$\frac{16{b'}_x e_z}{BE_{\rm ac}}$

The asymmetry (2.16) has been chosen to determine the APV asymmetry. Since the $M1$ and ellipticity terms have opposite signs for $M = \pm 1$, their contributions to $\mathcal{A}_{\rm LR}$ cancel, while the contributions from $\mathcal{A}_{\rm w}(M)$ add.

The Stark contribution, $\mathcal{A}_{\rm s}(M)$, has several terms that are produced due to different imperfections and impacts all three Zeeman components, $M = 0, \pm 1$. In order to determine which terms could potentially mimic the APV asymmetry in $\mathcal{A}_{\rm LR}$, we discriminate the APV contribution to $\mathcal{A}_{\rm LR}$ with respect to the B-field reversal and flip of the polarization angle, θ. Switching to a different Zeeman component of the transition is also a reversal, which is incorporated in the expression for the asymmetry, $\mathcal{A}_{\rm LR}$. Analysis of the noise affecting the accuracy of APV-asymmetry measurements demonstrate that the highest signal-to-noise ratio is achieved when $\theta = \pm\pi/4$, and therefore, the polarization flip is a change of the polarization angle by $\pi/2$. Thus, the asymmetry (2.16) must be determined for four different combinations of the magnetic field directions and light-polarization angles: $\mathcal{A}_{\rm LR}(+B, +\pi/4)$, $\mathcal{A}_{\rm LR}(-B, +\pi/4)$, $\mathcal{A}_{\rm LR}(+B, -\pi/4)$, and $\mathcal{A}_{\rm LR}(-B, -\pi/4)$, so that terms having different symmetries with respect to the reversals can be isolated:

$$\begin{bmatrix} \mathcal{A}_{\rm LR,1} \\ \mathcal{A}_{\rm LR,2} \\ \mathcal{A}_{\rm LR,3} \\ \mathcal{A}_{\rm LR,4} \end{bmatrix} = \frac{1}{4} \begin{bmatrix} -1 & -1 & +1 & +1 \\ -1 & +1 & +1 & -1 \\ +1 & -1 & +1 & -1 \\ +1 & +1 & +1 & +1 \end{bmatrix} \cdot \begin{bmatrix} \mathcal{A}(+B, +\theta) \\ \mathcal{A}(-B, +\theta) \\ \mathcal{A}(+B, -\theta) \\ \mathcal{A}(-B, -\theta) \end{bmatrix}. \tag{2.22}$$

The result of this procedure is summarized in Table 2.2.

The APV asymmetry contributing to $\mathcal{A}_{\rm LR,1}$ is B-field even, θ-flip odd. It competes with the second-order terms that are a combination of the E-field and B-field alignment imperfections and stray fields. Using the theoretical value of $\zeta \simeq 10^{-9}\ ea_0$ [30, 96] combined with the measured $|\beta| = 2.24(0.12) \times 10^{-8}\ ea_0/(\text{V/cm})$ [22, 107], the expected APV asymmetry, $16\zeta/\beta\tilde{E}$, is about 10^{-4}, for $\theta = \pi/4$ and $E_{\rm ac} = 2$ kV/cm. For a typical value of misalignments and "parasitic" fields, $e_{y,z}/E_{\rm ac}$ and $\tilde{b}_x/B$ (on the order of 10^{-3} in the present apparatus), the contribution of the "parasitic" terms may be up to a few percent of the total value of $\mathcal{A}_{\rm LR,1}$. Ways of measuring the contribution of these imperfections are discussed in the following sections.

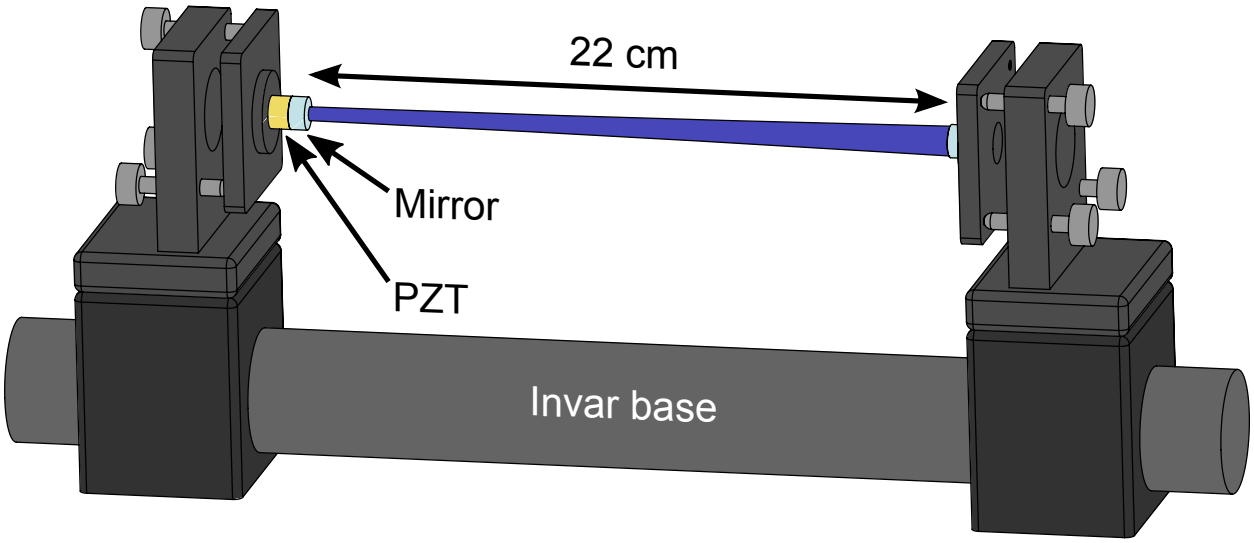

Figure 2.4: Schematic of the power buildup cavity.

2.4 Experimental apparatus

The forbidden 408 nm transition is excited by resonant laser light coupled into the power-buildup cavity in the presence of the magnetic and electric fields. The transition rates are detected by measuring the population of the $^3P_0$ state, where 65% of the atoms excited to the $^3D_1$ state decay spontaneously (Fig. 2.1). This is done by resonantly exciting the atoms with 649-nm light to the $6s7s\,^3S_1$ state downstream from the main interaction region, and by collecting the fluorescence resulting from the decay of this state to the $^3P_1$ and $^3P_2$ states and subsequently, from the decay of the $^3P_1$ state to the ground state $^1S_0$ (556 nm transition). As long as the 408 nm transition is not saturated, the fluorescence intensity measured in the probe region is proportional to the rate of that transition.

A schematic of the Yb-APV apparatus is shown in Fig. 2.2. A beam of Yb atoms is produced (inside of a vacuum chamber with a residual pressure of $\sim 3 \times 10^{-6}$ Torr) with an effusive source: a stainless-steel oven loaded with Yb metal, operating at $500 - 600$°C. The oven is outfitted with a multi-slit nozzle, and there is an external vane collimator reducing the spread of the atomic beam in the horizontal direction. The resulting Doppler width of the 408 nm transition is ~ 12 MHz [107].

Downstream from the collimator, the atoms enter the main interaction region where the Stark- and APV-induced transitions take place. Up to 80 mW of light at the transition wavelength of 408.345 nm in vacuum is produced by frequency doubling the output of a Ti:Sapphire laser (Coherent 899) using the Wavetrain^{cw} ring-resonator doubler. After shaping and linearly polarizing the laser beam, ~ 10 mW of the 408 nm radiation is coupled into a power buildup cavity (PBC) inside the vacuum chamber.

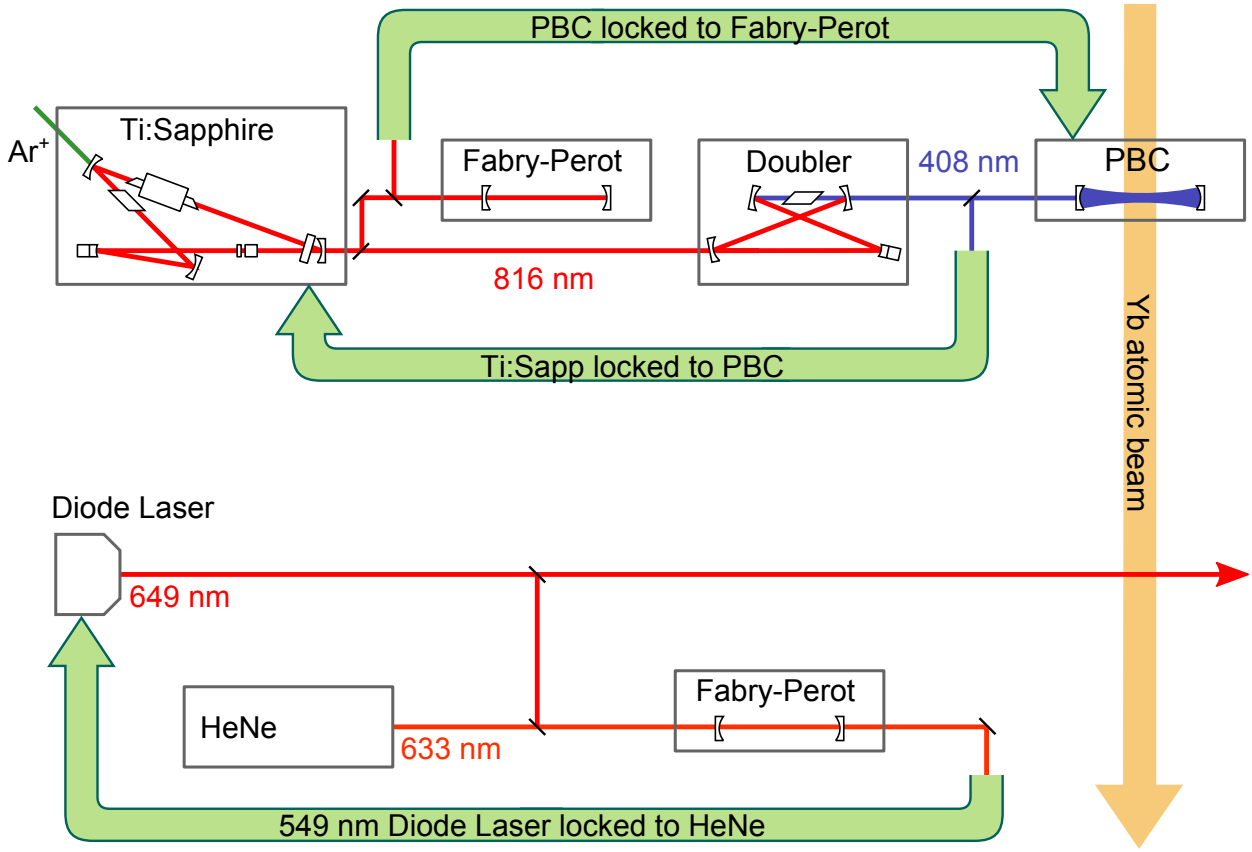

Figure 2.5: Schematic of the optical setup. Light at 408-nm is produced by frequency doubling the output of a Ti:Sapphire laser (Coherent 899) using the Wavetrain^{cw} ring resonator doubler. The laser is locked to the PBC using the FM-sideband technique. The PBC is locked to a confocal Fabry-Pérot étalon. This scannable étalon provides the master frequency. The 649-nm excitation light is derived from a single-frequency diode laser (New Focus Vortex). The diode laser is locked to a frequency-stabilized He-Ne laser using another scanning Fabry-Pérot étalon.

The cavity was designed to operate as an asymmetric cavity with flat input mirror and curved back mirror with a 25-cm radius of curvature and 22-cm separation between the mirrors. The atomic beam intersects the cavity mode in the middle of the cavity, where the $1/e^2$ radius of the mode in intensity is 172 μm. The asymmetric configuration has the advantage of larger mode radius at the interaction position compared to a symmetric cavity. A larger mode allows us to reduce the ac-Stark shifts, consequently reducing the width of the 408 nm transition. Alternatively, the cavity can be modified to operate in the symmetric confocal condition where multiple transverse modes can be excited, thereby increasing the effective "mode" size. However, we were unable to obtain high power and stable lock for the confocal configuration.

The cavity mirrors were purchased from Research Electro Optics, Inc. For the flat input mirror the transmission is 350 ppm with the absorption and scattering losses of 150 ppm total at 408 nm. The curved back mirror is designed to have a lower transmission of 50 ppm in order to additionally suppress the net light wave vector and, therefore, the $M1$ transition amplitude. The absorption and scattering losses in the curved mirror are 120 ppm. The finesse and the circulating power of the PBC are up to $\mathcal{F} = 9000$ and $P = 8$ W. These parameters were routinely monitored during the PV measurements. Details of the characterization of the PBC are addressed in Appendix A.2.

We found that the use of the 408 nm-PBC in vacuum is accompanied by substantial degradation of the mirrors. Typically after 6 hours of operation, the finesse drops by a factor of two. This is a limiting factor for the duration of the measurement run. The degradation of the finesse is due to the increased absorption and scattering losses. This effect is reversible: the mirror parameters can be restored by operating the PBC for several minutes in air, which makes performing a number of runs possible without replacing the mirrors. However, it takes several hours with the present apparatus to reach the desired vacuum after exposing the PBC to air. Presently, this effect is under investigation aiming for longer-duration experiments and shorter breaks in between.

A schematic of the PBC setup is presented in Fig. 2.4. The mirrors are mounted on precision optical mounts (Lees mounts) with micrometer adjustments for the horizontal and vertical angles and the pivot point of the mirror face. The mirror mounts are attached to an Invar rod supported by adjustable table resting on lead blocks. The input mirror is mounted on a piezo-ceramic transducer allowing cavity scanning.

The laser is locked to the PBC using the FM-sideband technique [42]. In order to remove frequency excursions of the PBC in the acoustic frequency range, the cavity is locked to a more stable confocal Fabry-Pérot étalon, once again using the FM-sideband technique. This stable scannable cavity provides the master frequency, with the power-build-up cavity serving as the secondary master for the laser. A schematic of the optical system is presented in Fig. 2.5.

The magnetic field is generated by a pair of rectangular coils designed to produce a magnetic field up to 100 G with a 1% non-uniformity over the volume with the dimensions of $1 \times 1 \times 1$ cm^3 in the interaction region. Additional coils placed outside of the vacuum chamber compensate for the external magnetic fields down to 10 mG at the interaction region.

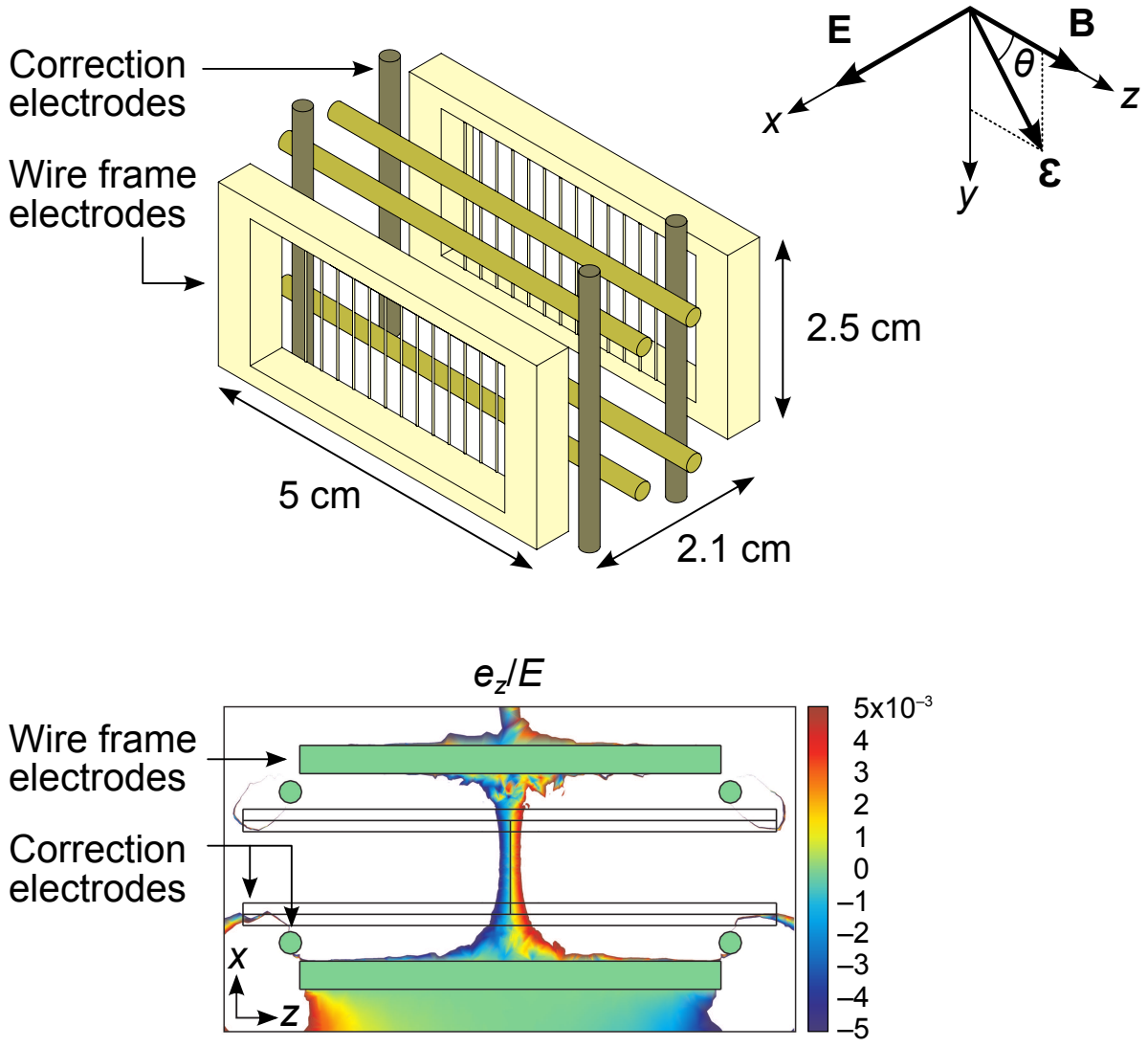

Figure 2.6: Schematic of the E-field electrodes assembly, and a result of the E-field modeling showing an X-Z slice of the amplitude of the E-field z-component, e_z, in a midplane (Y=0) of the assembly normalized by the total E-field amplitude, E. The voltage is applied to electrode 1, and electrode 2 and the correction electrodes are grounded.

The residual B-field of this magnitude does not have an impact on the APV measurements since its contribution is discriminated using the field reversals.

The electric field is generated with two wire-frame electrodes separated by 2.1 cm (see Fig. 2.6). The copper electrode frames support arrays of 0.2-mm diameter gold-plated wires. This design allows us to reduce the stray charges accumulated on the electrodes by minimizing the surface area facing the atomic beam, thereby minimizing stray electric fields. AC voltage of up to 10 kV at a frequency of 76.2 Hz is supplied to the electrodes via a high-voltage amplifier. An additional DC bias voltage of up to 100 V can be added.

The result of the electric field non-uniformity calculations is shown in Fig. 2.6. These calculations demonstrate that errors in the centering of the light beam with respect to the E-field plates may induce substantial parasitic components as large as, for example, $|e_z| \sim 5 \times 10^{-3} E_{\rm ac}$, producing parasitic effects comparable to the APV asymmetry. In order to measure and/or compensate the impact of the parasitic fields, additional electrodes designed to simulate stray E-field components were added to the interaction region. By applying high-voltage to these electrodes ("correction electrodes" in Fig. 2.6), the parasitic-field components may be exaggerated and accurately measured as described in the following sections.

Light at 556 nm emitted from the interaction region is collected with a light guide and detected with a photomultiplier tube. This signal is used for initial selection of the atomic resonance and for monitoring purposes. Fluorescent light from the probe region is collected onto a light guide using two optically polished curved aluminum reflectors and registered with a cooled photodetector (PD). The PD consists of a large-area (1×1 cm^2) Hamamatsu photodiode connected to a 1-GΩ transimpedance pre-amplifier, both contained in a cooled housing (temperatures down to -15°C). The pre-amp's bandwidth is 1 kHz and the output noise is ~ 1 mV (rms). The 649-nm excitation light is derived from a single-frequency diode laser (New Focus Vortex) producing ≈ 1.2 mW of cw output, high enough to saturate the $6s6p\,^3P_0 \rightarrow 6s7s\,^3S_1$ transition. Due to the saturation of this transition, $\sim$3 fluorescence photons per atom exited to the $^3P_0$ state are emitted at the probe region. The natural width of the 649-nm transition is 70 MHz, thus, its profile covers all transverse velocity groups (v_x) in the atomic beam ($\approx$ 8 MHz Doppler width at 649 nm). A drift of the laser frequency ($\sim$ 100 MHz per minute) is eliminated by locking the diode laser to a frequency-stabilized He-Ne laser using a scanning Fabry-Pérot étalon with the scanning rate of 25 Hz. The spectral distance between the étalon transmission peaks from the two lasers is measured during each scan and maintained constant within an accuracy of $\pm$3 MHz, good enough to eliminate any degradation of the probe-region signal.

The signals from the PMT and PD are fed into lock-in amplifiers for frequency discrimination and averaging. A typical time of a single spectral-profile acquisition is 20 s. The signals at the first and the second harmonic of the electric-field modulation frequency are registered simultaneously, which reduces the influence of slow drifts, such as instabilities of the atomic-beam flux. The modulation frequency is limited by several factors. Thermal distribution of atomic velocities in the beam causes a spread (of $\sim$ 2 ms) in the time of flight between the interaction region and the probe region. This, along with the finite bandwidth

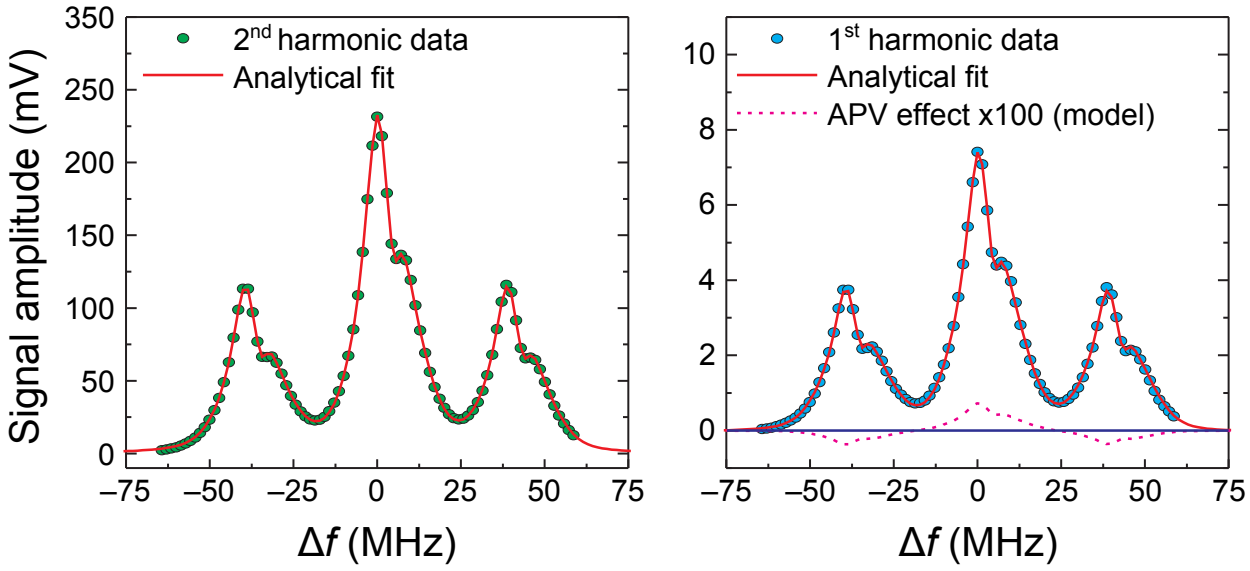

Figure 2.7: A profile of the B-field-split 408-nm spectral line of ^{174}Yb recorded at 1st- and 2nd-harmonic of the modulation. Also a simulated APV-contribution is shown for clarity. $\tilde{E}$=5 kV/cm; DC offset=40 V/cm; $\theta = \pi/4$; an effective integration time is 10 s per point.

of the PD, leads to a reduction of the signal-modulation contrast (see below). The choice of the modulation frequency of 76.2 Hz is a tradeoff between this contrast degradation and the frequent E-field reversal.

2.5 Results and analysis

In Fig. 2.7 a profile of the B-field-split 408 nm spectral line of the ^{174}Yb is shown. The 649-nm-light-induced fluorescence was recorded during a single profile scan. Statistical error bars determined directly from the spread of data are smaller than the points in the figure. The peculiar asymmetric line shape of the Zeeman components is a result of the dynamic Stark effect [107].

During a typical experimental run 100 profiles are recorded for each combination of the magnetic field and the polarization angle (400 profile scans in total). In order to compute the normalized amplitude, $\mathcal{A}(M)$, of a selected Zeeman component, the actual first-harmonic signal near the Zeeman peak is divided by the respective second-harmonic signal and then averaged over a number of the data points[1]. Then, the combination $\mathcal{A}_{\rm LR}$ of Eq. (2.16) is

[1]In the normalized rate calculations only data points having intensity higher that 1/3 of the respective Zeeman peak are used to avoid excessive noise from spectral regions with low signal intensity.

Table 2.3: Results of measurements of the electric field imperfections using artificially exaggerated AC- and DC-components, $\tilde{e}^{ex}_{y,z}$ and $e^{ex}_{y,z}$. These fields were generated by use of the correction electrodes, Fig. 2.6. $E_{\rm ac} = 2000(2)$ V/cm.

DC-Set	**AC-Set**
Exaggerated imperfections (V/cm)	
$e^{ex}_y = -140(2)$	$\tilde{e}^{ex}_y = -120(2)$
$e^{ex}_z = 20(2)$	$\tilde{e}^{ex}_z = 30(2)$
Measurements (mV/cm)	
$\tilde{e}_y e^{ex}_z/(2E_{\rm ac}) = 16(10)$	$e_y \tilde{e}^{ex}_z/(2E_{\rm ac}) = 4(5)$
$e^{ex}_y \tilde{b}_x/B + e^{ex}_y \tilde{e}_z/(2E_{\rm ac}) = 442(10)$	$e_z \tilde{e}^{ex}_y/(2E_{\rm ac}) = 40(5)$
Parasitic fields (V/cm)	
$\tilde{e}_y = 3.2(2)$	$e_y = 0.5(0.6)$
$2E_{\rm ac}\tilde{b}_x/B + \tilde{e}_z = -12.6(0.3)$	$e_z = -1.3(0.2)$

computed for each profile scan followed by averaging the result over all the scans at a given B-θ configuration. This procedure is repeated for all four reversals, and all B-θ symmetrical contributions, $\mathcal{A}_{\rm LR,1-4}$, are determined. In the present experiment, the values of $\mathcal{A}_{\rm LR,2,3,4}$-terms are found to be consistent with zero within the statistical uncertainty, which is the same as that of the APV-asymmetry (see below).

As can be seen from Table 2.2, terms in $\mathcal{A}_{\rm LR,1}$ associated with the fields imperfection are of crucial importance:

$$\frac{16}{E_{\rm ac}}\left[e_y\left(\frac{\tilde{e}_z}{2E_{\rm ac}} + \frac{\tilde{b}_x}{B}\right) + e_z\frac{\tilde{e}_y}{2E_{\rm ac}}\right].$$

In order to measure the contribution of these terms, artificially exaggerated E-field imperfections both static and oscillating, e^{ex}_z, e^{ex}_y, $\tilde{e}^{ex}_y$ and $\tilde{e}^{ex}_z$, are imposed by use of the "correction electrodes" (see Fig. 2.6), and two sets of the experiments were performed. In the first one, a DC-voltage was applied to the correction electrodes, and the measurements were done reversing e^{ex}_y and e^{ex}_z. These experiments yield values of $\tilde{e}_y$ and $\tilde{e}_z + 2E_{\rm ac}\tilde{b}_x/B$. In the second set, an AC-voltage modulated synchronously with the main E-field is applied to the correction electrodes. In order to reverse the sign of the parasitic terms a π-phase-shift of $\tilde{e}^{ex}_y$ and $\tilde{e}^{ex}_z$ with respect to the modulation signal is employed by switching the wiring of the correction electrodes. Thus, values of the DC-imperfections, e_y and e_z, are determined. The magnitudes of the applied electric fields and their distributions are calculated using a 3D-numerical-model of the interaction region. The results of the experiments are presented in Table 2.3.

The net contribution of these imperfections to $\mathcal{A}_{\rm LR,1}$ in the absence of the exaggerated

fields is found to be[2]:

$$e_y\left(\frac{\tilde{e}_z}{2E_{\rm ac}}+\frac{\tilde{b}_x}{B}\right)+e_z\frac{\tilde{e}_y}{2E_{\rm ac}}=-2.6(1.6)_{stat.}(1.5)_{syst.}\ mV/cm. \tag{2.23}$$

The systematic uncertainty comes from a sensitivity of the numerical model of the E-field, which is used for calculating the exaggerated fields in the interaction region, to an imperfect approximation of the electrode-system geometry. These experiments suggest that this field's imperfection cannot mimic the APV-effect entirely, nevertheless, it appears to be a major source of systematic uncertainty impacting the accuracy of the APV-asymmetry measurements. The most prominent contribution is given by a combined effect of the parasitic components of the electric field and the non-zero projection of the leading magnetic field on the direction of the electric field: $e_y(\tilde{e}_z/2E_{\rm ac}+\tilde{b}_x/B)$. The APV-asymmetry parameter, ζ/β is obtained from the measured value of $\mathcal{A}_{\rm LR,1}$ by compensating for the influence of these magnetic- and electric-field imperfections, Eq. (2.23).

There is another effect that cannot, by itself, mimic the PV-asymmetry, but needs to be taken into account for proper calibration. This effect is related to the E-field modulation implemented in the present experiment. The atoms are excited to the metastable state, $6s6p\,^3P_0$, by the light beam in the interaction region and then travel ∼20 cm until they are detected downstream in the probe region. Due to the spread in the time-of-flight between the interaction and probe regions, the phase mixing leads to a reduction of the signal modulation contrast at the probe region, and it depends on the signal-modulation frequency. Since the signal comprises two time-scales of interest, first- and second-harmonic of the E-field modulation, the contrast reduction is different for the two. Therefore, the ratio of the signal modulation amplitudes, $\mathcal{A}(M)$, on which we base the APV-asymmetry observation, appear altered in the probe region compared to what it would be at the interaction region. The amplitude combination, $\mathcal{A}_{\rm LR}$, and, therefore, the APV-parameter, ζ/β, are similarly affected. In our data analysis, a correction coefficient, C_0, is introduced, which has been calculated theoretically:

$$\left[\frac{\zeta}{\beta}\right]_{probe\ reg.} = C_0\left[\frac{\zeta}{\beta}\right]_{real}.$$

Under present experimental conditions, this coefficient, C_0, is found to be 1.028(3), and the measured APV parameter is corrected accordingly. Principles of its derivation are given in Appendix A.3.

In Fig. 2.8, the APV interference parameter ζ/β is shown as determined in 19 separate runs (∼60 hours of integration in total). Its mean value is

$$\zeta/\beta = 39(4)_{\rm stat.}(3)_{\rm syst.}\ {\rm mV/cm}, \tag{2.24}$$

which is in agreement with the theoretical predictions [30, 96]. The value of the APV parameter was extracted using the expression given in the first column of Table 2.2, taking

[2]Compare with the APV asymmetry parameter $\zeta/\beta \approx 40$ mV/cm.

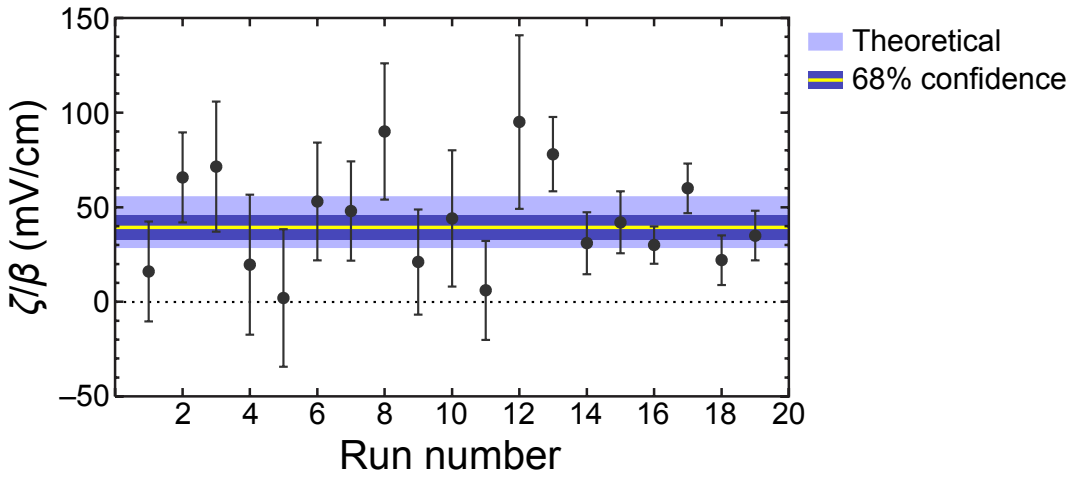

Figure 2.8: APV asymmetry in ytterbium. Shown are the measurements of the Stark-weak interference parameter ζ/β. The mean value is $39(4)_{\text{stat.}}(5)_{\text{syst.}}$ mV/cm, which corresponds to a weak-interaction-induced transition amplitude $|\zeta| = 8.7(1.4) \times 10^{-10}\ ea_0$.

into account the calibration correction C_0. Thus, $|\zeta| = 8.7(1.4) \times 10^{-10}\ ea_0$, which is the largest APV amplitude observed so far (here we used $|\beta| = 2.24(12) \times 10^{-8}\ ea_0/(\text{V/cm})$ [22, 107]).

The sign of the APV interference parameter ζ/β is found by comparing the measurements with the theoretical model of the transition rates employing the field geometry shown in Fig. 2.2. The direction and, thus, the signs of the electric and magnetic fields as well as the polarization angle θ were calibrated prior to the APV measurements. Special care was taken of detecting parasitic phase shifts in the lock-in amplifier. A signal from an arbitrary function direct digital synthesis (DDS) generator simulating the output of the probe region photodetector was fed into the amplifier. The signal is comprised of a sum of two sinusoidal waveforms, one frequency doubled, attenuated, and phase shifted with respect to the other. Results of the signal parameters measurement from the lock-in, such as the first-to-second harmonic amplitude ratio, relative phase shift and its sign, are compared to those used in the DDS generator to simulate the signal. The difference in the measured and generated amplitude ratio is found to be below 0.01%, and the relative phase shift is detected within $\pm 1.5°$. No relative sign flips between the first- and second-harmonic amplitudes were detected.

2.6 Error budget

The present measurement accuracy is not yet sufficient to observe the isotopic and hyperfine differences in the APV amplitude, which requires an accuracy better than $\sim 1\%$ for APV amplitude in a single transition [23, 97, 105].

In the present apparatus, the signal levels achieved values high enough to reach the signal-to-noise ratio (SNR) for the APV asymmetry if the noise were dominated by the fluorescence-photon shot-noise. The ideal shot-noise-limited SNR can be estimated as follows. Let $N_i \approx 10^6$ be the number of atoms illuminated by 408 nm light of intensity $\mathcal{I} \approx 80$ W/mm^2, which corresponds to about 10 W of power and a beam radius of about 200 μm (Sec 2.4). Then the number of excited atoms contributing to the first and second harmonics of the fluorescence signal are $N_{1,2} = N_i R_{1,2} t$, where t is the measurement time. Here N_2 and $N_1 \ll N_2$ are the number of excited atoms due to parity-conserving and parity-violating processes. The signal-to-noise ratio is SNR $= N_1/\sqrt{N_2}$, which reduces to

$$\mathrm{SNR} \approx \zeta\sqrt{8\pi\alpha\mathcal{I}t/\Gamma} \approx 3\sqrt{t(\mathrm{s})} \tag{2.25}$$

in the absence of a DC bias and systematic sources of noise. This is good enough to reach the sub-percent accuracy in a few hours of integration. However, a number of additional factors limit the accuracy.

One of the most important noise sources is the fluctuations of the modulating- and DC-field parameters during the experiment. The first- and the second-harmonic signals depend differently on the modulating electric field amplitude, E_{ac}, and the DC-bias, thus, a noise in the electronics controlling the fields contaminates the first-to-second harmonic ratio directly. A substantial effort was made to cope with this problem: a home-built high-voltage amplifier used in the first 13 runs was replaced by a commercial Trek 609B amplifier and a circuit controlling the DC-bias was upgraded. This allowed us to control the DC-bias and E_{ac} with mV-scale accuracy that would make the SNR to approach the shot-noise limit if this were the only source of the noise. As seen in Fig. 2.8, the last six measurements exhibit higher accuracy than the rest. These are the runs after the HV-system upgrade. However, the present SNR of $\approx 0.03/\sqrt{\tau(s)}$ is worse by almost two orders of magnitude than the shot-noise limit.

There are other fluctuations in the system parameters, such as light intensity fluctuations in the PBC, fluctuations of the spectral position of the PBC resonance with respect to the frequency reference, and noise in the detection system. All of them contribute to the noise in the first- and the second- harmonic signals but we found that such noise largely canceled in the ratio $\mathcal{A}(M)$.

However, there is a noise source, which is not canceled in the ratio. The following experiments demonstrated that this noise source is related to frequency excursions of the Fabry-Pérot étalon serving as the frequency reference for the optical system. In these experiments the excitation light was frequency tuned to a wing of the atomic resonance, and the first- and second-harmonic signals were recorded without scanning over the resonance. Then, the same was done when the spectral position was set at the peak of the resonance, and a change of the SNR for the harmonics ratio was determined. These experiments were performed using the upgraded HV-system. Results of the measurements are presented in Fig. 2.9.

For a shot-noise-limied signal, the SNR at the peak of the resonance is expected to be a factor of about $\sqrt{2}$ higher than at the wing due to larger signal. It was found, however, that

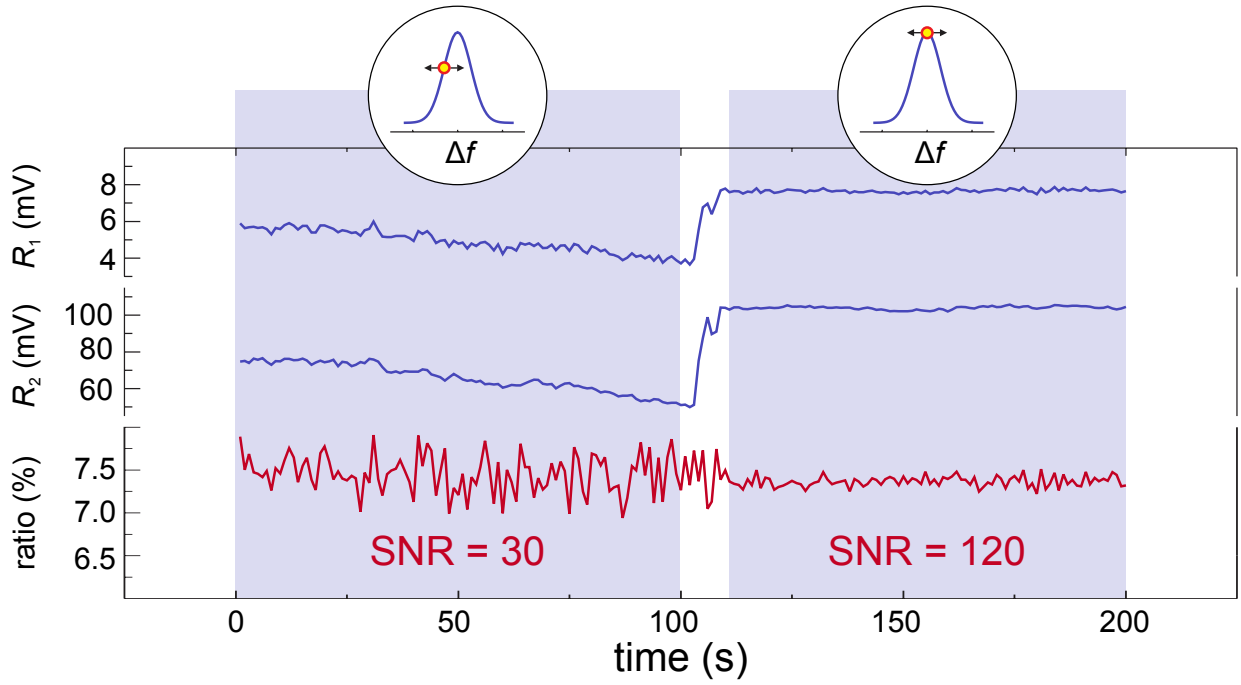

Figure 2.9: Impact of the frequency excursions of the Fabry-Pérot étalon on the noise level in the harmonics ratio. A change in the noise level when the optical system was tuned from the wing of the atomic resonance to its peak is shown. In the inserts above the excitation light spectral position is shown schematically with respect to the atomic resonance. Arrows denote the fluctuations.

the SNR went up by a factor of 4 by tuning from the wing to the peak of the resonance. This demonstrates that the main source of noise is not photon statistics but fluctuations in the spectral reference. Indeed, the frequency excursions at the wing of the spectral line produces substantially more intensity noise due to a steeper spectral slope than that at the peak, where the slope is nominally zero. It must be emphasized, that in the case of slow frequency excursions (compared to the E-field modulation period), the noise in the first- and the second-harmonic channels would be canceled in the ratio. However, fast excursions can generate noise in the signal ratio.

The factors affecting the measurement accuracy mentioned above have an impact on the statistical error of the result. The present systematic errors (summarized in Table 2.4) has nearly the same significance as the statistical one and also comprises a number of factors.

One of the most significant factors is the uncertainty in the field-imperfection contributions, Eq. (2.23). This uncertainty is mostly due to statistical factors such as laser drifts, nevertheless, it provides an offset to the PV-parameter. Since the measurement of this contribution is actually the same measurement as the APV-effect, any improvements of the stability reduces the overall systematic uncertainty. We would like to emphasize also that

Table 2.4: List of factors contributing to the systematic uncertainty of the parameter ζ/β.

Factor	**Uncertainty (%)**
$\tilde{E}$ value:	
geometry	5
numerical modeling	3
Applied field imperfections	5
Phase mixing	0.5
Other	1
Total (in quadrature)	**8**

Eq. (2.23) represents a mean value of the imperfection contribution over numerous experiments averaging over possible fluctuations of the field-imperfection contribution. These fluctuations may be partially responsible for the variance in the APV-parameter, and, thus, the statistical uncertainty of its value. This fact demonstrates that the elimination of the field-imperfections is an essential requirement for improving the overall accuracy of the experiments.

Another significant source of the systematic uncertainty is the uncertainty in the value of the electric field in the interaction region. While the voltage applied to the E-field plates and the correction electrodes is controlled precisely, the actual E-field value used in the APV parameter determination depends on the accuracy of the numerical modeling of the electric-field distribution in the particular geometry. There are two factors in the model contributing to the uncertainty: finite accuracy of measurements of the interaction region geometrical parameters, and the imperfect approximation of the geometry in the numerical simulation.

However, while this systematic uncertainty plays a significant role for measurements of the APV parameter of a single isotope, for the isotope ratios this uncertainty will cancel (or will be substantially reduced), if the measurements observing different isotopes are performed without changing the E-field geometry. The same is true for the calibration parameter, C_0, which also cancels in the isotope ratios.

There are other, rather minor, factors contributing to the systematic uncertainty, for example, a finite accuracy of the polarization angle flip, errors in the lock-in amplifiers, a finite dynamic range of the lock-ins etc. The net contribution of these factors is found to be $\lesssim 1\%$. A summary of the systematic error budget is presented in Table 2.4.

One goal of the future measurements of the parity-violation effects in ytterbium is observing a difference in the APV effect between different isotopes. The net uncertainty of the APV parameter of a single isotope must be better than 1% based on the theoretical predictions. Methods for improvement are discussed in Chapter 5.

Chapter 3

Measurement of ac polarizabilities in ytterbium

Static (dc) and dynamic (ac) electric dipole polarizabilities determine the response of neutral particles to applied electric fields. They are related to a host of atomic and molecular quantities, including the dielectric constant, refractive index, and Stark shift [2, 3, 12, 13], and are an important consideration for many current atomic, molecular, and optical physics experiments [88]. For example, polarizabilities play a vital role in the production of light traps for quantum information processing applications [123]. In the context of optical atomic clocks, Stark shifts constitute an important systematic effect that must be controlled [5, 26, 109, 114]. Similarly, Stark shifts also contribute to systematic effects in atomic parity violation (APV) measurements [111, 112, 119, 121]. Hence the determination of polarizabilities is a priority for high-precision atomic physics.

Present experiments typically rely on theoretical calculations of electric dipole polarizabilities [9, 43, 100]. Several methods for measuring polarizabilities also exist. Early schemes involved the deflection of atoms in an inhomogeneous electric field [12]. More recent techniques include absolute frequency measurements [5], atom interferometry [32, 51, 89], and a technique that uses light force [76, 77]. However, these methods typically provide information about the polarizability of an atom in its *ground* state [88]. Therefore, they are inappropriate for high-precision experiments where the polarizabilities of *excited* states are relevant.

As part of an ongoing investigation of parity violation in atomic ytterbium (Yb) [111, 112], a scheme for measuring a combination of polarizabilities of the ground and an excited state of Yb was developed [40, 107]. The scheme involves the simulation and measurement of the spectral lineshape of a forbidden electric dipole transition driven by a standing wave of light in the presence of a dc electric field. Due to the standing wave, the ac Stark shifts of the upper and lower states introduce a polarizability-dependent distortion in the lineshape, a phenomenon which was first observed and characterized during a search for APV in cesium [119]. The difference of polarizabilities of the two states is treated as a variable parameter in the simulation and is measured by fitting the simulated lineshape to

experimental data. We call this scheme the Lineshape Simulation Method (LSM). The LSM can be generalized to an arbitrary atomic species.

In this chapter, we present the next generation of the LSM, which was described in Ref. [40]. The numerical procedures accommodate for a broad domain of values of input parameters, *e.g.*, the intensity of the standing wave. In addition, the independent dimensionless parameters that determine the lineshape have been explicitly identified, thus facilitating error analysis. In general, the LSM is compatible with a variety of atomic species and field geometries. The LSM is sensitive to the *difference* of polarizabilities of the atom in its ground and excited states. Nevertheless, this method may yield unambiguous measurements of the vector and tensor components of the excited state polarizability, as we will show. In this sense, we present a versatile method for measuring the excited-state polarizabilities of atoms.

We demonstrate the LSM using the 408-nm $6s^2\,{}^1S_0 \rightarrow 5d6s\,{}^3D_1$ transition in atomic Yb. Whereas the previous results [107] were obtained in the absence of a magnetic field, the present work uses a magnetic field to isolate Zeeman sublevels of the excited state. The ac Stark shifts of the sublevels are characterized by different combinations of scalar, vector, and tensor polarizabilities. This approach allows for the unambiguous determination of these polarizabilities. The ac scalar and tensor polarizabilities of the excited state $5d6s\,{}^3D_1$ in Yb are measured for the first time. Due to improvements in the experimental apparatus, the signal-to-noise ratio of the observed lineshape is an order of magnitude larger than for the previous implementation. In the present work, the statistical error introduced by the LSM is negligible compared to the systematic uncertainty of the experiment.

This chapter is organized as follows. In Section 3.1, we introduce our conventions for the polarizabilities and the Stark shift. The theoretical model, numerical procedure, and results of the simulation are discussed in Section 3.2. In Section 3.3 we apply the LSM to the Yb system and present the results. Finally, a summary of the results and an outlook for future experiments are given in Section 3.4.

3.1 Atomic system

Throughout this work, we consider a Stark-induced transition between two atomic states of the same parity. The transition is induced by applying a uniform dc electric field $\mathbf{E}$. We assume that the transition is driven by a standing wave of light formed by two counter-propagating waves with the same polarization traveling in the $\pm\mathbf{k}$ directions. In this case, the electric field of the light is given by

$$\boldsymbol{\mathcal{E}}(\mathbf{r},t) = \mathcal{E}(\mathbf{r})\cos(\omega t)\,\boldsymbol{\epsilon}, \tag{3.1}$$

where

$$\mathcal{E}(\mathbf{r}) = \mathcal{E}_0\cos(\mathbf{k}\cdot\mathbf{r})e^{-r_\perp^2/r_\mathrm{b}^2}. \tag{3.2}$$

Here $\mathcal{E}_0$, $\mathbf{k}$, ω, and $\boldsymbol{\epsilon}$ are the amplitude, wave-vector, angular frequency, and polarization of the electric field, respectively, r_b is the radius of the standing wave, and $r_\perp = |\mathbf{r} - \hat{\mathbf{k}}(\hat{\mathbf{k}}\cdot\mathbf{r})|$

is the perpendicular distance from the center of the standing wave. In addition to these parameters, we define the wave-number $k \equiv |\mathbf{k}| = \omega/c$ and the wavelength $\lambda \equiv 2\pi/k$, where c is the speed of light. We assume that $\mathcal{E}_0 > 0$ since the overall sign of the field can be incorporated into the polarization $\boldsymbol{\epsilon}$. Equation (3.2) is appropriate for the case of a light field with a Gaussian profile. The discussion is limited to optical frequencies. In this regime, $\boldsymbol{\mathcal{E}}(\mathbf{r}, t)$ is uniform over atomic length scales. In order to study the influence of the magnetic structure of the transition, we also assume the presence of a uniform dc magnetic field $\mathbf{B}$. The quantization axis (z-axis) is chosen so that $\mathbf{B} = B\,\hat{\mathbf{z}}$ for $B > 0$.

The dynamics of an atom in the presence of the external magnetic and electric fields described above is governed by the total Hamiltonian

$$H = H_0 + H_1(t), \tag{3.3}$$

where $H_0 \equiv H_{\mathrm{A}} + H_{\mathrm{Z}} + H_{\mathrm{dc}}$ and $H_1(t) \equiv H_{\mathrm{ac}}(t)$ are the time-independent and time-dependent parts of H. Here H_{A} is the atomic Hamiltonian, $H_{\mathrm{Z}} = -\boldsymbol{\mu} \cdot \mathbf{B}$ is the Zeeman Hamiltonian, $H_{\mathrm{dc}} = -\mathbf{d} \cdot \mathbf{E}$ and $H_{\mathrm{ac}}(t) = -\mathbf{d} \cdot \boldsymbol{\mathcal{E}}(\mathbf{r}, t)$ are the dc and ac Stark Hamiltonians, and $\boldsymbol{\mu}$ and $\mathbf{d}$ are the magnetic and electric dipole moments of the atom, respectively. We assume that $\mathbf{B}$, $\mathbf{E}$, and $\boldsymbol{\mathcal{E}}(\mathbf{r}, t)$ are sufficiently electroweak that H_{Z}, H_{dc}, and H_{ac} can be treated as successive perturbations to H_{A}.

Let $|\ell\rangle = |\gamma J M\rangle$ and $\omega_{\mathrm{A}}(\ell) = \omega_{\mathrm{A}}(\gamma J)$ represent the degenerate eigenstates of the atomic Hamiltonian H_{A} and their corresponding energies, respectively. Here J is the total angular momentum quantum number, $M \in \{J, J-1, \ldots, -J\}$ is the magnetic quantum number corresponding to the projection of the total angular momentum along the z-axis, and γ is a set of other quantum numbers. Then, to lowest order in the perturbing fields B and E, the eigenstates of H_0 are

$$|\bar{\ell}\rangle = |\ell\rangle + \sum_{\ell' \neq \ell} |\ell'\rangle \frac{\langle \ell' | H_{\mathrm{dc}} | \ell \rangle}{\omega_{\mathrm{A}}(\ell) - \omega_{\mathrm{A}}(\ell')}, \tag{3.4}$$

with corresponding energies

$$\omega(\bar{\ell}) = \omega_{\mathrm{A}}(\ell) + \omega_{\mathrm{Z}}(\ell) + \omega_{\mathrm{dc}}(\ell). \tag{3.5}$$

Here $\omega_{\mathrm{Z}}(\ell)$ and $\omega_{\mathrm{dc}}(\ell)$ represent the Zeeman and dc Stark shifts, respectively. The Zeeman shift is given by $\omega_{\mathrm{Z}}(\ell) = g_\ell \mu_0 B M$, where g_ℓ is the Landé factor of the state $|\ell\rangle$ and μ_0 is the Bohr magneton. Throughout this work, we assume that B is sufficiently strong to completely isolate the Zeeman sublevels of $|\ell\rangle$. The dc Stark shift is given by $\omega_{\mathrm{dc}}(\ell) = -(1/2)\alpha_\ell^{\mathrm{dc}} E^2$, where $E = |\mathbf{E}|$ is the magnitude of the dc electric field, and $\alpha_\ell^{\mathrm{dc}}$ is the dc polarizability of the atom in state $|\ell\rangle$. To derive Eq. (3.4), we neglected mixing of atomic eigenstates due to the magnetic field.

The atomic energy levels are also shifted by the ac Stark shift [2, 3, 12, 13], which is induced by the dynamic field $\boldsymbol{\mathcal{E}}(\mathbf{r}, t)$. We assume that the frequency of the standing wave satisfies $\omega \approx \omega_{ag}$, where ω_{ag} is the resonant frequency of the electric-dipole (E1) transition from the perturbed electronic ground state $|\bar{g}\rangle$ to a perturbed excited state $|\bar{a}\rangle$. Thus it is

appropriate to make a two-level approximation that involves neglecting dynamic interactions between states other than $|\overline{g}\rangle$ and $|\overline{a}\rangle$. However, such an approximation can only account for ac Stark shifts that arise due to mixing of the states $|\overline{g}\rangle$ and $|\overline{a}\rangle$ with each other. To address this situation, we modify the energy of the perturbed ground state as follows:

$$\omega(\overline{g}) \to \omega(\overline{g}) + \omega_{\rm ac}(\overline{g}), \tag{3.6}$$

where

$$\omega_{\rm ac}(\overline{g}) = -\alpha_{\overline{g}} \left[\mathcal{E}(\mathbf{r})/2\right]^2, \tag{3.7}$$

is the ac Stark shift[1] of $|\overline{g}\rangle$ due to mixing of $|\overline{g}\rangle$ with states other than $|\overline{a}\rangle$, and $\alpha_{\overline{g}}$ is the corresponding ac polarizability of the state $|\overline{g}\rangle$. An analogous modification is made to the energy of the perturbed state $|\overline{a}\rangle$.

We further assume that the unperturbed ground and excited states $|g\rangle = |\gamma_g J_g M_g\rangle$ and $|a\rangle = |\gamma_a J_a M_a\rangle$ have the same parity. In this case, the $\overline{g} \to \overline{a}$ transition is induced by the dc electric field [19] and the mixing of the states $|\overline{g}\rangle$ and $|\overline{a}\rangle$ with each other is characterized by the induced dipole matrix element

$$\langle \overline{a}|\mathbf{d}\cdot\boldsymbol{\epsilon}|\overline{g}\rangle \equiv d_{\rm in}. \tag{3.8}$$

We assume $d_{\rm in} \geq 0$ since any complex phase can be incorporated into the states $|\overline{a}\rangle$ and $|\overline{g}\rangle$. Note that the value of $d_{\rm in}$ depends on the dc field $\mathbf{E}$ and the light polarization $\boldsymbol{\epsilon}$. In particular, $d_{\rm in} \to 0$ as $\mathbf{E} \to \mathbf{0}$. Therefore, the dynamic field does not cause mixing of the states $|\overline{g}\rangle$ and $|\overline{a}\rangle$ in the absence of the electric field. The polarizability $\alpha_{\overline{g}}$ in Eq. (3.7) represents the ac polarizability of the unperturbed ground state $|g\rangle$, provided the effects of the dc field on the ac polarizability can be neglected. In this case, $\alpha_{\overline{g}} = \alpha_g$.

In general, ac polarizabilities depend on the polarization $\boldsymbol{\epsilon}$ and frequency ω of the external light field. The polarizability of an arbitrary atomic state $|\ell\rangle$ can be decomposed into three terms:

$$\alpha_\ell = \alpha_0(\gamma J) + i\,\alpha_1(\gamma J)\,\frac{M}{J}\,(\boldsymbol{\epsilon}\times\boldsymbol{\epsilon}^*)\cdot\hat{\mathbf{z}} + \alpha_2(\gamma J)\,\frac{3M^2 - J(J+1)}{J(2J-1)}\,\frac{3|\boldsymbol{\epsilon}\cdot\hat{\mathbf{z}}|^2 - 1}{2}. \tag{3.9}$$

The quantities $\alpha_0(\gamma J)$, $\alpha_1(\gamma J)$, and $\alpha_2(\gamma J)$ are referred to as the *scalar*, *vector*, and *tensor* polarizabilities, respectively [12]. The scalar, vector, and tensor polarizabilities are independent of the magnetic quantum number M and the polarization $\boldsymbol{\epsilon}$, and hence are independent of the choice of quantization axis and field geometry. However, they depend on the light frequency ω, as described in Appendix D.

Hereafter, we abandon the use of the overline to distinguish between perturbed and unperturbed atomic states. Despite the lack of an overline, quantum states should be interpreted as atomic states that have been perturbed by the static electric and magnetic fields $\mathbf{E}$ and $\mathbf{B}$, unless otherwise noted.

[1] In Refs. [107] and [40], a different convention for the ac Stark shift is used.

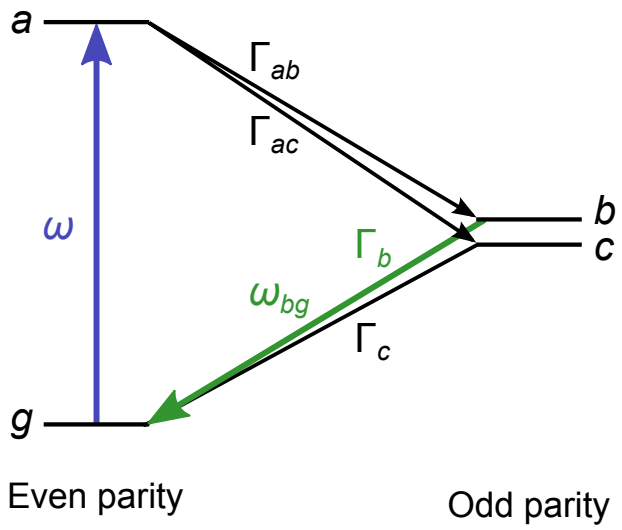

Figure 3.1: Energy-level diagram. Shown are the energy eigenstates of an atom and the electronic transitions relevant to the LSM.

We consider a system in which atoms in the excited state undergo spontaneous decay to the lower states $|b\rangle$ and $|c\rangle$ with corresponding rates Γ_{ab} and $\Gamma_{ac} = \Gamma_a - \Gamma_{ab}$, where Γ_a is the natural linewidth of the state $|a\rangle$. A schematic of the relevant energy level structure is shown in Fig. 3.1. As atoms decay from $|b\rangle$ down to $|g\rangle$, they emit fluorescent light of frequency ω_{bg}. The LSM involves both the simulation and measurement of the spectral lineshape of the $g \to a$ transition. In this context, the "spectral lineshape" refers to the probability of emission of fluorescent light of frequency ω_{bg} as a function of laser frequency ω. Although polarizabilities α_g and α_a depend on ω, we assume that they are effectively constant for $\omega \approx \omega_{ag}$. The LSM can be applied to any atomic system with the energy level structure shown in Fig. 3.1.

3.2 Spectral lineshape

The ac Stark shifts cause the resonant frequency of the $g \to a$ transition to shift as atoms travel through the standing wave. As a result, the spectral lineshape depends heavily on the details of the light field. Because the light field amplitude $E(\mathbf{r})$ is not spatially uniform [see Eq. (3.2) and the discussion thereafter], an atom with coordinate $\mathbf{r}(t)$ will experience a time-dependent electric field in its rest frame.

Assuming constant velocity, the atom's position is $\mathbf{r}(t) = \mathbf{v}t + \mathbf{r}_0$ where $\mathbf{v}$ is the atomic velocity and $\mathbf{r}_0$ is the position of the atom when $t = 0$. The origin O is chosen to be at one of the nodes of the standing wave. A diagram of the geometry is shown in Fig. 3.2. The

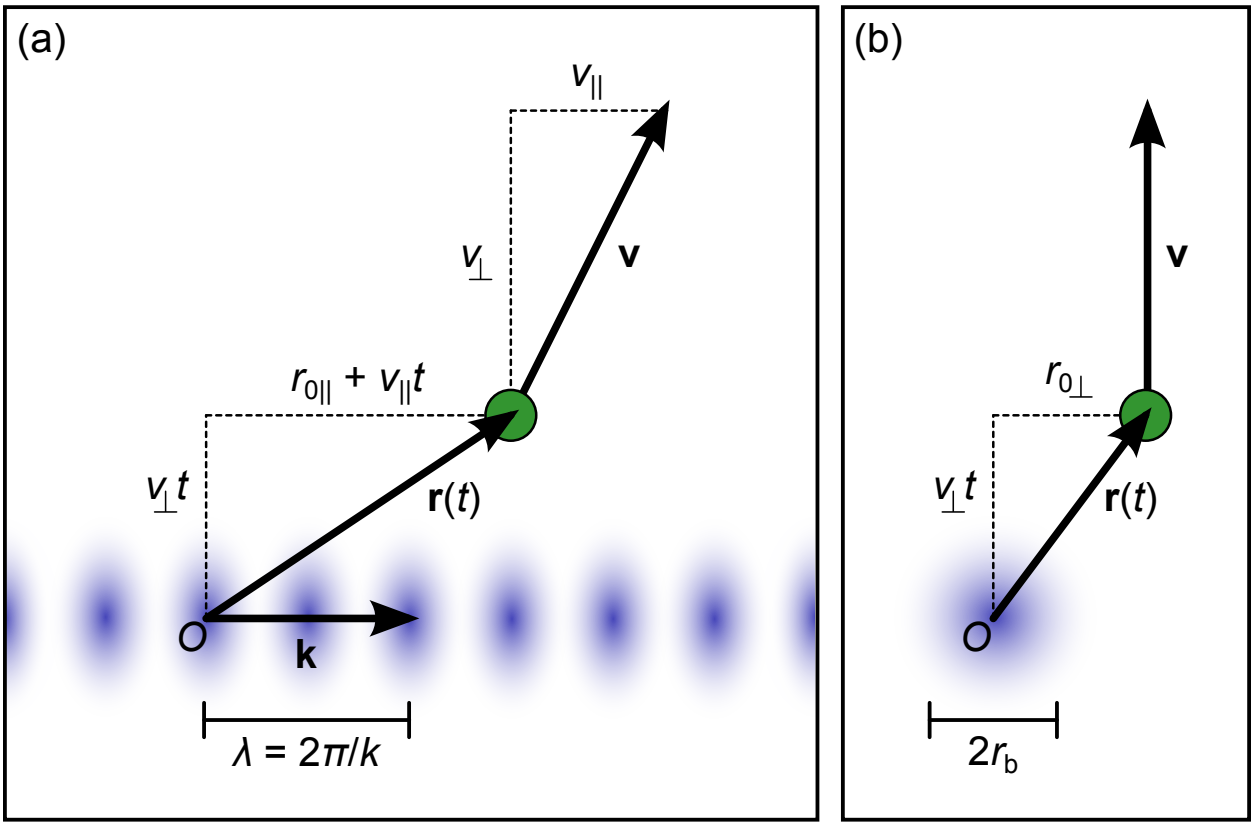

Figure 3.2: Parameters of atomic trajectory. The atom's position $\mathbf{r}(t)$ and velocity $\mathbf{v}$ are shown for some time $t > 0$ and have been projected onto two planes: (a) the plane formed by the vectors $\mathbf{k}$ and $\mathbf{v}$, where $\mathbf{k}$ is the wave-vector of the standing wave of light, and (b) the plane normal to $\mathbf{k}$ and containing the origin O. A contour plot of the spatial extent of the light intensity is shown for reference; white and purple indicate minimal (zero) and maximal intensity, respectively. Here $r_{0||}$ and $r_{0\perp}$ correspond to the components of $\mathbf{r}(t)$ that are parallel and perpendicular to $\mathbf{k}$ when $t = 0$.

time-dependent field experienced by the atom is given by

$$\mathcal{E}[\mathbf{r}(t)] = \mathcal{E}_0 \cos(kv_\parallel t + kr_{0\parallel})\, e^{-(v_\perp^2 t^2 + r_{0\perp}^2)/r_\mathrm{b}^2}, \tag{3.10}$$

where $\mathcal{E}(\mathbf{r})$ is given by Eq. (3.2). Here $v_\parallel = \hat{\mathbf{k}} \cdot \mathbf{v}$ and $v_\perp = |\mathbf{v} - \hat{\mathbf{k}}\, v_\parallel|$ are the components of the velocity that are perpendicular and parallel to $\mathbf{k}$. Similarly, $r_{0\parallel}$ and $r_{0\perp}$ correspond to the perpendicular and parallel components of the position $\mathbf{r}_0$.

The total time dependence of the electric field in Eq. (3.1) is due to the fast oscillation of the light at frequency ω and the slow modulation of the amplitude with a frequency $kv_\parallel$. The amplitude modulation is additionally characterized by a temporal Gaussian envelope with a characteristic width $r_\mathrm{b}/v_\perp$, which is the amount of time an atom spends within the radius of the standing wave. We consider non-relativistic atoms for which the conditions $\omega \gg kv_\parallel$ and $\omega \gg v_\perp/r_\mathrm{b}$ are valid, and the optical oscillations are much faster than the modulation of the amplitude $\mathcal{E}[\mathbf{r}(t)]$. In this case, the ac Stark shift is obtained by substituting Eq. (3.10) into Eq. (3.7).

Absorption profile

In order to gain a qualitative understanding of the physics, we make the simplifying assumption

$$\mathcal{E}(t) \approx \mathcal{E}_0 \cos(kv_\parallel t). \tag{3.11}$$

In this case, the Stark shifts of the ground and excited states lead to the following shift of the resonant energy of the $g \to a$ transition:

$$\omega_\mathrm{ac}(a) - \omega_\mathrm{ac}(g) = -\alpha_{ag} (\mathcal{E}_0/2)^2 \cos^2(kv_\parallel t), \tag{3.12}$$

where

$$\alpha_{ag} \equiv \alpha_a - \alpha_g, \tag{3.13}$$

is the difference of the polarizabilities of the ground and excited states. From an atom's perspective, this is equivalent to a polarizability-dependent frequency modulation of the two counterpropagting light fields. Thus, the features of the $g \to a$ lineshape can be understood by studying a related system: stationary atoms with fixed energy levels in the presence of two counter-propagating, frequency-modulated electric fields. In this subsection, we turn our attention to such a system.

The frequency-modulated electric fields have instantaneous frequencies ω_+ and ω_- given by

$$\omega_\pm(t) = \omega \pm kv_\parallel + \omega_\mathrm{m} A_\mathrm{m} \cos(\omega_\mathrm{m} t), \tag{3.14}$$

where

$$\omega_\mathrm{m} \equiv 2kv_\parallel \quad \text{and} \quad A_\mathrm{m} \equiv \frac{\alpha_{ag} \mathcal{E}_0^2}{16\hbar k v_\parallel}, \tag{3.15}$$

are the modulation frequency and modulation index, respectively. Equation (3.14) includes the term $\pm kv_\parallel$ which accounts for the Doppler shifts of the frequencies of the two

counter-propagating waves. To derive Eq. (3.14), we used a trigonometric identity to write $\cos^2(kv_\parallel t) = (1/2)[1 + \cos(2kv_\parallel t)]$ and we neglected the time-independent term because it can be interpreted as an overall shift of the optical frequency: $\omega \to \omega + \omega_{\rm m} A_{\rm m}$. The instantaneous frequency $\omega_\pm(t)$ is characteristic of a light field with a time-dependent phase [104]. Such a field is given by

$$\mathcal{E}_\pm = (1/2)\mathcal{E}_0 e^{i[(\omega \pm kv_\parallel)t + A_{\rm m}\sin(\omega_{\rm m} t)]}, \tag{3.16}$$

where the factor of 1/2 is included so that the total field, which is the sum of two traveling waves, has an amplitude of $\mathcal{E}_0$. Note that the instantaneous frequency is the time derivative of the argument of $\mathcal{E}_\pm$. The effective field $\mathcal{E}_\pm$ can be decomposed in the following way:

$$\mathcal{E}_\pm = \sum_{n=-\infty}^{\infty} (1/2)\mathcal{E}_0 J_n(A_{\rm m}) e^{i(\omega \pm kv_\parallel + n\omega_{\rm m})t}, \tag{3.17}$$

where J_n are Bessel functions of the first kind. Thus the effective field consists of a principal field ($n = 0$) which oscillates at a frequency $\omega \pm kv_\parallel$, and infinitely many sidebands ($n \neq 0$) which oscillate at frequencies $\omega \pm kv_\parallel + n\omega_{\rm m}$. The amplitude of the electric field of nth sideband is $(1/2)\mathcal{E}_0 J_n(A_{\rm m})$.

The total electric field $\mathcal{E}_{\rm tot}$ seen by the atom is the sum of the two counter-propagating light fields. To add the fields, the summation index in Eq. (3.17) is changed from n to $n+1$ and the field $\mathcal{E}_-$ is expressed as

$$\mathcal{E}_- = \sum_{n=-\infty}^{\infty} (1/2)\mathcal{E}_0 J_{n+1}(A_{\rm m}) e^{i(\omega + kv_\parallel + n\omega_{\rm m})t},$$

where $-kv_\parallel + \omega_{\rm m} = +kv_\parallel$ because the modulation frequency $\omega_{\rm m}$ is exactly twice the Doppler shift. Hence the sidebands of the two counter-propagating waves overlap and the total field is given by

$$\mathcal{E}_{\rm tot} = \mathcal{E}_+ + \mathcal{E}_- = \sum_{n=-\infty}^{\infty} \tilde{\mathcal{E}}_n e^{i\omega_n t}, \tag{3.18}$$

where

$$\tilde{\mathcal{E}}_n \equiv \frac{\mathcal{E}_0}{2}[J_{n+1} + J_n] \quad \text{and} \quad \omega_n \equiv \omega + kv_\parallel + 2n\, kv_\parallel. \tag{3.19}$$

In particular, the first-order sidebands from one field correspond with the carrier of the other [107], resulting in an absorption profile with a polarizability-dependent distortion. The "absorption profile" is a plot of the transition rate as a function of ω.

The rate of the $g \to a$ transition is given by

$$\mathcal{R} = \sum_{n=-\infty}^{\infty} \frac{2\pi}{\hbar^2} \left| d_{\rm in} \tilde{\mathcal{E}}_n \right|^2 \frac{\Gamma_a/2\pi}{(\omega_n - \omega_{ag})^2 + (\Gamma_a/2)^2}. \tag{3.20}$$

Equation (3.20) is valid in the electroweak excitation limit, that is, when the excitation rate $\mathcal{R}$ is much smaller than all other relevant rates. To derive Eq. (3.20), we neglected

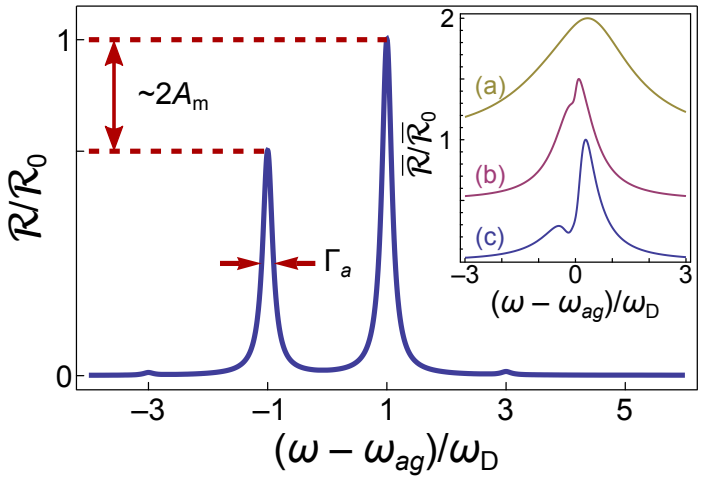

Figure 3.3: Absorption profile. Shown is a plot of the transition rate $\mathcal{R}$ as a function of the laser frequency ω for the case of a single atom with parallel speed $v_\parallel = \omega_{\rm D}/k$, where $\omega_{\rm D}$ is the Doppler broadening of the line. The transition rate is normalized by $\mathcal{R}_0$ to have a maximum value of unity. Here the modulation index satisfies $A_{\rm m} < 0$. For $A_{\rm m} > 0$, the peak on the left is taller than the peak on the right. In the insert, the average transition rate $\overline{\mathcal{R}}$ is shown in three cases: (a) the condition $\Gamma_a/4 \ll \omega_{\rm D}$ is violated, (b) the condition $\hbar\omega_{\rm D} \lesssim |\alpha_{ag}|E_0^2$ is violated, and (c) both conditions in Eq. (3.22) are satisfied. To generate these curves, we made use of the approximation $k \approx k_{ag}$ which is valid in the near-resonant regime ($\omega \approx \omega_{ag}$).

the interference of different harmonic components, *e.g.*, $\tilde{\mathcal{E}}_n e^{i\omega_n t}$ and $\tilde{\mathcal{E}}_{n'} e^{i\omega_{n'} t}$. Such terms contribute small corrections to the transition rate which do not affect the qualitative behavior of the absorption profile. A plot of the absorption profile is given in Fig. 3.3. The single-atom absorption profile is clearly asymmetric about the atomic resonance ($\omega = \omega_{ag}$).

For an ensemble of atoms, the absorption profile is obtained by averaging the transition rate (3.20) over the velocity distribution. The average rate is

$$\overline{\mathcal{R}} \equiv \int_{-\infty}^{\infty} \mathcal{R}(v_\parallel)\, w_{\rm L}(v_\parallel, v_{\rm C})\, dv_\parallel, \tag{3.21}$$

where $w_{\rm L}(v_\parallel, v_{\rm C})$ is the appropriate probability distribution for the parallel velocity $v_\parallel$, and $v_{\rm C}$ is a characteristic speed in the $\hat{\mathbf{k}}$ direction. A plot of the average transition rate is shown in the insert of Fig. 3.3. For the insert, $w_{\rm L}(v_\parallel, v_{\rm C})$ is taken to be a Lorentzian distribution with a full-width at half the maximum value (FWHM) of $v_{\rm C} = \omega_{\rm D}/k$, where $\omega_{\rm D}$ is the overall Doppler broadening of the line. The resulting absorption profile is similar to experimentally observed lineshapes in Yb (Section 3.3).

The absorption profile exhibits a polarizability-dependent feature: a dip that separates the profile into two distinct peaks. The sign of the polarizability α_{ag} determines whether the

peak on the left is larger or smaller than the peak on the right. The following conditions need to be met in order for the distortion to be observed:

$$\Gamma_a/4 \ll \omega_{\mathrm{D}} \quad \text{and} \quad \hbar\omega_{\mathrm{D}} \lesssim |\alpha_{ag}|\mathcal{E}_0^2. \tag{3.22}$$

The former condition ensures that the sidebands of the FM waves can be resolved. The latter ensures that the amplitude of the first-order sidebands is not negligible compared to the amplitude of the carrier, that is, $A_{\mathrm{m}} \neq 0$ for $v_{\parallel} \approx v_{\mathrm{C}}$. If either $\omega_{\mathrm{D}} \lesssim \Gamma_a/4$ or $\hbar\omega_{\mathrm{D}} \gg |\alpha_{ag}|\tilde{\mathcal{E}}_0^2$, then the asymmetric distortion will be suppressed, as can be seen in the insert of Fig. 3.3. In this case, the methods described here cannot be used to measure the polarizability α_{ag}. However, the LSM can still be used to measure α_{ag} in the absence of the distortion by comparing displacements of the central peak of the lineshape.

By omitting the Gaussian envelope $\exp(-v_\perp^2 t^2/r_{\mathrm{b}}^2)$ in Eq. (3.11), we neglect effects of the atom's finite transit time, such as broadening of the spectral line [36]. Nonetheless, the transit time must satisfy the following restrictions:

$$v_\perp/r_{\mathrm{b}} \lesssim d_{\mathrm{in}}\mathcal{E}_0/\hbar \quad \text{and} \quad v_\perp/r_{\mathrm{b}} \ll \omega_{\mathrm{D}}, \tag{3.23}$$

where $d_{\mathrm{in}}\mathcal{E}_0/\hbar$ is the Rabi frequency of the $g \to a$ transition. The former condition represents a system in which atoms have enough time to undergo excitation to the upper state $|a\rangle$, as will be discussed in Section 3.2. The latter condition ensures that the Doppler broadening is sufficiently large that most atoms travel through many nodes and antinodes of the standing wave during their transit.

Although the absorption profile provides a satisfactory illustration of the physics, it cannot be used to measure the ac polarizabilities. The transition rate presented in Eq. (3.20) is valid only in the electroweak excitation limit and therefore cannot account for saturation effects. Moreover, Eq. (3.20) does not properly take into account interference of different probability amplitudes, nor does it include finite transit-time effects. A more complete picture is required to generate a theoretical lineshape that can be fitted to experimental data. Such a picture is achieved by the following model.

Fluorescence probability

Hereafter, we return our attention to the original system: moving atoms illuminated by light with a fixed frequency ω. The spectral lineshape of the $g \to a$ transition is modeled by computing the probability of emission of fluorescent light of frequency ω_{bg} as a function of laser frequency ω. The computation involves three steps. First, the time-dependent population ρ_{bb} of the state $|b\rangle$ is computed by numerically solving the optical Bloch equations (OBE) for the case of atoms traveling through a non-uniform field (see Fig. 3.2). Second, the probability of fluorescence $\mathcal{F}$ is determined by integrating the time-dependent decay rate $\Gamma_b\rho_{bb}$ with respect to time. Finally, the average fluorescence probability $\overline{\mathcal{F}}$ is computed by taking a weighted average of $\mathcal{F}$ with respect to the atomic velocity $\mathbf{v}$ and the offset $\mathbf{r}_0$.

Although the LSM can be used in conjunction with any atomic source, our model makes use of distributions that are appropriate for a collimated beam of thermal atoms traveling in a direction that is orthogonal to the standing wave. In this case, $v_\perp$ represents the component of the atom's velocity along the atomic beam, and $v_\parallel/v_\perp$ represents the angular spread of the beam. The corresponding velocity distribution is

$$w(\mathbf{v}) = w_{\mathrm{T}}(v_\perp, v_{\mathrm{T}})\, w_{\mathrm{L}}(v_\parallel, v_{\mathrm{C}}), \tag{3.24}$$

where

$$w_{\mathrm{T}}(v_\perp, v_{\mathrm{T}}) = 2(v_\perp^3/v_{\mathrm{T}}^4)e^{-(v_\perp/v_{\mathrm{T}})^2}, \tag{3.25}$$

is the distribution of velocities appropriate for thermal atoms escaping from a hole, and $w_{\mathrm{L}}(v_\parallel, v_{\mathrm{C}})$ is the velocity distribution appropriate for a collimated atomic beam. Here $v_{\mathrm{T}} = \sqrt{2k_BT/M}$ is the thermal speed of the atom, T is the temperature of the oven, M is the atom's mass, k_B is Boltzmann's constant, and v_{C} is the characteristic speed determined by the atomic-beam collimator. To model the effects of a vane collimator, we approximate the spread of parallel velocities by a Lorentzian distribution with a FWHM of $v_{\mathrm{C}} = \omega_{\mathrm{D}}/k$, where ω_{D} is the overall Doppler broadening of the line.

In the following model, we use dimensionless parameters. Dimensionless parameters ease computation, and potentially facilitate the application of the model to several different atomic systems. Throughout, we make the approximation $k \approx k_{ag}$ which is valid in the near-resonant regime ($\omega \approx \omega_{ag}$).

Time is measured in units $1/\Gamma_a$. We define the dimensionless time $\tau \equiv \Gamma_a\, t$ and decay rates $G_b \equiv \Gamma_b/\Gamma_a$, $G_c \equiv \Gamma_c/\Gamma_a$, $G_{ab} = \Gamma_{ab}/\Gamma_a$, and $G_{ac} = 1 - G_{ab}$. We further define the dimensionless perpendicular and parallel velocities $u_\perp \equiv v_\perp/v_{\mathrm{T}}$ and $u_\parallel \equiv v_\parallel/v_{\mathrm{C}}$, and the dimensionless perpendicular and parallel offsets $\xi \equiv r_{0\perp}/r_{\mathrm{b}}$ and $\varphi \equiv kr_{0\parallel}$, respectively.

Consistent with the discussion in Section 3.2, we introduce the following dimensionless parameters: the saturation parameter S_0, characteristic modulation index S_1, and Doppler parameter S_2, defined by

$$S_0 \equiv \left[d_{\mathrm{in}}\mathcal{E}_0/(\hbar\Gamma_a)\right]^2, \tag{3.26}$$

$$S_1 \equiv \alpha_{ag}\mathcal{E}_0^2/(16\hbar\omega_{\mathrm{D}}), \tag{3.27}$$

and

$$S_2 \equiv 2\omega_{\mathrm{D}}/\Gamma_a, \tag{3.28}$$

respectively. We define an additional parameter S_3 by

$$S_3 \equiv v_{\mathrm{T}}/(r_{\mathrm{b}}\Gamma_a). \tag{3.29}$$

Note that $r_{\mathrm{b}}/v_\perp$ is the time that an atom spends within the radius of the light field and hence $1/(S_3\, u_\perp)$ represents the dimensionless transit time.

In terms of the dimensionless parameters, the conditions presented in expressions (3.22) reduce to $S_2 \gg 1/2$ and $|S_1| \gtrsim 1/16$. When either of these conditions is violated, the

characteristic dip in the lineshape is suppressed, as can be seen in Fig. 3.4. Likewise, conditions (3.23) reduce to $S_3 \lesssim \sqrt{S_0}$ and $S_3 \ll (1/2)S_2$. Whereas the absorption profile discussed in Section 3.2 was valid only in the weak excitation limit ($S_0 \ll 1$), the model of the fluorescence can accommodate large saturation parameters.

Let ρ_{nm} be the elements of the density matrix in the atom's rest frame for states $n, m \in \{g, a, b, c\}$. We assume that the rotating wave approximation holds and dynamic interactions between states other than $|g\rangle$ and $|a\rangle$ can be neglected. In this case, the dimensionless optical Bloch equations (OBE) for the configuration shown in Fig. 3.1 are [84]

$$\dot{\rho}_{aa} = -\frac{i}{2}\Omega(\rho_{ag} - \rho_{ga}) - \rho_{aa}, \tag{3.30a}$$

$$\dot{\rho}_{ag} = +\frac{i}{2}\Omega(\rho_{gg} - \rho_{aa}) - \frac{1}{2}(1 - 2i\Delta)\rho_{ag}, \tag{3.30b}$$

$$\dot{\rho}_{bb} = -G_b\rho_{bb} + G_{ab}\rho_{aa}, \tag{3.30c}$$

$$\dot{\rho}_{cc} = -G_c\rho_{cc} + G_{ac}\rho_{aa}, \tag{3.30d}$$

where $\dot{\rho}_{nm} = d(\rho_{nm})/d\tau$. The remaining density matrix elements ρ_{gg} and ρ_{ga} are determined from $\sum_n \rho_{nn} = 1$ and $\rho_{ga} = \rho^*_{ag}$. Here

$$\Omega \equiv \frac{1}{\Gamma_a}\left[\frac{\langle a|\mathbf{d}\cdot\boldsymbol{\epsilon}|g\rangle\mathcal{E}(t)}{\hbar}\right] = \sqrt{S_0}\, f(\boldsymbol{\xi}, \mathbf{u}), \tag{3.31}$$

is the Rabi frequency,

$$\Delta \equiv \frac{1}{\Gamma_a}\left[\omega - \frac{\omega(a) - \omega(g)}{\hbar}\right] = \delta + 2S_1S_2\, f(\boldsymbol{\xi}, \mathbf{u})^2, \tag{3.32}$$

is the detuning of the laser light from the resonance, $\delta \equiv (\omega - \omega_{ag})/\Gamma_a$, and the function $f(\boldsymbol{\xi}, \mathbf{u})$ is defined by

$$f(\boldsymbol{\xi}, \mathbf{u}) \equiv \cos[(S_2/2)u_\parallel\tau + \varphi]e^{-[(S_3u_\perp\tau)^2 + \xi^2]}, \tag{3.33}$$

where $\boldsymbol{\xi} = (\varphi, \xi)$ and $\mathbf{u} = (u_\parallel, u_\perp)$. We further assume that all atoms initially occupy the ground state.

The probability that an atom will emit fluorescent light of frequency ω_{bg} in a time interval $[\tau_\mathrm{i}, \tau_\mathrm{f}]$ is given by

$$\mathcal{F} = \int_{\tau_\mathrm{i}}^{\tau_\mathrm{f}} G_b\, \rho_{bb}(\tau)\, d\tau, \tag{3.34}$$

where $G_b\, \rho_{bb}(\tau)$ is the time-dependent rate of the $b \to g$ decay. The choice of integration interval $[\tau_\mathrm{i}, \tau_\mathrm{f}]$ depends on both the transit time and the characteristic time of the fluorescent decay after the atoms leave the light field. In the case where the $a \to b \to g$ decay time is shorter than the transit time, it is appropriate to define the integration limits by $-\tau_\mathrm{i} = \tau_\mathrm{f} = 3/(S_3\, u_\perp)$. The factor of 3 ensures that the atom is "far" from the standing wave at the

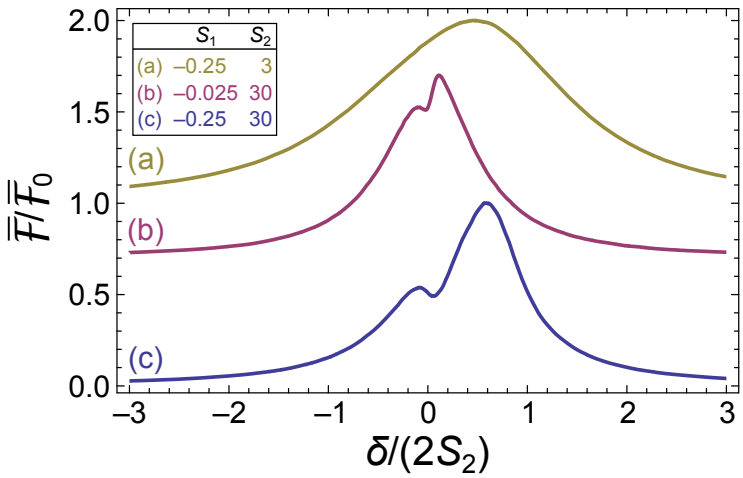

Figure 3.4: Results of simulation. The simulated lineshape $\overline{\mathcal{F}}(\delta)$ is shown for two different values each of the modulation index S_1 and the Doppler parameter S_2, as indicated by the insert: (a) the condition $S_2 \gg 1/2$ is violated, (b) the condition $|S_1| \gtrsim 1/16$ is violated, and (c) both conditions are satisfied. For each curve, the saturation parameter is $S_0 = 1.0$. The lineshapes are normalized by the maximum peak height $\overline{\mathcal{F}}_0$. To ease comparison, the middle and top curves are shifted vertically by 0.7 and 1.0, respectively.

integration limits. To model a system with slower decays, the integration limit τ_f must be extended.

The fluorescence probability depends on the parameters of the atomic trajectory, that is, $\mathcal{F} = \mathcal{F}(\boldsymbol{\xi}, \mathbf{u})$. We define the average probability of fluorescence by

$$\overline{\mathcal{F}} = \iint \mathcal{F}(\boldsymbol{\xi}, \mathbf{u})\, w(\boldsymbol{\xi}, \mathbf{u})\, d\boldsymbol{\xi}\, d\mathbf{u}, \tag{3.35}$$

where $w(\boldsymbol{\xi}, \mathbf{u})$ is the probability distribution associated with the atom's initial position and velocity. In our model, we assume $w(\boldsymbol{\xi}, \mathbf{u}) = w_1(\boldsymbol{\xi})\, w_2(\mathbf{u})$, where the distribution w_1 is a uniform distribution over the intervals $\xi \in [-3, 3]$ and $\varphi \in [-\pi, \pi]$. The finite integration limits are justified by the following properties of the system: First, the amplitude of the standing wave drops to less than 0.01% of its maximum value when $|\xi| > 3$. Therefore, atoms will only pass through the light if $|\xi| \lesssim 3$. Second, φ constitutes a phase shift of the electric field which is unique only for $\varphi \in [-\pi, \pi]$. Consistent with Eqs. (3.24) and (3.25), the velocity distribution satisfies $w_2(\mathbf{u}) = w_\mathrm{T}(u_\perp, 1) w_\mathrm{L}(u_\parallel, 1)$, where $w_\mathrm{T}(u_\perp, 1)$ is the velocity distribution for atoms escaping from a hole with unit thermal speed, and $w_\mathrm{L}(u_\parallel, 1)$ is a Lorentzian distribution with FWHM of 1.

The fluorescence probability is a function of the detuning δ from the atomic resonance, that is,

$$\overline{\mathcal{F}} = \overline{\mathcal{F}}(\delta; \mathbf{S}, \mathbf{G}), \tag{3.36}$$

where $\mathbf{S} \equiv (S_0, S_1, S_2, S_3)$ and $\mathbf{G} \equiv (G_{ab}, G_b, G_c)$ are parameters. We refer to a plot of $\overline{\mathcal{F}}(\delta; \mathbf{S}, \mathbf{G})$ as a function of δ as the "simulated lineshape" of the $g \to a$ transition. Three such plots are shown in Fig. 3.4. In Fig. 3.4, curves (a) and (b) demonstrate the suppression of the polarizability-dependent distortion when either the Doppler parameter S_2 or the modulation index S_1 is too small. The distortion is most pronounced in curve (c), for which $S_2 \gg 1/2$ and $|S_1| \gtrsim 1/16$. The simulated lineshapes in Fig. 3.4 are qualitatively similar to the absorption profiles in the insert of Fig. 3.3, as expected.

Numerical procedure

The numerical procedures described here are valid for a variety of atomic species. However, the simulations were performed with parameter values appropriate for the Yb system described in Section 3.3.

We used a stiffly stable Rosenback method [98] to numerically solve a system of equations related to Eqs. (3.30) and (3.34), with $-\tau_{\rm i} = \tau_{\rm f} = 3/(S_3\, u_\perp)$. This system of equations is described in Appendix B.2. The Rosenback method involves two tolerances–denoted `atol` and `rtol` in Ref. [98]–which were both set to 10^{-5}. The multi-dimensional integral in Eq. (3.35) was computed using an adaptive Monte Carlo routine [98]. In our implementation, the integration routine involves 10^5 evaluations of the integrand. For various values of $\mathbf{S}$, the average estimated error was less than 1% of the value of the integral.

For computational purposes, we restricted the integration to the following finite domain: $\xi \in [-3, 3]$, $\varphi \in [-\pi, \pi]$, $u_\perp \in [0, 3]$, and $u_\parallel \in [-6, 6]$. The subdomains for ξ and φ were discussed after Eq. (3.35). The finite integration subdomains for $u_\parallel$ and $u_\perp$ are justified as follows: Atoms with a large parallel speed $|u_\parallel|$ experience a Doppler shift that is much larger than the characteristic Doppler broadening of the spectral line. Such atoms only contribute to the wings of the lineshape, where $|\delta|$ is large and the probability of fluorescence is very small. Moreover, for a Lorentzian velocity distribution with unit FWHM, $|u_\parallel| \leq 6$ for about 95% of atoms.

On the other hand, atoms with a perpendicular speed that satisfies $u_\perp \gg \sqrt{S_0}/S_3$ are moving so fast that the transit time is much smaller than the inverse Rabi frequency. Such atoms do not spend enough time in the light field for the $g \to a$ transition to be realized. Since most atoms travel at or near the thermal speed $u_\perp = 1$, the condition $\sqrt{S_0}/S_3 \gtrsim 1$ represents a system in which most atoms have enough time to interact with the light. We assume that atoms with speed $u_\perp > 3$ do not contribute significantly to the lineshape. Note that $u_\perp > 3$ for only about 0.1% of atoms. Finally, we ignore counterflow of atoms in the atomic beam by requiring $u_\perp \geq 0$.

For fixed $\mathbf{G} = (0.35, 0.45, 0)$ and $S_3 = 0.53$, we computed the average fluorescence $\overline{\mathcal{F}}(\delta; \mathbf{S}, \mathbf{G})$ for 100 discrete values of $\delta \in [\delta_-, \delta_+]$, and various discrete values of $S_0 \in [0.1, 10]$, $S_1 \in [0.01, 1]$, and $S_2 \in [1, 100]$. Here $\delta_\pm \equiv 2S_1S_2 \pm 3[(1/2)S_2 + G_b + 1]$. The results were interpolated using cubic splines to approximate the continuous function $\overline{\mathcal{F}}(\delta; \mathbf{S}, \mathbf{G})$. Three curves which are typical of those produced by this procedure are presented in Fig. 3.4.

The LSM involves fitting the simulated curve $\overline{\mathcal{F}}(\delta;\mathbf{S},\mathbf{G})$ to the observed lineshape to determine best-fit values of S_0, S_1, and S_2. From the best-fit values, the following three quantities can be calculated: the polarizability difference α_{ag}, the circulating power P of the standing wave,[2]and the Doppler broadening ω_{D} of the $g \to a$ transition which are given by

$$\alpha_{ag} = \left[\frac{8\, d_{\mathrm{in}}^2}{\hbar\, \Gamma_a}\right] \times S_1 S_2 / S_0, \tag{3.37}$$

$$P = \frac{1}{\alpha}\left[\frac{r_{\mathrm{b}} \hbar\, \Gamma_a}{8 d_{\mathrm{in}}}\right]^2 \times S_0, \tag{3.38}$$

and

$$\omega_{\mathrm{D}} = (\Gamma_a/2) \times S_2, \tag{3.39}$$

respectively. Here $\alpha \approx 1/137$ is the fine structure constant. The present implementation of the LSM uses *Mathematica*'s nonlinear regression routine to determine the best-fit values of S_0, S_1, and S_2. Alternatively, Eq. (3.38) can be solved for d_{in} in terms of P and S_0. Thus the LSM can also be used to measure the induced dipole moment when the power is known, as was done in the previous application of the LSM [107].

The treatment of systematic errors and statistical uncertainties is straightforward. In Eq. (3.37), for instance, the uncertainty in the dimensionful quantity $d_{\mathrm{in}}^2/(\hbar\Gamma_a)$ is due solely to systematic effects, whereas the uncertainty in the term $S_1 S_2/S_0$ arises from statistical uncertainties in both the observed signal and the fitting algorithm. The total uncertainty of the quantity α_{ag} is obtained by adding these independent uncertainties in quadrature. If the signal-to-noise ratio (SNR) of the observed lineshape is sufficiently high, then the error of the measurement of α_{ag} will be dominated by the uncertainties of the known quantities d_{in} and Γ_a.

3.3 Application to ytterbium

The electronic structure of Yb is shown in Fig. 3.5. The low-lying energy eigenstates of Yb match the structure shown in Fig. 3.1 under the following mapping: $g = {}^1S_0$, $a = {}^3D_1$, $b = {}^3P_1$, and $c = {}^3P_0$. Therefore, the LSM can be used to measure the difference in ac polarizabilities of the upper state ${}^3D_1$ and the ground state ${}^1S_0$ at 408 nm by analyzing the lineshape of the 408-nm ${}^1S_0 \to {}^3D_1$ transition. In this case, the lineshape is measured by observing the 556-nm fluorescence of the ${}^3P_1 \to {}^1S_0$ decay. The intermediate state ${}^3P_0$ is metastable and hence $\Gamma_c \approx 0$.

[2]The standing wave is formed by two counter-propagating waves of light. The circulating power of the standing wave is defined as the average power of a single traveling wave. The electric field of the wave propagating in the $\pm\hat{\mathbf{k}}$ direction is given by $\mathcal{E}_1(\mathbf{r},t) = (1/2)\mathcal{E}_0 \exp[-(r_\perp/r_{\mathrm{b}})^2]\cos(kr_\parallel \pm \omega t)$. The corresponding time-averaged intensity in SI units is $I(r_\perp) = (1/32\pi\alpha)\mathcal{E}_0^2 \exp[-2(r_\perp/r_{\mathrm{b}})^2]$, where the time average is taken over a single period of oscillation. Therefore, the circulating power of the standing wave is given by $P \equiv \int_0^\infty I(r_\perp)\, 2\pi r_\perp\, dr_\perp = (1/64\alpha) r_{\mathrm{b}}^2 \mathcal{E}_0^2$.

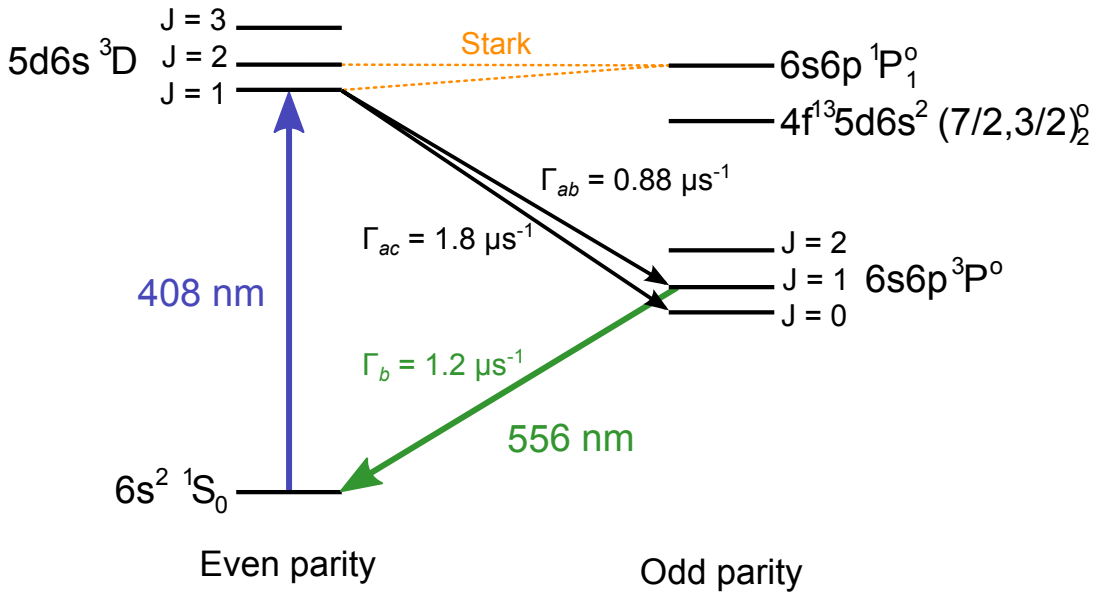

Figure 3.5: Ytterbium energy levels. Shown are the low-lying energy eigenstates of Yb and the electronic transitions relevant to the polarizability experiment.

There is an additional decay of $^3D_1$ to the metastable state $^3P_2$, which is not shown in Fig. 3.1. The state c can represent multiple metastable states, including both $^3P_1$ and $^3P_2$. In this interpretation, Γ_{ac} is the rate of decay of $^3D_1$ to all metastable states.

The highly forbidden $^1S_0 \rightarrow {}^3D_1$ transition is induced by the Stark mixing technique. This technique involves the application of a static, uniform electric field $\mathbf{E}$ which mixes the upper state $^3D_1$ with opposite-parity states, predominantly the $^1P_1$ state. The effective dipole moment d_{in} associated with the Stark-induced transition is given by [107]

$$d_{\text{in}} = \beta_{ag} |(\mathbf{E} \times \boldsymbol{\epsilon})^{(1)}_{-M_a}|, \tag{3.40}$$

where $\beta_{ag} = 2.18(10) \times 10^{-8}\ e \cdot a_0 \cdot (\text{V/cm})^{-1}$ is the vector transition polarizability of the $^1S_0 \rightarrow {}^3D_1$ transition, e is the elementary charge, a_0 is the Bohr radius, and $(\mathbf{E}_{\text{dc}} \times \boldsymbol{\epsilon})^{(1)}$ is a spherical tensor of rank one.[3]Here M_a is the magnetic quantum number of the $^3D_1$ state.

Because the angular momentum of the ground state $^1S_0$ is $J_g = 0$, only the scalar term in Eq. (3.9) contributes to the polarizability of $^1S_0$. That is, $\alpha_g = \alpha_0(^1S_0)$ and so α_g is independent of the geometry of the applied fields. Hence the dependence of α_{ag} on the field

[3]Let $A^{(1)}$ be the rank-one spherical tensor associated with the Cartesian vector $\mathbf{A}$. Then the components of $A^{(1)}$ are given by $A^{(1)}_0 = A_z$ and $A^{(1)}_{\pm 1} = \mp(A_x \pm iA_y)/\sqrt{2}$.

geometry is due entirely to the vector and tensor polarizabilities $\alpha_1(^3D_1)$ and $\alpha_2(^3D_1)$ of the excited state $^3D_1$. In this case, the LSM is sensitive to the difference of the scalar polarizabilities of the ground and excited states. However, the vector and tensor polarizabilities of the excited state can be measured unambiguously by varying the polarization of the standing wave.

A recent calculation [37] of the polarizability of the ground state $^1S_0$ at 408 nm yielded[4]

$$\alpha_0(^1S_0) = 0.570(3)\ \text{Hz} \cdot (\text{V/cm})^{-2}. \tag{3.41}$$

Calculations of the polarizability $^3D_1$ at 408 nm are complicated by the potential existence of odd-parity eigenstates with energy close to twice the energy of a 408-nm photon. Such states could lead to a resonantly enhanced polarizability of the $^3D_1$ state. The energy spectrum in this region (which is below the ionization limit) is very dense due to the excitation of $4f$ orbitals. The knowledge of the energy spectrum is far from complete in this region. This provides one of the motivations for determining the polarizabilities experimentally.

The first implementation of the LSM [107] was used to measure the quantity[5]

$$\alpha^{\text{I}}_{ag} = -0.624(68)\ \text{Hz} \cdot (\text{V/cm})^{-2}, \tag{3.42}$$

were $\alpha^{\text{I}}_{ag} = \alpha_2(^3D_1) + \alpha_0(^3D_1) - \alpha_0(^1S_0)$. Here the superscript "I" is introduced to distinguish this measurement from the results of the present work. To determine the tensor contribution $\alpha_2(^3D_1)$ unambiguously requires a second measurement of a different combination of scalar and tensor polarizabilities. This is accomplished in the present work by the application of a dc electric field that is parallel to the standing wave (Fig. 3.6), whereas the previous measurement was performed with a dc field that was perpendicular to the standing wave. In addition, the current experiment includes a strong magnetic field not present in the previous case. The magnetic field makes possible the measurement of the vector polarizability, as discussed in Section 3.4.

Experimental apparatus and field geometry

The details of the experimental apparatus were reported elsewhere [112], and only a brief description is provided here. A schematic of the setup is shown in Fig. 3.6. A beam of Yb atoms is produced by a stainless-steel oven loaded with Yb metal, operating at 500 °C. The oven is outfitted with a multislit nozzle, and there is an external vane collimator reducing the spread of the atomic beam in the z-direction. Downstream from the collimator, atoms enter a region with three external fields: a uniform, static magnetic field $\mathbf{B}$; a uniform, static electric field $\mathbf{E}$; and a non-uniform, dynamic electric field $\boldsymbol{\mathcal{E}}(\mathbf{r}, t)$.

[4] Equation (3.7) implies that α_{ag} has units of *energy* per squared electric field. However, in this work α_{ag} is normalized by $2\pi\hbar$ and presented in units of *frequency* per squared electric field. For a more thorough discussion of unit conventions, see Ref. [88].

[5] The quantity α^{I}_{ag} presented here is larger than the analogous quantity presented in Ref. [107] by a factor of 2. This difference is due to the fact that we adopt a different convention for the Stark shift than is used in that work.

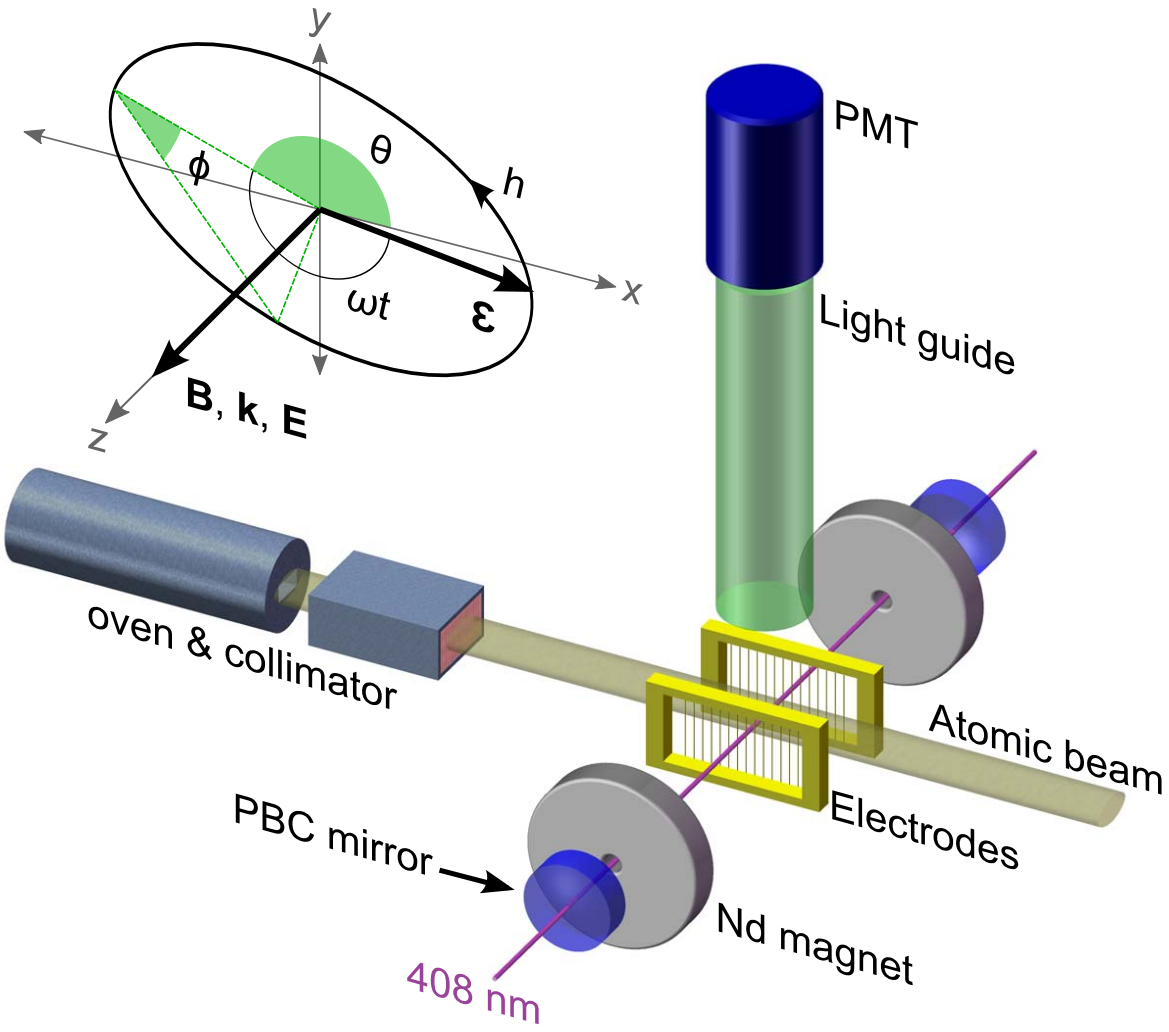

Figure 3.6: Experimental apparatus. A collimated beam of ytterbium atoms interacts with a standing wave of light in the presence of dc electric and magnetic fields. The light is resonant with the 408-nm ${}^1S_0 \rightarrow {}^3D_1$ transition, and the 556-nm fluorescence is detected by the photomultiplier tube (PMT). The neodymium (Nd) magnets are axially magnetized in the z-direction. The standing wave is generated in a power buildup cavity (PBC). With the exception of the PMT, the apparatus is contained in a vacuum chamber.

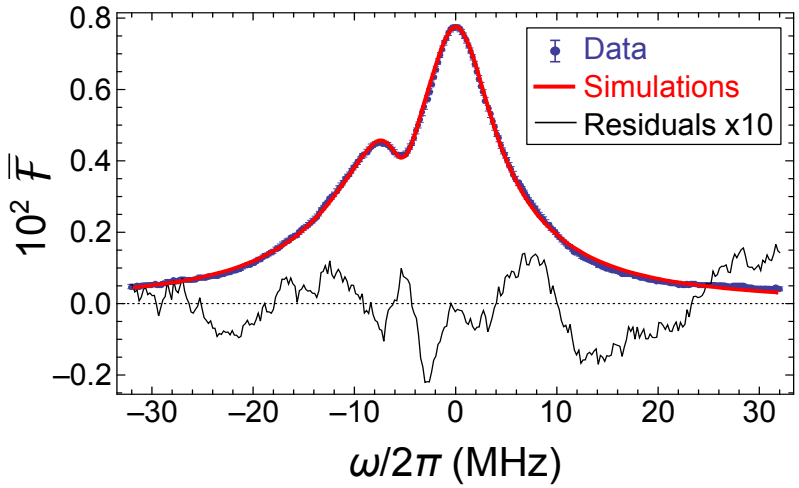

Figure 3.7: Results of fitting program. Shown is a comparison of the observed and the simulated lineshapes of the $^1S_0 \rightarrow {}^3D_1$ transition. The data correspond to Run 3 in Table 3.1. Also shown are the residuals, magnified by a factor of 10. The residuals are the difference of the data and the simulation.

The magnetic field $\mathbf{B}$ is generated by a pair of axially magnetized neodymium (Nd) magnets. These magnets produce a field with sufficient strength (more than 50 G) to completely isolate the Zeeman sublevels of the upper state $^3D_1$. The electric field $\mathbf{E}$ is generated by two wire-frame electrodes separated by 2 cm. The ac electric field $\boldsymbol{\mathcal{E}}(\mathbf{r},t)$ is due to standing-wave light at the transition wavelength of 408.346 nm in vacuum, which is produced by doubling the frequency of the output of a Ti:sapphire laser (Coherent 899). About 7 mW of 408-nm light is coupled into a power buildup cavity (PBC) with finesse of approximately 15,000. The PBC is an asymmetric cavity with a flat input mirror and a curved back mirror with a 50-cm radius of curvature. The separation between the mirrors is 22 cm. Fluorescent light with a wavelength of 556 nm is collected with a light guide and detected with a photomultiplier tube (PMT). With the exception of the PMT, the entire apparatus is contained within a vacuum chamber with a residual gas pressure of 3×10^{-6} Torr.

As can be seen in Fig. 3.6, the fields $\mathbf{B}$ and $\mathbf{E}$ point in the $\hat{\mathbf{z}}$ direction. Likewise, the standing wave is oriented along the z-axis. The light field $\boldsymbol{\mathcal{E}}(\mathbf{r},t)$ lies in the xy-plane. For this geometry, the transition to the upper state $|^3D_1; M_a = 0\rangle$ is suppressed.

The polarization of the light field is of the form $\boldsymbol{\epsilon} = \epsilon_x\,\hat{\mathbf{x}} + \epsilon_y\,\hat{\mathbf{y}}$, where $|\epsilon_x|^2 + |\epsilon_y|^2 = 1$. To further characterize the polarization, we introduce three parameters: polarization angle θ, degree of ellipticity ϕ, and handedness h, which are given by [4]

$$\tan 2\theta = 2\,\mathrm{Re}(\epsilon_x\epsilon_y^*)/(|\epsilon_x|^2 - |\epsilon_y|^2), \tag{3.43}$$

$$\sin 2\phi = 2\,|\mathrm{Im}(\epsilon_x\epsilon_y^*)| = |i(\boldsymbol{\epsilon}\times\boldsymbol{\epsilon}^*)\cdot\hat{\mathbf{z}}|, \tag{3.44}$$

Table 3.1: Summary of results. The uncertainty in the fitted parameters is the asymptotic standard error returned by the fitting algorithm.

Run	$c_0 \cdot 10^2$	$c_1 \cdot 10^2$	S_0	S_1	S_2	$S_1 S_2 / S_0$
1	5.1(1)	5.5(4)	2.83(17)	-0.208(3)	34(1.1)	-2.53(16)
2	5.0(1)	3.2(3)	2.76(16)	-0.215(3)	30(1.1)	-2.33(17)
3	5.4(1)	7.0(3)	2.68(12)	-0.187(2)	34(1.0)	-2.35(13)
4	5.0(1)	4.7(3)	2.56(17)	-0.195(3)	29(1.1)	-2.22(17)
Avg.:			2.70(7)	-0.199(1)	31.8(5)	-2.36(8)

and

$$h = -\mathrm{sgn}[i(\boldsymbol{\epsilon} \times \boldsymbol{\epsilon}^*) \cdot \hat{\mathbf{z}}]. \tag{3.45}$$

Linearly, circularly, and elliptically polarized light are described by $\phi = 0$, $\phi = \pi/4$, and $0 < \phi < \pi/4$, respectively. The sense of rotation is determined by h: left and right-handed polarizations correspond to $h = +1$ and $h = -1$, respectively. Substituting $\mathbf{E} = E\,\hat{\mathbf{z}}$ and $\boldsymbol{\epsilon} = \epsilon_x\,\hat{\mathbf{x}} + \epsilon_y\,\hat{\mathbf{y}}$ into Eqs. (3.40) and (3.9) yields

$$d_{\mathrm{in}} = \beta_{ag} E \sqrt{(1/2)[1 + h M_a \sin(2\phi)]}, \tag{3.46}$$

and

$$\alpha_a = \alpha_0(^3D_1) - h M_a \sin(2\phi)\alpha_1(^3D_1) - \frac{1}{2}\alpha_2(^3D_1), \tag{3.47}$$

for $M_a = \pm 1$. Here we have used Eqs. (3.44) and (3.45) to eliminate ϵ_x and ϵ_y in favor of the degree of ellipticity ϕ and the handedness h. For this geometry, both d_{in} and α_a are independent of the polarization angle θ.

According to the geometry in Fig. 3.6, the component of the atom's velocity that is perpendicular to the standing wave is $v_\perp = (v_x^2 + v_y^2)^{1/2}$. The output of the oven is about 6 mm in the y-direction, and is located more than 20 cm away from the standing wave. In order for an atom to pass through the standing wave, its velocity components must satisfy $|v_y/v_x| \leq 0.015$. Therefore, the approximation $v_\perp = v_x$ is valid and the use of the thermal distribution given in Eq. (3.25) is justified. However, for a high-precision measurement, the effect of this approximation needs to be investigated.

Data analysis

The data were acquired over four separate experiments (runs). During each run, approximately 2000 lineshapes were recorded at a rate of about 100 ms per lineshape and an average lineshape was computed. This procedure resulted in 4 lineshapes, each with an effective integration time of about 200 s. A typical lineshape is shown in Fig. 3.7. After fitting the theoretical model to the data, the statistical uncertainties of each run were scaled to give a reduced χ^2 of unity. The scale factor varied between 4.0 and 4.7 depending on the run. The resulting error bars are shown in the figure. The relatively large scale factor indicates that

the accuracy of the fit is dominated by either systematic distortion of the profile during the scan, or profile features that are neglected in the theoretical model, but not by the statistical uncertainty of the signal.

In the present experiment, the oven temperature was $T = 500(50)$ °C and the magnitude of the dc electric field was $E = 4.24(6)$ kV/cm. The atoms intersect the standing wave in the middle of the PBC where the radius of the light beam is $r_{\rm b} = 196(5)$ μm. We used linearly polarized light with $\phi = 0(1)°$. Then Eqs. (3.37) through (3.39) become

$$\alpha_{ag}^{\rm II} = [0.134(17)\ {\rm Hz}\cdot({\rm V/cm})^{-2}] \times S_1 S_2/S_0, \tag{3.48}$$

$$P = [5.02(98)\ {\rm W}] \times S_0, \tag{3.49}$$

and

$$\omega_{\rm D} = [2\pi \times 0.209(17)\ {\rm MHz}] \times S_2, \tag{3.50}$$

where $\alpha_{ag}^{\rm II} = \alpha_0(^3D_1) - (1/2)\alpha_2(^3D_1) - \alpha_0(^1S_0)$. Here the superscript "II" is used to distinguish the results of the present work from the previous measurement. The dimensionless decay rates are $G_{ab} = 0.35(4)$, $G_b = 0.45(4)$, and $G_c = 0$, and the parameter S_3 is given by $S_3 = 0.53(5)$.

As part of our analysis, we normalized the observed and simulated lineshapes by their maximum values. In addition, we introduced two calibration parameters to the simulated curve:

$$\overline{\mathcal{F}}(x; \mathbf{S}, \mathbf{G}, \mathbf{c}) = (1 + c_0)\overline{\mathcal{F}}((1 - c_1)x; \mathbf{S}, \mathbf{G}) - c_0, \tag{3.51}$$

where $\mathbf{c} = (c_0, c_1)$. Here c_0 accounts for the background of the observed signal. The parameter c_1 is a scaling factor that accounts for any variation in the calibration of the frequency axis of the data relative to the simulation. Such deviations could arise due to misalignment of the atomic beam relative to the axis of the PBC, deviations in the perpendicular velocity distribution, or the uncertainty of the timescale $1/\Gamma_a$. In practice, both c_0 and c_1 represent very small corrections, with typical values on the order of 0.05 (see Table 3.1).

The results of the fitting for each run are given in Table 3.1. Combining these results with Eqs. (3.48) through (3.50) yields

$$\alpha_{ag}^{\rm II} = -0.316(42)\ {\rm Hz}\cdot({\rm V/cm})^{-2}, \tag{3.52}$$

$P = 13.6(2.6)$ W, and $\omega_{\rm D} = 2\pi \times 6.58(53)$ MHz. The measured values of the circulating power P and the Doppler broadening $\omega_{\rm D}$ are consistent with (and more precise than) direct measurements of these quantities. A comparison of the data to the fit is shown in Fig. 3.7. The quality of both the data and the fit are sufficiently high that the uncertainty of the measured value of $\alpha_{ag}^{\rm II}$ is primarily due to the uncertainties in the vector transition polarizability β_{ag} and the linewidth Γ_a. A summary of the factors that contribute to the uncertainty of the measurement are shown in Table 3.2.

The quantity $\alpha_{ag}^{\rm II} = \alpha_0(^3D_1) - (1/2)\alpha_2(^3D_1) - \alpha_0(^1S_0)$ is a combination of the ac scalar and tensor polarizabilities of the states $^3D_1$ and $^1S_0$. The tensor polarizability of $^3D_1$ is

Table 3.2: Error budget. Shown are the factors contributing to the uncertainty of the measured value of $\alpha_{ag}^{\mathrm{II}}$.

Factor	Uncertainty (%)
Vector transition polarizability (β_{ag})	9
Lifetime of $^3D_1$	8
Light polarization	4
DC electric field	3
Simulation and data fit	3
Total (in quadrature)	**13**

determined unambiguously by comparing the present measurement of $\alpha_{ag}^{\mathrm{II}}$ with the previous measurement of α_{ag}^{I}, which was discussed after Eq. (3.42). We find

$$\alpha_2(^3D_1) = -0.205(53)\ \mathrm{Hz}\cdot(\mathrm{V/cm})^{-2}, \tag{3.53}$$

and

$$\alpha_0(^3D_1) - \alpha_0(^1S_0) = -0.418(36)\ \mathrm{Hz}\cdot(\mathrm{V/cm})^{-2}. \tag{3.54}$$

Finally, the scalar polarizability of $^3D_1$ is isolated by substituting the calculated value $\alpha_0(^1S_0)$, given by Eq. (3.41), into Eq. (3.54):

$$\alpha_0(^3D_1) = 0.151(36)\ \mathrm{Hz}\cdot(\mathrm{V/cm})^{-2}. \tag{3.55}$$

In the presence of linearly polarized light, the polarizability of $^3D_1$ is dominated by the tensor polarizability. However, for light with arbitrary polarization, $\alpha_1(^3D_1)$ also plays a role. Measurement of the vector polarizability is the subject of ongoing experiments.

The tensor-to-scalar ratio of the polarizabilities of the $^3D_1$ state is $-1.36(48)$. This ratio is consistent with the claim that the polarizability of $^3D_1$ is dominated by near-resonant mixing of $^3D_1$ with a high-lying $J = 2$ state; in that case, we would expect the tensor-to-scalar ratio to be -1 (see Appendix B.1). Measurement of the vector polarizability could provide additional information about such a high-lying $J = 2$ state: if it existed, then the scalar-to-vector polarizability ratio would be $(2/3)(1-\omega_{J=2}/\omega)$, where $\omega_{J=2}$ is the energy of the hypothetical $J = 2$ state.

3.4 Summary and Outlook

This work is part of a continuing investigation of polarizabilities in Yb. The ac scalar and tensor polarizabilities of the excited $^3D_1$ state in Yb were measured independently for the first time. Ongoing experiments are focused on measuring the ac vector polarizability, for which there is currently no experimental or theoretical data.

To measure the vector polarizability, the $^1S_0 \rightarrow {}^3D_1$ transition must be excited using circularly polarized light, as can be seen in Eq. (3.47). Such a measurement requires control

over the ellipticity of the light. In the present experimental setup, only two Zeeman sublevels ($M_a = \pm 1$) are excited. The degree of ellipticity can be measured by comparing the relative strengths of the transitions to different sublevels. For purely circularly polarized light, only one sublevel is excited. This condition is ideal for measurement of the vector polarizability.

In this chapter, we presented the next generation of the Lineshape Simulation Method (LSM) for measuring combinations of polarizabilities of the ground and excited states in atoms. The LSM was originally developed specifically for Yb, but we have generalized the method for an arbitrary atomic system with the level structure shown in Fig. 3.7. For example, the LSM could be used to measure the polarizabilities of the $6S$ and $7S$ states in cesium by observing the lineshape of the 539-nm $6S \rightarrow 7S$ transition driven by a standing wave of light [119].

Chapter 4

Novel schemes for measuring APV

In this chapter, we propose two methods for measuring APV using two-photon transitions, the *all-optical scheme (AOS)* and the *degenerate photon scheme (DPS)*. Both techniques can be thought of as extensions of the single-photon Stark interference method. The AOS replaces static electric and magnetic fields with optical ones via the introduction of a second light source. On the other hand, the DPS–which requires only a single light source–is essentially the same as the Stark interference method except that nuclear-spin-independent sources of APV are eliminated by taking advantage of the bosonic nature of photons. This work originally appeared in Refs. [38] and [39].

4.1 APV in $J = 0 \to 0$ two-photon transitions

In addition to well-established Stark-interference techniques, there are various extensions: Light-shift measurements of amplitude interference have been proposed for various systems [57], including atoms [16], single trapped ions [59, 117], two-ion entangled states [86], and chiral molecules [6, 70]. The potential advantages of using electromagnetically induced transparency to measure APV-induced optical rotation in thallium have been investigated [29]. It has also been proposed to employ interference of a parity conserving two-photon transition with a parity violating single-photon transition in cesium [68, 69].

All these methods rely on application of static external electric and magnetic fields to amplify and discriminate APV effects. Misalignments of applied fields introduce systematic uncertainties limiting the precision of APV measurements [111]. In this section, we present a scheme for measuring NSI APV that replaces static fields with optical fields, which are easier to align. The proposed scheme uses a two-photon transition between energy eigenstates of zero electronic angular momentum. Amplification of APV effects is achieved by interference of two transition amplitudes: a parity conserving amplitude describing electric-dipole-magnetic-dipole ($E1$-$M1$) transitions, and a parity violating $E1$-$E1$ amplitude. The APV signal can be discriminated from the large parity conserving background by manip-

ulating properties of the light fields. A further advantage of this scheme is the ability to measure spurious electric and magnetic fields. This method, which we call the *all-optical scheme (AOS)*, is applicable to a variety of atomic systems.

We consider an application of the AOS that takes advantage of the large NSI APV mixing of the $6s6p\ ^1P_1$ and $5d6s\ ^3D_1$ states observed in ytterbium [111]. Precise measurements of this mixing in a chain of isotopes will provide important information about nuclear structure and facilitate a search for physics beyond the Standard Model [23, 48], two major goals of ongoing Stark-interference experiments [111]. Systematic errors due to imperfections of applied fields pose a challenge for APV experiments, and cross-checks of present and future measurements are highly valuable. In the case of cesium, for instance, a cross check was provided by a stimulated-emission experiment [65, 66]. To this end, we propose applying the AOS to the ytterbium two-photon ($\lambda_1 = 399$ nm, $\lambda_2 = 1.28$ μm) $6s^2\ ^1S_0 \rightarrow 6s6p\ ^3P_0$ transition to measure the parity-violating mixing of the intermediate $6s6p\ ^1P_1$ state with the $5d6s\ ^3D_1$ state.

From a formal point of view, the AOS is equivalent to measuring optical rotation induced by APV on an $M1$ transition [15]. However, the AOS provides more field reversals compared to traditional optical rotation experiments, thereby allowing for better discrimination of systematic effects from the APV signal. For the ytterbium system, a scheme for measuring APV-induced optical rotation on the 1.28 μm $6s6p\ ^3P_0 \rightarrow 6s6p\ ^1P_1$ has previously been proposed [79]. The AOS has two advantages over that proposal: the light fields are cw rather than pulsed, bypassing the challenges of achieving a high repetition rate; and, APV effects are measured by observing population of the metastable $6s6p\ ^3P_0$ state, which allows for measurement in a region where detection conditions are easier to optimize.

All-optical scheme

We consider atoms illuminated by two light fields, with polarization vectors $\boldsymbol{\epsilon}_j$, propagation vectors $\mathbf{k}_j$, and frequencies ω_j, where $j = 1, 2$ is the light-field index. We denote the wavenumbers $k_j \equiv |\mathbf{k}_j| = \omega_j/c$, the wavelengths $\lambda_j = 2\pi/k_j$, and the field intensities $\mathcal{I}_j$. The light fields drive two-photon transitions from initial state $|i\rangle$ to final state $|f\rangle$, separated in energy by ω_{fi}. The transition rate on resonance ($\omega_1 + \omega_2 = \omega_{fi}$) is [53]:

$$R = (2\pi)^3 \alpha^2 \mathcal{I}_1 \mathcal{I}_2 |A|^2 \frac{2}{\pi\,\Gamma}, \tag{4.1}$$

where α is the fine-structure constant, A is the transition amplitude, and Γ is the width of the transition. Energy eigenstates are represented as $|i\rangle = |J_i M_i\rangle$, and likewise for $|f\rangle$. Here J_i and $M_i \in \{\pm J_i, \pm(J_i - 1), \ldots\}$ are quantum numbers associated with the electronic angular momentum and its projection along the quantization axis, respectively.

The AOS uses a two-photon transition from an initial state with $J_i = 0$ to an opposite-parity final state with $J_f = 0$. The transition is enhanced by the presence of an intermediate state $|n\rangle$ with $J_n = 1$. The character of the two-photon transition depends on the magnitude of the detuning of the light fields from the one-photon resonances involving the intermediate

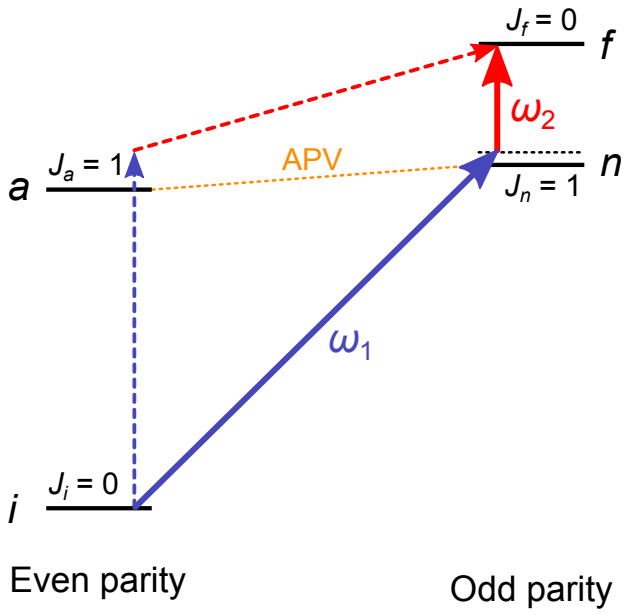

Figure 4.1: Energy levels and transitions relevant to the AOS. The dashed ellipse represents mixing of the states $|n\rangle$ and $|a\rangle$ due to the electroweak interaction. The dotted horizontal line represents the detuning of the light fields from the intermediate state. Thick, solid arrows and thin, dashed arrows illustrate dominant and suppressed excitation paths, respectively.

state [110]. When the detuning is small, the final state is populated by cascade excitation, that is, consecutive single-photon $i \to n$ and $n \to f$ transitions. We work in the opposite regime of large detuning [see condition (4.11) below]. In this regime, the excitation occurs via a pure two-photon transition and the population of the intermediate state is negligible.

The probability amplitude for the $i \to f$ transition has two contributions: one from a parity conserving $E1$-$M1$ transition, and another from a parity violating $E1$-$E1$ transition. The $E1$-$E1$ transition is induced by mixing of the intermediate state[1] $|n\rangle$ with opposite-parity $J = 1$ states via the electroweak interaction. We assume that this mixing is dominated by a single nearby state $|a\rangle$ with $J_a = 1$ (Fig. 4.1). The proximity of $|a\rangle$ to $|n\rangle$ leads to an $M1$-$E1$ excitation path for the $i \to f$ transition that uses the intermediate state $|a\rangle$ rather than $|n\rangle$. We incorporate the amplitude of this path into the expression for the $E1$-$M1$ amplitude below.

In the absence of stray fields, the amplitude for a two-photon $J_i = 0 \to J_f = 0$ transition

[1] Alternatively, the $E1$-$E1$ transition could be induced by mixing of the final state $|f\rangle$ with opposite-parity $J = 0$ states. Such a scheme is equivalent to the AOS, and shares the key features of the AOS presented in this work.

is (Appendix A):

$$A = A_{E1-M1} + A_{\rm w}, \tag{4.2}$$

where

$$A_{E1-M1} = [\mathcal{M}(\omega_1)\hat{\mathbf{k}}_2 - \mathcal{M}(\omega_2)\hat{\mathbf{k}}_1] \cdot (\boldsymbol{\epsilon}_1 \times \boldsymbol{\epsilon}_2) \tag{4.3}$$

and

$$A_{\rm w} = i[\zeta(\omega_1) + \zeta(\omega_2)](\boldsymbol{\epsilon}_1 \cdot \boldsymbol{\epsilon}_2) \tag{4.4}$$

are the amplitudes corresponding to the $E1$-$M1$ and electroweak interaction induced $E1$-$E1$ transitions[2]. The quantities $\mathcal{M}(\omega_j)$ and $\zeta(\omega_j)$ are

$$\mathcal{M}(\omega_j) = \frac{1}{3}\left(\frac{\mu_{fn}\, d_{ni}}{\omega_{ni} - \omega_j} + \frac{d_{fa}\, \mu_{ai}}{\omega_{ai} - \omega_j}\right) \tag{4.5}$$

and

$$\zeta(\omega_j) = \frac{1}{3}\frac{d_{fa}\, \Omega_{an}\, d_{ni}}{\omega_{na}}\left(\frac{1}{\omega_{ni} - \omega_j} - \frac{1}{\omega_{ai} - \omega_j}\right), \tag{4.6}$$

where μ_{fn} and d_{ni} are the reduced matrix elements of the magnetic- and electric-dipole moments, respectively. Here ω_{na} is the energy difference of states $|a\rangle$ and $|n\rangle$, and Ω_{an} is the magnitude of the reduced matrix element of the NSI APV Hamiltonian $H_{\rm NSD}$ [see Eq. (D.12) in the Appendix].

The two terms in each of Eqs. (4.5, 4.6) correspond to the two different excitation paths for the transition. If states $|n\rangle$ and $|a\rangle$ were perfectly degenerate ($\omega_{na} = 0$), the induced $E1$-$E1$ paths would interfere destructively and the parity violating amplitude vanishes. We limit our discussion to atomic systems for which ω_{na} is sufficiently large that one path is dominant. We assume that $\Delta = \omega_1 - \omega_{ni}$ is much smaller than all other detunings from the intermediate states $|n\rangle$ and $|a\rangle$. In this case, only

$$\mathcal{M}(\omega_1) \approx \mathcal{M} \equiv \frac{1}{3}\frac{\mu_{fn}\, d_{ni}}{\Delta} \tag{4.7}$$

and

$$\zeta(\omega_1) \approx \zeta \equiv \frac{1}{3}\frac{d_{fa}\, \Omega_{an}\, d_{ni}}{\omega_{na}\Delta} \tag{4.8}$$

contribute significantly to Eqs. (4.3, 4.30). Because $\mathcal{M}$ and ζ have the same complex phase [78], the relative phase between A_{E1-M1} and $A_{\rm w}$ is determined by the field geometry. Hereafter, we assume that $\mathcal{M}$ and ζ are real parameters since their common phase is irrelevant.

The goal of the AOS is to observe interference of amplitudes $A_{\rm w}$ and A_{E1-M1} in the rate R. As Eqs. (4.1-4.30) show, R consists of a large parity conserving term proportional to $\mathcal{M}^2$,

[2] The $E1$-$M1$ amplitude is a product of the matrix elements of the operators describing $E1$ and $M1$ single-photon transitions. Because the $E1$ ($M1$) operator is odd (even) under spatial inversion, the $E1$-$M1$ amplitude is a pseudoscalar. A similar argument shows that the $E1$-$E1$ amplitude is a normal scalar.

a small parity violating term (the interference term) proportional to $\mathcal{M}\zeta$, and a negligibly small term on the order of ζ^2. The interference term is proportional to a pseudoscalar quantity that depends only on the field geometry, the *rotational invariant*:

$$\mathrm{Im}\{(\boldsymbol{\epsilon}_1 \cdot \boldsymbol{\epsilon}_2)^*[(\boldsymbol{\epsilon}_1 \times \boldsymbol{\epsilon}_2) \cdot \mathbf{k}_2]\}, \tag{4.9}$$

which changes sign upon spatial inversion and is invariant under time reversal[3]. The time reversal invariance of expression (4.9) can be understood in the following way. In addition to changing the sign of the photon momentum, time reversal requires complex conjugation [101]. Therefore there is no overall change in sign of expression (4.9) under time reversal.

The dependence of APV interference on the geometry of the light fields is inferred from the form of the rotational invariant. The rotational invariant, and hence the interference term, vanishes for plane polarized light beams. One way to achieve a nonzero rotational invariant is to choose circular polarization for the second beam: $\boldsymbol{\epsilon}_2 = \boldsymbol{\sigma}_\pm$, where we have assumed $\mathbf{k}_2$ lies along the z axis. For arbitrary polarization $\boldsymbol{\epsilon}_1 = a_+\boldsymbol{\sigma}_+ + a_-\boldsymbol{\sigma}_-$ of the first beam, conservation of angular momentum requires that only the polarization component $a_\mp$ contributes to the excitation process. Thus the rotational invariant (4.9) reduces to $\pm|a_\mp|^2 k_z$, where $k_z = +1$ ($k_z = -1$) when $\mathbf{k}_2$ is aligned (anti-aligned) with the z-axis.

For two collinear circularly polarized beams of light oriented along the z-axis, the transition rate is

$$R \propto |A|^2 = \mathcal{M}^2 \pm 2k_z\mathcal{M}\zeta, \tag{4.10}$$

where we have neglected the term proportional to ζ^2. The positive (negative) sign in Eq. (4.10) is taken when beam 2 has $\boldsymbol{\sigma}_+$ ($\boldsymbol{\sigma}_-$) polarization. The interference term is discriminated from the total transition rate either by reversing the direction of the propagation vector $\mathbf{k}_2$, or by reversing the sense of rotation of the circularly polarized light fields. The asymmetry $2\zeta/\mathcal{M} = 2(d_{fa}/\mu_{fn})(\Omega_{an}/\omega_{na})$ is obtained by dividing the difference of rates upon a reversal by their sum.

We propose to measure the transition rate by probing the population of the final state $|f\rangle$ while the following conditions hold: (i) the transition is purely two-photon, and (ii) the transition is not saturated. A pure two-photon transition is achieved when [53, 110]

$$|\Delta| \gg \Omega_0, \tag{4.11}$$

where

$$\Omega_0 = \sqrt{\frac{8\pi\alpha}{3}\left(d_{ni}^2\,\mathcal{I}_1 + \mu_{fn}^2\,\mathcal{I}_2\right)} \tag{4.12}$$

is the interaction energy. When condition (4.11) is satisfied, the system reduces to a two-level system consisting of the initial and final states coupled by a single effective driving

[3] The rotational invariant presented in Eq. (4.9) is not symmetric under photon exchange because we have neglected the terms proportional to $\mathcal{M}(\omega_2)$ and $\zeta(\omega_2)$ in Eqs. (4.3, 4.30). When these terms are included, R has two interference terms whose sum is exchange symmetric. In the case of degenerate photons ($\omega_1 = \omega_2$), the sum of the interference terms is proportional to the exchange symmetric rotational invariant $\mathrm{Im}\{(\boldsymbol{\epsilon}_1 \cdot \boldsymbol{\epsilon}_2)^*[(\boldsymbol{\epsilon}_1 \times \boldsymbol{\epsilon}_2) \cdot (\hat{\mathbf{k}}_1 - \hat{\mathbf{k}}_2)]\}$.

field. Saturation effects can be ignored when the pumping rate R is much smaller than the relaxation rate Γ' of the final state, that is, when

$$\mathcal{I}_1\mathcal{I}_2 \ll \left[\frac{3}{\pi\alpha}\frac{\Delta}{d_{ni}\,\mu_{fn}}\right]^2 \Gamma\Gamma'. \tag{4.13}$$

In this regime, the population of the final state is proportional to the rate given by Eq. (4.1).

The shot-noise limited sensitivity of the AOS is estimated as follows. The probe signal is proportional to the number of excited atoms. The number of excited atoms associated with the parity violating part of the transition rate is

$$N = [(4\pi\alpha)^2\mathcal{I}_1\mathcal{I}_2(2\mathcal{M}\zeta)/\Gamma]N_i t, \tag{4.14}$$

where t is the effective integration time of the measurement and N_i is the total number of atoms initially in state $|i\rangle$. The measurement noise is given by $\delta N = \sqrt{N'}$, where

$$N' = [(4\pi\alpha)^2\mathcal{I}_1\mathcal{I}_2\mathcal{M}^2/\Gamma]N_i t \tag{4.15}$$

is the number of excited atoms associated with the parity conserving part of the transition rate. The signal-to-noise ratio (SNR) of the probe signal is $N/\delta N$, or

$$\mathrm{SNR} = \frac{8\,\pi\alpha}{3}\,\frac{d_{fa}\,\Omega_{an}\,d_{ni}}{\omega_{na}|\Delta|}\sqrt{\frac{\mathcal{I}_1\,\mathcal{I}_2\,N_i\,t}{\Gamma}}. \tag{4.16}$$

As expected, the SNR increases for large Ω_{an} and high light intensities. Although purely statistical shot-noise dominated SNR does depend on μ_{fn}, this amplitude is still an important parameter in practice due to conditions (4.11, 4.13). Large μ_{fn} leads to small APV asymmetry which requires better control over experimental parameters (see Sec. 4.1). In the opposite case of small μ_{fn}, an observable signal requires high light intensities which may pose a technical challenge.

Although we have focused on a ladder-type three-level atomic system (Fig. 4.1), the discussion presented here holds for lambda-type systems (Fig. 4.2) as well. However, the following modifications must be made: In a lambda-type system, the polarization of the absorbed photon $\boldsymbol{\epsilon}_2$ is replaced by the polarization of the photon emitted by stimulated emission. Consequently, conservation of energy requires that the two-photon resonance condition above Eq. (4.1) becomes $\omega_1 - \omega_2 = \omega_{fi}$, and conservation of angular momentum requires that both circularly polarized beams have the same sense of rotation. Then the positive (negative) sign is taken in Eq. (4.10) when $\boldsymbol{\epsilon}_1 = \boldsymbol{\epsilon}_2 = \boldsymbol{\sigma}_{-(+)}$.

Spurious sources of asymmetry

Systematic effects may also contribute to the asymmetry and mask the APV signal. In this section, we discuss three potential sources of such spurious asymmetry: imperfections of applied optical fields; Stark interference due to stray electric fields; and, shifts of the intermediate state energy induced by external fields.

Optical field imperfections

To understand the effects of imperfections in the optical fields, we relax the assumptions of collinear light beams and perfectly circular polarization. We choose the z-axis to lie along $\mathbf{k}_2$. In this case, misalignment of the nominally collinear beams is characterized by the polar ($\theta \ll 1$) and azimuthal (ϕ) angles of $\mathbf{k}_1$.

The polarization of arbitrarily polarized light is parameterized in terms of the polarization angle ϑ_j and the ellipticity φ_j in the following way:

$$\boldsymbol{\epsilon}_j = (\cos\vartheta_j \cos\varphi_j - i \sin\vartheta_j \sin\varphi_j)\hat{\mathbf{x}} + (\sin\vartheta_j \cos\varphi_j + i \cos\vartheta_j \sin\varphi_j)\hat{\mathbf{y}}, \tag{4.17}$$

where $\hat{\mathbf{x}}$ and $\hat{\mathbf{y}}$ are Cartesian unit vectors in the x and y directions. Linearly, circularly, and elliptically polarized light are described by $\varphi_j = 0$, $|\varphi_j| = \pi/4$ and $0 < |\varphi_j| < \pi/4$, respectively. The sense of rotation is determined by sign of the ellipticity: $\boldsymbol{\epsilon}_j = \boldsymbol{\sigma}_\pm$ when $\varphi_j = \pm\pi/4$. Deviations from circular polarization are characterized by the parameters $\eta_j \equiv \pi/4 - |\varphi_j| \ll 1$.

Field imperfections lead to additional parity conserving terms in R:

$$R \to R - \mathcal{M}^2[\theta^2/2 + \eta_1^2 + \eta_2^2 + 2\eta_1\eta_2 \cos(2\vartheta - 2\phi)], \tag{4.18}$$

where $\vartheta = \vartheta_2 - \vartheta_1$ is the relative polarization angle of the light fields. We treat the case of maximal correction, that is, $\vartheta = \phi$. Then the corrections to R are on the order of $\mathcal{M}^2[\theta^2/2 + (\eta_1 + \eta_2)^2]$. Although these corrections to R do not mimic APV, they nevertheless contribute to the asymmetry if they change upon reversal. To simplify our analysis, we assume that changes in θ and η_j between reversals are on the order of θ and η_j for any particular reversal. We further assume that η_1 and η_2 are similar in magnitude: $\eta_1 \simeq \eta_2 \equiv \eta$. Then spurious ellipticity and beam misalignment give rise to a spurious asymmetry on the order of $\theta^2 + 2\eta^2$, and may mask the APV signal if they are large. Asymmetry due to field imperfections is negligible compared to APV asymmetry when

$$\theta^2 \ll 2\zeta/\mathcal{M} \quad \text{and} \quad \eta^2 \ll \zeta/\mathcal{M}. \tag{4.19}$$

Stark interference

The derivation of Eq. (4.10) assumes the absence of external fields. Here we relax this assumption and discuss the uncertainty in the AOS that arises due to spurious electric fields. In the presence of a static electric field $\mathbf{E}$, Stark mixing of $|n\rangle$ and $|a\rangle$ induces an $E1$-$E1$ transition between the initial and final states. The Stark-induced transition amplitude is (Appendix A):

$$A_{\rm s} = i\xi[\mathbf{E} \cdot (\boldsymbol{\epsilon}_1 \times \boldsymbol{\epsilon}_2)], \tag{4.20}$$

where

$$\xi = \frac{1}{3\sqrt{6}} \frac{d_{fa}\, d_{an}\, d_{ni}}{\omega_{na}\Delta}. \tag{4.21}$$

After including the effects of stray fields and misalignments, the transition rate (4.10) becomes

$$R \propto \mathcal{M}^2 + \xi^2 E_z E_1 \pm k_z\big(\mathcal{M}\xi E_\perp + 2\mathcal{M}\zeta\big), \tag{4.22}$$

where E_z is the z component of the electric field, $E_1 = \mathbf{E}\cdot\hat{\mathbf{k}}_1 \approx E_z$, $E_\perp = |\mathbf{E}\cdot(\hat{\mathbf{k}}_1\times\hat{\mathbf{k}}_2)| \lesssim \theta|\mathbf{E}|$, and only terms linear in θ and η_j are presented. The terms in the parentheses represent the combined effects of APV and Stark interference. These interference terms exhibit the same behavior under reversals of the light fields. This means that there is a contribution to the asymmetry on the order of $\theta\xi E/\mathcal{M}$, where E is the magnitude of $|\mathbf{E}|$. APV asymmetry dominates over asymmetry due to Stark interference when

$$E \ll 2\zeta/(\theta\xi). \tag{4.23}$$

Energy shifts of the intermediate state

The transition rate must be further modified to account for light shifts and effects of stray magnetic fields. We consider energy shifts of the form $M_n^2\delta_2 + M_n\delta_1$, where M_n is the magnetic quantum number of $|n\rangle$.

The parameter δ_2 is due to tensor shifts caused by the light fields or dc electric fields. We neglect quadratic Zeeman shifts that arise in the presence of transverse magnetic fields. In general, many levels may contribute to light shifts of the intermediate state. We approximate light shifts by their contributions from the initial and final states. Then the light shifts are approximately equal to $\Omega_0^2/(4\Delta)$, where Ω_0 is given by Eq. (4.12). When the dc polarizability of the intermediate state is dominated by Stark mixing of $|n\rangle$ and $|a\rangle$, dc Stark shifts of that state are on the order of $d_{an}^2E^2/(2\omega_{na})$. Then

$$\delta_2 \approx \Omega_0^2/(4\Delta) + d_{an}^2E^2/(2\omega_{na}). \tag{4.24}$$

The parameter δ_1 is due to vector light shifts and the dc Zeeman effect. Vector light shifts change sign upon reversal of circular polarization ($\boldsymbol{\sigma}_\pm \to \boldsymbol{\sigma}_\mp$). In this case,

$$\delta_1 \approx \pm\Omega_0^2/(4\Delta) + g\mu_0 B_z, \tag{4.25}$$

where g is the Landé factor of the intermediate state, μ_0 is the Bohr magneton, B_z is the z-component of the stray magnetic field, and $g\mu_0 B_z$ is the Zeeman shift.

The corrected $E1$-$M1$ and Stark-induced $E1$-$E1$ transition amplitudes are obtained by expanding the energy denominators in Eqs. (C.2-C.6) in Appendix A to first order in $\delta_{1,2}$. Corrections to the electroweak interaction induced amplitude (4.6) are neglected here. The transition rate is

$$R \propto \mathcal{M}^2\big[1 + 2(\delta_2 \pm \delta_1)/\Delta\big] + \xi^2 E_1 E_z - 2\xi^2 E_z^2(\delta_2 \pm \delta_1)/\Delta \pm k_z\big(\mathcal{M}\xi E_\perp + 2\mathcal{M}\zeta\big), \tag{4.26}$$

where summation over the magnetic sublevels of $|n\rangle$ has been taken into account. Only the Stark interference term $\mathcal{M}\xi E_\perp$ has the same signature as APV. The Stark and Zeeman shift

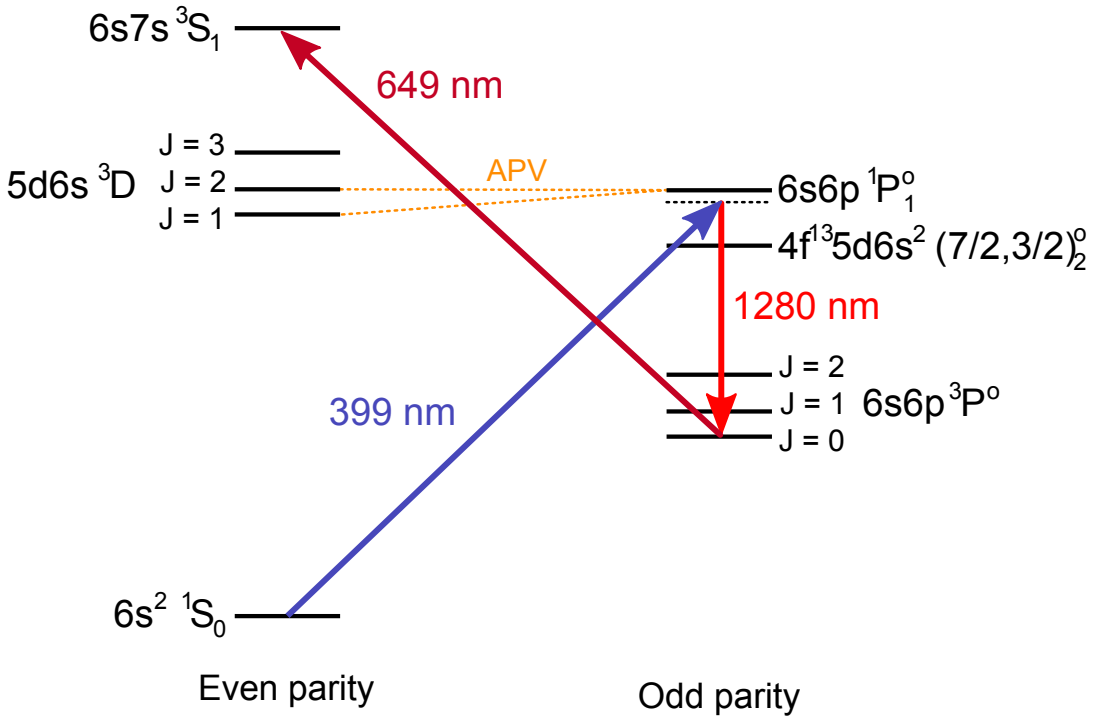

Figure 4.2: Application of AOS to ytterbium.

corrections can be discriminated from the other terms in Eq. (4.26) by changing the sign of Δ, and can be discriminated from each other by reversing the sense of rotation of the circularly polarized light fields. Thus stray electric and magnetic fields can be measured by alternating the sign of the detuning of the light fields from the intermediate state.

Applications of the AOS

We now turn our attention to the two-photon $6s^2\ ^1S_0 \to 6s6p\ ^3P_0$ transition in ytterbium. This transition can be driven by two light fields of wavelengths $\lambda_1 = 399$ nm and $\lambda_2 = 1.28\ \mu$m, which are nearly resonant with transitions involving the intermediate $6s6p\ ^1P_1$ state (Fig. 4.2). The parity violating $E1$-$E1$ transition is induced by the mixing of the $6s6p\ ^1P_1$ and $5d6s\ ^3D_1$ states due to the electroweak interaction. The parameter describing mixing of $6s6p\ ^1P_1$ and $5d6s\ ^3D_1$ was measured to be $\Omega_{an}/\omega_{na} = 6 \times 10^{-10}$ [111]. Other essential atomic parameters are given in Table 4.1. The asymmetry in ytterbium is $2\zeta/\mathcal{M} \approx 6 \times 10^{-6}$, more than an order of magnitude larger than asymmetries measured in optical rotation experiments in bismuth, lead, and thallium [62].

As an example, we consider an experiment using an atomic beam similar to that of Ref. [111]: characteristic thermal speed 3×10^4 cm/s; density 2×10^9 cm^{-3}; and, radius 1 cm.

Table 4.1: Atomic data for application of AOS to ytterbium. Here a_0 and μ_0 are the Bohr radius and magneton.

	Transition $(1 \to 2)$	$d_{21}/(ea_0)$	μ_{21}/μ_0
$E1$	$6s^2\ {}^1S_0 \to 6s6p\ {}^1P_1$	4.1^a	
	$6s6p\ {}^3P_0 \to 5d6s\ {}^3D_1$	2.6^b	
	$5d6s\ {}^3D_1 \to 6s6p\ {}^1P_1$	0.27^b	
$M1$	$6s^2\ {}^1S_0 \to 5d6s\ {}^3D_1$		$1.33^c \times 10^{-4}$
	$6s6p\ {}^3P_0 \to 6s6p\ {}^1P_1$		0.13^d

[a]Ref. [11], [b]Ref. [95], [c]Ref. [108], [d]Ref. [79]

The atomic beam intersects two overlapping, collinear laser beams where atoms interact with the 399 nm and 1.28 μm light and undergo transitions from $6s^2\ {}^1S_0$ to $6s6p\ {}^3P_0$. High light powers–which are necessary to achieve a large SNR–can be realized using a unidirectional ring cavity. The transition rate can be measured by probing the population of the metastable $6s6p\ {}^3P_0$ state using the detection method described in Ref. [111].

To estimate the SNR, we choose light parameters that satisfy conditions (4.11, 4.13). The laser beams have a Gaussian profile with a characteristic radius of 2 mm, and the frequencies are detuned from the intermediate state by $\Delta = 2\pi \times 800$ MHz, about 30 times larger than the width of the intermediate state. In the interaction region, the metastable state acquires a radiative decay rate on the order of $\Gamma' = [\Omega_0^2/(4\Delta^2)]\tau^{-1} = 2\pi \times 30$ kHz, where $\tau = 5.68$ ns is the lifetime of $6s6p\ {}^1P_1$ [11]. The width of the $6s^2\ {}^1S_0 \to 6s6p\ {}^3P_0$ transition is dominated by the transit-broadened linewidth[4] $\Gamma = 2\pi \times 90$ kHz. For light powers of 10 W at 1.28-μm and 10 mW at 399-nm, Eq. (4.16) gives SNR $\approx 2\sqrt{t(\mathrm{s})}$. Based on these estimates, a one-hour measurement may achieve better than 1% statistical uncertainty in determination of parity violation.

Spurious asymmetry due to field imperfections and stray electric fields can be controlled by aligning the laser beams over a large distance. In order to limit asymmetry due to beam misalignment to less than 1% of the APV asymmetry, the angle between the nominally collinear laser beams must be controlled to better than one-tenth of a beam radius of transverse displacement over a distance of one meter, which corresponds to a beam misalignment of 0.01°. Similarly, the deviation from circular polarization must also be smaller than about 0.01°. In this case, the systematic uncertainty due to Stark interference effects is below 1% for electric fields smaller than 8 V/cm. In Ref. [111], stray electric fields were measured to be on the order of 1 V/cm. In that experiment, stray electric fields are partially attributed

[4] The transit-broadened width of a one-photon transition is $\Gamma_0 \approx 2.4v/r$ [36], where v is the atomic velocity and r is the $1/e$ radius of the optical electric field profile. The matrix element for a two-photon transition is proportional to the product of the two optical electric fields, and hence to the product of their Gaussian profiles [53]. Therefore, the transit-broadened width is $\Gamma = \sqrt{2}\Gamma_0$ when the beam profiles are identical.

to charge buildup on surfaces of electrodes and coils that are used to generate external static electric and magnetic fields. For the AOS, the absence of such surfaces will likely result in even smaller stray fields.

It is important to consider other mechanisms for population of the metastable $6s6p\,^3P_0$ state, causing background and noise. The metastable state may be populated by multiphoton processes involving highly excited states, or by molecular processes in the presence of dimers or other molecular impurities in the atomic beam. These detrimental effects will contribute to a background that depends on Δ, compromising the search for stray fields [15]. We note that no evidence of molecular impurities has been seen in the ytterbium APV experiments up to date.

To better understand the feasibility of the proposed experiment, we compare the predicted SNR of the two-photon AOS to the observed SNR of the one-photon Stark-interference experiment [111]. This comparison is especially relevant since both techniques employ the same method for probing the population of the metastable $6s6p\,^3P_0$ state in ytterbium. The shot-noise limited SNR in Chapter 2 was demonstrated to be $3\sqrt{t(\mathrm{s})}$. However, the Stark-interference experiment is not currently shot-noise limited; the measurement uncertainty is determined by systematic effects due to imperfections of applied fields. Because the AOS has similar projected statistical sensitivity and possibly better control of systematics compared to the Stark-interference experiment, the AOS is an attractive candidate for future APV measurements in ytterbium.

Another candidate for the AOS is the ladder-type $4f^6 6s^2\,{}^7F_0 \rightarrow 4f^6 6s6p\,{}^7F_0$ transition ($\lambda_1 = 639$ nm, $\lambda_2 = 1.56\ \mu$m) in samarium. The $E1$-$E1$ transition is induced by mixing of the opposite-parity states $4f^6 5d6s\,{}^7G_1$ and $4f^6 6s6p\,{}^7G_1$ due to the electroweak interaction. The APV effect in samarium is expected to be of the same order of magnitude as that observed in ytterbium [99]. A version of the AOS that uses photons of the same frequency has been previously suggested in a proposal for a search for APV using the 1 μm $1s2p\,^3P_0 \rightarrow 1s2s\,^1S_0$ transition in uranium ions [103]. However, the uranium-ion experiment is not currently feasible because the required laser intensity is on the order of 10^{21} W/cm^2.

4.2 APV in $J = 0 \rightarrow 1$ two-photon transitions

Sub-1% measurements of nuclear spin-independent (NSI) atomic parity violation (APV) [120] have led to precise evaluation of the nuclear weak charge [94], yielding excellent agreement with the Standard Model at low energies. On the other hand, nuclear anapole moments, parity violating magnetic moments induced by weak interactions within the nucleus, have been extracted from nuclear spin dependent (NSD) APV measurements in Cs [56] and Tl [82]. In these experiments, NSD APV was observed as a small correction to NSI effects [55]. In this section, we propose a technique that allows for measurement of NSD APV without NSI background in atoms with nonzero nuclear spin.

The proposed method uses two-photon transitions from an initial state of total electronic angular momentum $J_i = 0$ to an opposite-parity $J_f = 1$ final state (or *vice versa*). The

APV signal is due to interference of parity-conserving electric-dipole-electric-quadrupole ($E1$-$E2$) and electric-dipole-magnetic-dipole ($E1$-$M1$) transitions with parity-violating $E1$-$E1$ transitions induced by the electroweak interaction. This scheme is different from other multi-photon APV schemes [29, 38, 66, 68] in that the transitions are driven by collinear photons of the same frequency, and hence are subject to a Bose-Einstein statistics (BES) selection rule that forbids $E1$-$E1$ $J = 0 \to 1$ transitions [14, 34, 52]. However, such transitions may be induced by perturbations that cause the final state to mix with opposite-parity $J \neq 1$ states, such as the NSD electroweak interaction and, in the presence of an external static electric field, the Stark effect. Because the NSI electroweak interaction only leads to mixing of the final state with other $J = 1$ states, it cannot induce $J = 0 \to 1$ transitions. Thus NSI-background-free measurements of NSD APV can be achieved by exploiting two-photon BES selection rules.

Consider atoms illuminated by light in the presence of a static magnetic field $\mathbf{B}$. The optical field is characterized by polarization $\boldsymbol{\epsilon}$, propagation vector $\mathbf{k}$, frequency ω, and intensity $\mathcal{I}$. Because circularly polarized light cannot excite a $J = 0 \to 1$ two-photon transition due to conservation of angular momentum, we assume that the light is linearly polarized. We choose the frequency to be half the energy interval ω_{fi} between the ground state $|i\rangle$ and an excited state $|f\rangle$ of opposite nominal parity. The transition rate is [53]:

$$R = (2\pi)^3 \alpha^2 \mathcal{I}^2 |A|^2 \frac{2}{\pi\Gamma}, \tag{4.27}$$

where α is the fine structure constant, and A and Γ are the amplitude and width of the transition. Energy eigenstates are represented as $|i\rangle = |J_i I F_i M_i\rangle$, and likewise for $|f\rangle$. Here J_i, I, and F_i are quantum numbers associated with the electronic, nuclear, and total angular momentum, respectively, and $M_i \in \{\pm F_i, \pm(F_i - 1), \ldots\}$ is the projection of F_i along the quantization axis (z-axis), which we choose along $\mathbf{B}$.

The transition is enhanced by the presence of an intermediate state $|n\rangle$ of total electronic angular momentum $J_n = 1$ whose energy lies about halfway between the energies of the initial and final states (Fig. 4.3). For typical situations, the energy defect $\Delta = \omega_{ni} - \omega_{fi}/2$ is large compared to the Rabi frequency Ω_{R} associated with the one-photon resonance involving the intermediate state. We assume that the scattering rate from $|n\rangle$ to $|i\rangle$ is small compared to the natural width Γ_f of $|f\rangle$: $(\Omega_{\mathrm{R}}/\Delta)^2 \Gamma_n \ll \Gamma_f$. In this case, the system reduces to a two-level system consisting of initial and final states coupled by an effective optical field.

The parity-violating $E1$-$E1$ transition is induced by mixing of the final state with opposite-parity states via the electroweak interaction. In general, $|f\rangle$ may mix with states of electronic angular momentum $J = 0, 1$, or 2 according to the selection rules for NSD APV mixing [78]. Mixing of the final state with $J = 1$ states results in a perturbed final state with electronic angular momentum 1 that cannot be excited via degenerate two-photon transitions. We assume mixing is dominated by a single state $|a\rangle$ of total angular momentum J_a, and consider the cases $J_a = 0$ and $J_a = 2$ separately.

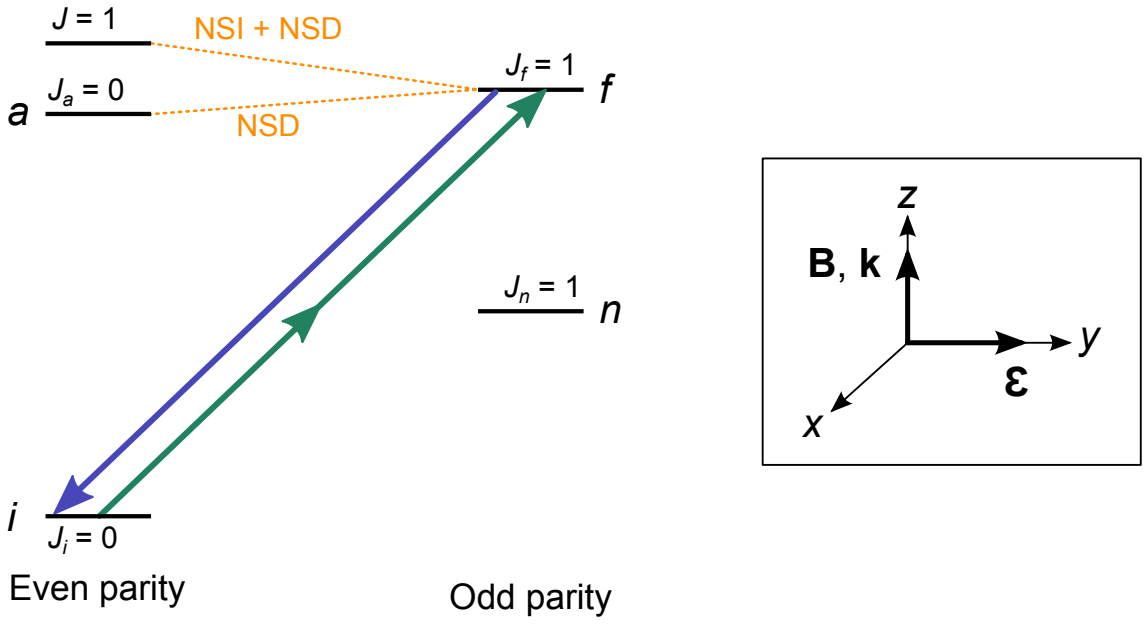

Figure 4.3: Energy level diagram. Dotted lines indicate APV mixing of opposite-parity states, and upward- and downward-pointing arrows represent two-photon absorption and one-photon fluorescence, respectively. Field geometry. The propagation vector $\mathbf{k}$ may alternatively be anti-aligned with the magnetic field $\mathbf{B}$.

NSD APV mixing of $J = 1$ and $J = 0$ states

When $|f\rangle$ mixes with a nearby $J_a = 0$ state, only transitions for which $F_f = I$ may be induced by the electroweak interaction. Transitions to hyperfine levels $F_f = I \pm 1$ that arise due to parity-conserving processes can be used as APV-free references, important for discriminating APV from systematic effects. The amplitude for a degenerate two-photon $J = 0 \to 1$ transition is (Appendix D):

$$A = A_{\rm pc} + A_{\rm w}, \tag{4.28}$$

where

$$A_{\rm pc} = i\mathcal{Q}k_{-q}(\boldsymbol{\epsilon}\cdot\boldsymbol{\epsilon})(-1)^q\langle F_iM_i;1q|F_fM_f\rangle, \tag{4.29}$$

and

$$A_{\rm w} = i\zeta_0(\boldsymbol{\epsilon}\cdot\boldsymbol{\epsilon})\delta_{F_fF_i}\delta_{M_fM_i}, \tag{4.30}$$

are the amplitudes of the parity-conserving and electroweak-interaction-induced parity-violating transitions, respectively. Here $q = M_f - M_i$ is a spherical index, k_q is the qth spherical component of $\hat{\mathbf{k}}$, $\langle F_iM_i;1q|F_fM_f\rangle$ is a Clebsch-Gordan coefficient, and $\delta_{F_fF_i}$ is the Kronecker

delta. The quantities $\mathcal{Q}$ and ζ_0 are

$$\mathcal{Q} = \frac{Q_{fn} d_{ni}}{2\sqrt{15}\Delta} + \frac{\mu_{fn} d_{ni}}{3\sqrt{2}\Delta}, \tag{4.31}$$

and

$$\zeta_0 = \frac{\Omega_{fa} d_{an} d_{ni}}{3\omega_{fa}\Delta}, \tag{4.32}$$

where the reduced matrix elements $Q_{fn} = (J_f||\mathbb{Q}||J_n)$, $\mu_{fn} = (J_f||\mu||J_n)$, and $d_{ni} = (J_n||d||J_i)$ of the electric quadrupole, magnetic dipole, and electric dipole moments, respectively, are independent of F_f and I. Here $\omega_{fa} = \omega_f - \omega_a$ is the energy difference of states $|f\rangle$ and $|a\rangle$, and Ω_{fa} is related to the matrix element of the NSD APV Hamiltonian $H_{\rm NSD}$ by $\langle f|H_{\rm NSD}|a\rangle = i\Omega_{fa}$. The parameter Ω_{fa} must be a purely real quantity to preserve time reversal invariance [78]. Note that $\boldsymbol{\epsilon}\cdot\boldsymbol{\epsilon} = 1$ for linear polarization, whereas $\boldsymbol{\epsilon}\cdot\boldsymbol{\epsilon} = 0$ and hence $A = 0$ for circular polarization, consistent with conservation of angular momentum. Hereafter, we assume $\boldsymbol{\epsilon}\cdot\boldsymbol{\epsilon} = 1$.

The goal of the DPS is to observe interference of parity- violating and conserving amplitudes in the rate R. When $M_f = M_i$, R consists of a large parity conserving term proportional to $\mathcal{Q}^2$, a small parity violating term (the interference term) proportional to $\mathcal{Q}\zeta_0$, and a negligibly small term on the order of ζ_0^2. The interference term is proportional to a pseudoscalar quantity that depends only on the field geometry, the *rotational invariant*:

$$\mathbf{k}\cdot\mathbf{B}. \tag{4.33}$$

The form of the rotational invariant follows from the fact that only $k_0 \propto \mathbf{k}\cdot\mathbf{B}$ contributes to the amplitude in Eq. (4.29) when $M_f = M_i$. Thus the interference term vanishes if $\mathbf{B}$ and $\mathbf{k}$ are orthogonal. One way to achieve a nonzero rotational invariant is to orient $\mathbf{k}$ along $\mathbf{B}$ (Fig. 4.3).

We calculate the transition rate when $\mathbf{B}$ is sufficiently strong to resolve magnetic sublevels of the final state, but not those of the initial state. This regime is realistic since Zeeman splitting of the initial and final states are proportional to the nuclear and Bohr magnetons, respectively. In this case, the total rate is the sum of rates from all magnetic sublevels of the initial state:

$$R \to \sum_{M_i} R(M_i). \tag{4.34}$$

When the fields are aligned as in Fig. (4.3), the transition rate is

$$R_\pm \propto \frac{\mathcal{Q}^2 M_f^2}{I(I+1)} \pm \frac{2\zeta_0 \mathcal{Q} M_f}{\sqrt{I(I+1)}}, \tag{4.35}$$

where the positive (negative) sign is taken when $\mathbf{k}$ and $\mathbf{B}$ are aligned (anti-aligned), and we have omitted the term proportional to ζ_0^2.

Reversals of applied fields are a powerful tool for discriminating APV from systematic effects. The interference term in (4.35) changes sign when the relative alignment of $\mathbf{k}$ and $\mathbf{B}$ is reversed, or when $M_f \to -M_f$. The *asymmetry* is obtained by dividing the difference of rates upon a reversal by their sum:

$$\frac{R_+ - R_-}{R_+ + R_-} = \frac{2\sqrt{I(I+1)}}{M_f}\frac{\zeta_0}{\mathcal{Q}}, \tag{4.36}$$

which is maximal when M_f is small but nonzero. Reversals are sufficient to distinguish APV from many systematic uncertainties. Nevertheless, there still exist systematic effects that give rise to *spurious asymmetries*, which may mask APV.

We consider two potential sources of spurious asymmetry: misalignment of applied fields, and stray electric and magnetic fields. A stray electric field $\mathbf{E}$ may induce $E1$-$E1$ transitions via the Stark effect [18, 19]. The amplitude of Stark-induced $J = 0 \to 1$ transitions is (Appendix D):

$$A_{\rm s} = \xi_0 E_{-q}(-1)^q \langle F_i M_i; 1q | F_f M_f \rangle, \tag{4.37}$$

where

$$\xi_0 = \frac{d_{fa} d_{an} d_{ni}}{3\sqrt{3}\omega_{af}\Delta}. \tag{4.38}$$

When $\mathbf{k}$ and $\mathbf{B}$ are misaligned ($\mathbf{k}\times\mathbf{B} \neq \mathbf{0}$), Stark-induced transitions may interfere with the allowed transitions yielding a spurious asymmetry characterized by the following rotational invariant:

$$(\mathbf{E}\times\mathbf{k})\cdot\mathbf{B} \equiv (\mathbf{k}\times\mathbf{B})\cdot\mathbf{E}. \tag{4.39}$$

The resulting Stark-induced asymmetry is

$$\frac{1}{M_f}\frac{\theta\xi_0 E}{\mathcal{Q}}, \tag{4.40}$$

where $\theta = |\hat{\mathbf{k}}\times\hat{\mathbf{B}}|$ is the angle between the nominally collinear vectors $\mathbf{k}$ and $\mathbf{B}$, and E is defined by $\theta E \equiv (\mathbf{k}\times\mathbf{B})\cdot\mathbf{E}$. The spurious asymmetry (4.40) may mask the APV asymmetry (4.36) because both exhibit the same behavior under field reversals. However, because the Stark-induced transition amplitude is nonzero when $F_f \neq I$, APV and Stark-induced asymmetries can be determined unambiguously by comparing transitions to different hyperfine levels of the final state.

We propose to measure the transition rate by observing fluorescence of the excited, and assume that the transition is not saturated:

$$\mathcal{I} < \mathcal{I}_{\rm sat} \equiv \Gamma/(4\pi\alpha\mathcal{Q}), \tag{4.41}$$

where the saturation intensity $\mathcal{I}_{\rm sat}$ is chosen so that $R = \Gamma$ when $\mathcal{I} = \mathcal{I}_{\rm sat}$. In this regime, fluorescence is proportional to the transition rate. The statistical sensitivity of this detection scheme is determined as follows: The number of excited atoms is

$$N_f = N_i R_\pm t \equiv N \pm N', \tag{4.42}$$

where N_i is the number of illuminated atoms, t is the measurement time, and N and $N' \ll N$ are the number of excited atoms due to parity-conserving and parity-violating processes. The signal-to-noise ratio is SNR $= N'/\sqrt{N}$, or

$$\mathrm{SNR} = 8\pi\alpha\mathcal{I}\zeta_0\sqrt{N_i t/\Gamma} = 2(\mathcal{I}/\mathcal{I}_{\mathrm{sat}})(\zeta_0/\mathcal{Q})\sqrt{N_i\Gamma t}. \tag{4.43}$$

The SNR is optimized by illuminating a large number of atoms with light that is intense, but does not saturate the $i \to f$ transition. Although purely statistical shot-noise dominated SNR does not depend on $\mathcal{Q}$, this parameter is still important in practice due to condition (4.41). Allowed $E1$-$E2$ and $E1$-$M1$ transitions are characterized by large $\mathcal{Q}$, which leads to small APV asymmetry. In the opposite case of forbidden $E1$-$E2$ and $E1$-$M1$ transitions (small $\mathcal{Q}$), an observable signal requires high light intensities, which may pose a technical challenge.

NSD APV mixing of $J = 1$ and $J = 2$ states

Mixing of $|f\rangle$ with nearby $J_a = 2$ states is qualitatively similar to the previous case. Here we make the comparison explicit. The amplitude of the transition induced by NSD APV mixing of $|f\rangle$ and $|a\rangle$ is (Appendix D):

$$A_{\mathrm{w}} = i\zeta_2\{\boldsymbol{\epsilon}\otimes\boldsymbol{\epsilon}\}_{2,-q}(-1)^q\langle F_i M_i; 2q|F_f M_f\rangle, \tag{4.44}$$

where

$$\zeta_2 = \frac{\Omega_{fa} d_{an} d_{ni}}{\sqrt{15}\omega_{af}\Delta}, \tag{4.45}$$

and $\{\boldsymbol{\epsilon}\otimes\boldsymbol{\epsilon}\}_{2q}$ is the qth spherical component of the rank-2 tensor formed by taking the dyadic product of $\boldsymbol{\epsilon}$ with itself [115]. For the geometry in Fig. 4.3, the transition rate is

$$R_\pm \propto C_1^2\mathcal{Q}^2 \pm \sqrt{2/3}C_1 C_2\zeta_2\mathcal{Q}, \tag{4.46}$$

where the positive (negative) sign is taken when $\mathbf{k}$ and $\mathbf{B}$ are aligned (anti-aligned), $C_k = \langle IM_f; k0|F_f M_f\rangle$ for $k = 1, 2$, and we have omitted a term proportional to ζ_2^2. For simplicity, we focus on the case $F_f = I + 1$ (the cases $F_f = I, I - 1$ are similar). In this case, Eq. (4.46) becomes

$$R_\pm \propto \frac{F_f^2 - M_f^2}{(I+1)(2I+1)}\left[\mathcal{Q}^2 \pm \frac{2\zeta_2\mathcal{Q}M_f}{\sqrt{2I(I+2)}}\right], \tag{4.47}$$

and the asymmetry is

$$\frac{R_+ - R_-}{R_+ + R_-} = \frac{2M_f}{\sqrt{2I(I+2)}}\frac{\zeta_2}{Q}, \tag{4.48}$$

which is maximal when $M_f = I$. In the case of maximal asymmetry, the SNR is

$$\mathrm{SNR} = 8\pi\alpha C_I\mathcal{I}\zeta_2\sqrt{N_i t/\Gamma} = 2C_I(\mathcal{I}/\mathcal{I}_{\mathrm{sat}})(\zeta_2/\mathcal{Q})\sqrt{N_i\Gamma t}. \tag{4.49}$$

where $C_I = \sqrt{I/[2(I+1)(I+2)]}$ is a numerical coefficient and $\mathcal{I}_{\rm sat}$ is given by Eq. (4.41).

Static electric fields may induce a $J = 0 \to 1$ transition via Stark mixing of $|f\rangle$ and $|a\rangle$, giving rise to systematic effects that may mimic APV. When $J_a = 2$, the amplitude of Stark-induced transitions is (Appendix D):

$$A_{\rm s} = \xi_2[E_{-q} - 3(\boldsymbol{\epsilon}\cdot\mathbf{E})\boldsymbol{\epsilon}_{-q}](-1)^q\langle F_i M_i; 1q|F_f M_f\rangle, \tag{4.50}$$

where

$$\xi_2 = \frac{d_{fa}d_{an}d_{ni}}{15\sqrt{3}\omega_{af}\Delta}. \tag{4.51}$$

The spurious asymmetry due to Stark mixing is characterized by the rotational invariant

$$(\mathbf{k}\times\mathbf{B})\cdot[\mathbf{E} - 3(\boldsymbol{\epsilon}\cdot\mathbf{E})\boldsymbol{\epsilon}]. \tag{4.52}$$

Unlike for the $J_a = 0$ case, both the Stark effect and the electroweak interaction may induce transitions to $F_f = I, I \pm 1$ hyperfine levels of $|f\rangle$ when $J_a = 2$, eliminating the possibility of using APV-free transitions to control systematic effects. However, the Stark- and electroweak-interaction- induced asymmetries have different dependence on M_f:

$$\frac{R_+ - R_-}{R_+ + R_-} = \underbrace{\frac{2M_f}{\sqrt{2I(I+2)}}\frac{\zeta_2}{Q}}_{\rm APV} + \underbrace{\frac{(2I+1)M_f}{F_f^2 - M_f^2}\frac{\theta\xi_2\tilde{E}}{Q}}_{\rm Stark}, \tag{4.53}$$

where $\tilde{E}$ is defined by $\theta\tilde{E} \equiv (\mathbf{k}\times\mathbf{B})\cdot[\mathbf{E} - 3(\boldsymbol{\epsilon}\cdot\mathbf{E})\boldsymbol{\epsilon}]$. Thus APV can be distinguished from spurious asymmetries by analyzing the Zeeman structure of the transition, *e.g.*, by comparing transitions to sublevels $M_f = I$ and $M_f = I - 1$ of the final state.

As a final note, in addition to the rotational invariant (4.33), there is a second parity-violating rotational invariant that arises when $|f\rangle$ mixes with $J = 2$ states:

$$(\mathbf{k}\cdot\mathbf{B})(\boldsymbol{\epsilon}\cdot\mathbf{B})^2. \tag{4.54}$$

This rotational invariant describes APV interference in transitions for which $M_f = M_i \pm 1$.

Applications of DPS

We now turn our attention to the two-photon 462 nm $5s^2\ {}^1S_0 \to 5s9p\ {}^1P_1$ transition in ^{87}Sr ($Z = 38$, $I = 9/2$). The transition is enhanced by the intermediate $5s5p\ {}^1P_1$ state ($\Delta = 34$ cm^{-1}), and the parity-violating $E1$-$E1$ transition is induced by NSD APV mixing of the $5s9p\ {}^1P_1$ and $5s10s\ {}^1S_0$ states ($\omega_{af} = 184$ cm^{-1}). We used expressions presented in Ref. [47] to calculate the NSD APV matrix element: $\Omega_{fa} \approx 10\kappa$ s^{-1}, where κ is a dimensionless constant of order unity that characterizes the strength of NSD APV. The width of the transition is determined by the natural width $\Gamma = 1.15\times10^7$ s^{-1} of the $5s9p\ {}^1P_1$ state [102].

Table 4.2: Available atomic data for application of DPS to Sr and Ra. Here a_0 is the Bohr radius.

	Transition $(1 \to 2)$	$d_{21}/(ea_0)$
Sr[a]	$5s^2\ {}^1S_0 \to 5s5p\ {}^1P_1$	5.4
Ra[b]	$7s^2\ {}^1S_0 \to 7s7p\ {}^1P_1$	5.8
	$7s7p\ {}^1P_1 \to 7s6d\ {}^3D_2$	0.6
	$7s6d\ {}^3D_2 \to 7s7p\ {}^3P_1$	4.8

[a]Ref. [102], [b]Ref. [49]

Other essential atomic parameters are given in Table 4.2. Resolution of the magnetic sublevels of the final state requires a magnetic field larger than $2\Gamma/g \approx 10$ G, where $g \approx 0.1$ is the Landé factor of the $F = I$ hyperfine level of the $5s9p\ {}^1P_1$ state. We estimate that $d_{an} \approx ea_0$, $\mathcal{Q}_{fn}/d_{an} \approx \alpha/2$, and $\mu_{fn} \ll Q_{fn}$. Then the APV asymmetry associated with this system is about $4\kappa \times 10^{-8}$.

Spurious asymmetries due to stray electric fields can be ignored when

$$\theta E \ll 2(2I+1)\sqrt{I(I+1)}(\zeta_0/\xi_0) \approx 2 \text{ mV/cm}. \tag{4.55}$$

In ongoing APV experiments in Yb [112], stray electric fields on the order of 1 V/cm have been observed. Assuming a similar magnitude of stray fields for the Sr system, spurious Stark-induced asymmetries can be ignored by controlling misalignment of the light propagation and the magnetic field to better than $\theta < 0.1°$. Regardless of misalignment errors, APV can be discriminated from Stark-induced asymmetries by comparing transitions to the $F \neq 9/2$ hyperfine levels of the final $5s9p\ {}^1P_1$ state.

To estimate the SNR, we consider experimental parameters similar to those of Ref. [111]: $N_i \approx 10^7$ atoms illuminated by a laser beam of characteristic radius 0.3 mm. Optimal statistical sensitivity is realized when $\mathcal{I} = \mathcal{I}_{\text{sat}} \approx 6 \times 10^5$ W/cm^2. In this case, Eq. (4.43) yields SNR $\approx \kappa \times 10^{-3}\sqrt{t/\text{s}}$. The saturation intensity corresponds to light power of about 2 kW at 462 nm. High light powers may be achieved in a running-wave power buildup cavity. With this level of sensitivity, about 300 hours of measurement time are required to achieve unit SNR. The projected asymmetry and SNR for the Sr system are to their observed counterparts in the most precise measurements of NSD APV in Tl [116].

Another potential candidate for the DPS is the 741 nm $7s^2\ {}^1S_0 \to 7s7p\ {}^3P_1$ transition in unstable ^{225}Ra ($Z = 88$, $I = 3/2$, $t_{1/2} = 15$ days). This system lacks an intermediate state whose energy is nearly half that of the final state; the closest state is $7s7p\ {}^1P_1$ ($\Delta \approx 14000$ cm^{-1}). Nevertheless, it is a good candidate for the DPS, partly due to the presence of nearly-degenerate opposite-parity levels $7s7p\ {}^3P_1$ and $7s6d\ {}^3D_2$ ($\omega_{af} = 5$ cm^{-1}). In this system, NSD APV mixing arises due to nonzero admixture of configuration $7p^2$ in the $7s6d\ {}^3D_2$ state [54]. Numerical calculations yield $\Omega_{fa}d_{an}/\omega_{af} \approx 2\kappa \times 10^{-9}\ ea_0$ [46] and $\Gamma = 2.8 \times 10^6$ s^{-1} [49]. Other essential atomic parameters are given in Table 4.2. Like for the Sr system, we estimate that $Q_{fn}/d_{an} = \alpha/2$ and $\mu_{fn} \ll Q_{fn}$, yielding an approximate

asymmetry of $7\kappa \times 10^{-6}$. Laser cooling and trapping of ^{225}Ra has been demonstrated [67], producing about $N_i \approx 20$ trapped atoms. When $\mathcal{I} = \mathcal{I}_{\rm sat} \approx 10^8$ W/cm^2, Eq. (4.49) gives SNR $= \kappa \times 10^{-2}\sqrt{t/\mathrm{s}}$. For a laser beam of 0.3 mm, the saturation intensity corresponds to light power of about 300 kW at 741 nm. These estimates suggest that unit SNR can be realized in under 3 hours of observation time. Compared to the Sr system, the Ra system potentially exhibits both a much larger asymmetry and a much higher statistical sensitivity.

Finally, we note that while we considered atoms with zero nuclear spin, the AOS could also be applied to isotopes with nonzero nuclear spin provided that the detuning Δ is much larger than the hyperfine splitting of the intermediate state.

Chapter 5

Future APV experiments

One goal of the future measurements of the parity-violation effects in ytterbium is observing a difference in the APV effect between different isotopes [113]. The net uncertainty of the APV parameter of a single isotope must be better than 1% based on the theoretical predictions. To this end, a program of the apparatus upgrades and improvements is developed. Besides general improvements of the stability of the system parameters, increase of the signal levels, suppression of the electronics noise etc., the main focus is on elimination of the frequency excursions of the frequency reference, which is a major source of the statistical noise. Improving the statistical uncertainty will contribute to more precise measurement and control of the electric-field-imperfection contribution to the systematic part of the uncertainty. The latter is another high-priority improvement essential for reaching the goal.

In the future apparatus, the referencing of the optical system to the Fabry-Pérot étalon will be replaced by locking the system to a femtosecond frequency comb. The impact of the electric field imperfection is planned to be substantially suppressed by redesigning of the interaction region to provide more uniform and controlled electric field distribution. Until now, no scientific or technical obstacles were discovered preventing us to improve the apparatus to the desired level of sensitivity.

As an alternative approach, we also presented two schemes for measuring APV using interference of parity-conserving $E1$-$M1$ (or $E1$-$E2$) and parity-violating $E1$-$E1$ two-photon transition amplitudes: the AOS and DPS. The AOS allows for observations of NSI APV in the absence of external static electric and magnetic fields. This method measures the rate of a transition between two energy eigenstates with zero total electronic angular momentum. We derived general expressions for the two-photon transition rate and SNR. Because the AOS uses optical fields rather than static electric and magnetic fields, systematic effects due to field misalignments are easier to minimize in the AOS than in the 408 nm system in ytterbium.

To demonstrate the feasibility of the AOS, we estimated the SNR of the $6s^2\ {}^1S_0 \rightarrow 6s6p\ {}^3P_0$ transition in ytterbium ($\lambda_1 = 399$ nm, $\lambda_2 = 1.28$ μm). A comparison of the schemes using the single-photon ${}^1S_0 \rightarrow {}^3D_1$ and the two-photon ${}^1S_0 \rightarrow {}^3P_0$ transitions can be found in Table 5.1. Our estimate of the SNR suggests that this system is a promising

Table 5.1: Summary of APV methods. SNRs have been estimated for 1 s of integration time and are valid when the statistical uncertainty is limited by photon shot noise. For the 408 nm system in ytterbium, the asymmetry $\mathcal{A}$ corresponds to an external electric field of amplitude 4 kV/cm.

Technique	Atom	Transition	P_1 (W)	λ_1 (nm)	P_2 (W)	λ_2 (nm)	$\mathcal{A}$	SNR
Stark	^{174}Yb	$^1S_0 \rightarrow {}^3D_1$	10	408			10^{-5}	3
AOS	^{174}Yb	$^1S_0 \rightarrow {}^3P_0$	10^{-2}	399	10	1280	10^{-5}	2
DPS	^{87}Sr	$^1S_0 \rightarrow {}^1P_1$	10^3	462			$10^{-8}\kappa$	$10^{-3}\kappa$
DPS	^{225}Ra	$^1S_0 \rightarrow {}^3P_1$	10^5	741			$10^{-5}\kappa$	$10^{-2}\kappa$

candidate for a cross-check of our recent APV measurement and for future measurements of APV in a chain of isotopes.

Whereas the AOS is best suited for NSI APV measurements, the DPS provides a means for measuring NSD APV without NSI background. The DPS uses two-photon $J = 0 \rightarrow 1$ transitions driven by collinear photons of the same frequency, for which NSI APV effects are suppressed by BES. We identified transitions in strontium-87 and radium-225 that are promising candidates for application of the DPS. The estimated asymmetries and SNRs of those systems are presented alongside the ytterbium systems in Table 5.1. The radium system boasts a large asymmetry and SNR compared to the strontium system. However, the short lifetime of the unstable radium-225 nucleus poses several experimental challenges.

Nevertheless the future of APV looks bright, with ongoing experiments in dysprosium [90], francium [64], radium ions [44, 63], and diatomic molecules [35]. The one- and two-photon ytterbium systems described herein are especially exciting given that they exhibit large APV asymmetries and are characterized by large SNRs, opening the door to high-precision APV measurements in a chain of isotopes.

Bibliography

[1] Dana Z. Anderson, Josef C. Frisch, and Carl S. Masser. "Mirror reflectometer based on optical cavity decay time". In: *Appl. Opt.* 23.8 (Apr. 1984), pp. 1238–1245.

[2] J. R. P. Angel and P. G. H. Sandars. "The Hyperfine Structure Stark Effect. I. Theory". In: *Proceedings of the Royal Society of London. Series A. Mathematical and Physical Sciences* 305.1480 (1968), pp. 125–138.

[3] S. H. Autler and C. H. Townes. "Stark Effect in Rapidly Varying Fields". In: *Physical Review* 100 (2 Oct. 1955), pp. 703–722.

[4] M. Auzinsh, D. Budker, and S. Rochester. *Optically Polarized Atoms*. Oxford University Press, 2010.

[5] Z. W. Barber et al. "Optical Lattice Induced Light Shifts in an Yb Atomic Clock". In: *Physical Review Letters* 100 (10 Mar. 2008), p. 103002.

[6] P. Bargueño, I. Gonzalo, and R. Pérez de Tudela. "Detection of parity violation in chiral molecules by external tuning of electroweak optical activity". In: *Physical Review A* 80 (1 July 2009), p. 012110.

[7] L. M. Barkov and M. S. Zolotorev. "Observation of parity nonconservation in atomic transitions". In: *Soviet Physics Soviet Physics Journal of Experimental and Theoretical Physics Letters* 27.6 (Mar. 1978). [*Pis'ma Zh. Eksp. Teor. Fiz.*, 27(6):379–383, Mar 1978], pp. 357–361.

[8] L. M. Barkov and M. S. Zolotorev. "Parity nonconservation in bismuth atoms and neutral weak-interaction currents". In: *Soviet Physics Journal of Experimental and Theoretical Physics Letters* 52.3 (Sept. 1980). [*Zh. Eksp. Teor. Fiz.*, 79(3):713, Sep 1980], pp. 360–369.

[9] D. R. Beck and L. Pan. "Improved RCI techniques for atomic $4f^n$ excitation energies and polarizabilities". In: *Journal of Physics B: Atomic, Molecular and Optical Physics* 43.7 (2010), p. 074009.

[10] G. N. Birich et al. "Nonconservation of parity in atomic bismuth". In: *Soviet Physics Soviet Physics Journal of Experimental and Theoretical Physics Letters* 60.3 (Sept. 1984). [*Zh. Eksp. Teor. Fiz.*, 87(3):776, Sep 1984], pp. 442–449.

[11] K. B. Blagoev and V. A. Komarovskii. "Lifetimes of Levels of Neutral and Singly Ionized Lanthanide Atoms". In: *Atomic Data and Nuclear Data Tables* 56.1 (1994), pp. 1–40.

[12] K. D. Bonin and M. A. Kadar-Kallen. "Linear Electric-Dipole Polarizabilities". In: *International Journal of Modern Physics B* 08.24 (1994), pp. 3313–3370.

[13] K. D. Bonin and V. V. Kresin. *Electric-Dipole Polarizabilities of Atoms, Molecules, and Clusters*. World Scientific Publishing Co. Pte. Ltd., 1997.

[14] K. D. Bonin and T. J. McIlrath. "Two-photon electric-dipole selection rules". In: *Journal of the Optical Society of America B* 1.1 (Mar. 1984), pp. 52–55.

[15] M.-A. Bouchiat. Private communication.

[16] M.-A. Bouchiat. "Measuring the Fr Weak Nuclear Charge by Observing a Linear Stark Shift with Small Atomic Samples". In: *Physical Review Letters* 100 (12 Mar. 2008), p. 123003.

[17] M.-A. Bouchiat and C. Bouchiat. "Parity violation in atoms". In: *Reports on Progress in Physics* 60.11 (1997), p. 1351.

[18] M.-A. Bouchiat and C. Bouchiat. "Parity violation induced by weak neutral currents in atomic physics I". In: *Journal de Physique* 35.12 (1974), pp. 899–927.

[19] M.-A. Bouchiat and C. Bouchiat. "Parity violation induced by weak neutral currents in atomic physics II". In: *Journal de Physique* 36.6 (1975), pp. 493–509.

[20] M.-A. Bouchiat et al. "Observation of a parity violation in cesium". In: *Physics Letters B* 117.5 (1982), pp. 358–364.

[21] C. J. Bowers et al. "Experimental investigation of excited-state lifetimes in atomic ytterbium". In: *Physical Review A* 53 (5 May 1996), pp. 3103–3109.

[22] C. J. Bowers et al. "Experimental investigation of the $6s^2\ {}^1S_0 \rightarrow 5d6s\ {}^3D_{1,2}$ forbidden transitions in atomic ytterbium". In: *Physical Review A* 59 (5 May 1999), pp. 3513–3526.

[23] B. A. Brown, A. Derevianko, and V. V. Flambaum. "Calculations of the neutron skin and its effect in atomic parity violation". In: *Physical Review C* 79 (3 Mar. 2009), p. 035501.

[24] D. Budker and J. E. Stalnaker. "Magnetoelectric Jones Dichroism in Atoms". In: *Physical Review Letters* 91 (26 Dec. 2003), p. 263901.

[25] C. Amsler *et al.* (Particle Data Group). "Review of Particle Physics". In: *Physics Letters B* 667.1–5 (2008), pp. 1–6.

[26] C. W. Chou et al. "Frequency Comparison of Two High-Accuracy Al^+ Optical Clocks". In: *Physical Review Lett.* 104 (7 Feb. 2010), p. 070802.

[27] E. D. Commins. "Atomic parity violation experiments". In: *Physica Scripta* 36.3 (1987), p. 468.

[28] R. Conti et al. "Preliminary Observation of Parity Nonconservation in Atomic Thallium". In: *Physical Review Letters* 42 (6 Feb. 1979), pp. 343–346.

[29] A. D. Cronin et al. "Studies of Electromagnetically Induced Transparency in Thallium Vapor and Possible Utility for Measuring Atomic Parity Nonconservation". In: *Physical Review Letters* 80 (17 Apr. 1998), pp. 3719–3722.

[30] B. P. Das. "Computation of correlation effects on the parity-nonconserving electric-dipole transition in atomic ytterbium". In: *Physical Review A* 56 (2 Aug. 1997), pp. 1635–1637.

[31] B. DeBoo et al. "Multichannel conical emission and parametric and nonparametric nonlinear optical processes in ytterbium vapor". In: *Journal of the Optical Society of America B* 18.5 (May 2001), pp. 639–645.

[32] B. Deissler et al. "Measurement of the ac Stark shift with a guided matter-wave interferometer". In: *Physical Review A* 77 (3 Mar. 2008), p. 031604.

[33] D. DeMille. "Parity Nonconservation in the $6s^2\ ^1S_0 \rightarrow 6s5d\ ^3D_1$ Transition in Atomic Ytterbium". In: *Physical Review Letters* 74 (21 May 1995), pp. 4165–4168.

[34] D. DeMille et al. "How we know that photons are bosons: Experimental tests of spin-statistics for photons". In: *AIP Conference Proceedings* 545.1 (2000). Ed. by Robert C. Hilborn and Guglielmo M. Tino, pp. 227–340.

[35] D. DeMille et al. "Using Molecules to Measure Nuclear Spin-Dependent Parity Violation". In: *Physical Review Letters* 100 (2 Jan. 2008), p. 023003.

[36] W. Demtröder. *Laser Spectroscopy*. 3rd. Springer-Verlag, 2003.

[37] A. Derevianko, V. A. Dzuba, and K. Beloy. Private communication.

[38] D. R. Dounas-Frazer et al. "Atomic parity violation in $J = 0 \rightarrow 0$ two-photon transitions". In: *Physical Review A* 84 (2 Aug. 2011), p. 023404.

[39] D. R. Dounas-Frazer et al. "Atomic parity violation in two-photon $J = 0 \rightarrow 1$ transitions". In: *Il Nuovo Cimento C* 35 (4 Aug. 2012), pp. 91–96.

[40] D. R. Dounas-Frazer et al. "Measurement of dynamic Stark polarizabilities by analyzing spectral line shapes of forbidden transitions". In: *Physical Review A* 82 (6 Dec. 2010), p. 062507.

[41] P. S. Drell and E. D. Commins. "Parity Nonconservation in Atomic Thallium". In: *Physical Review Letters* 53 (10 Sept. 1984), pp. 968–971.

[42] R. W. P. Drever et al. "Laser phase and frequency stabilization using an optical resonator". In: *Applied Physics B: Lasers and Optics* 31 (2 1983). 10.1007/BF00702605, pp. 97–105.

[43] V. A. Dzuba and A. Derevianko. "Dynamic polarizabilities and related properties of clock states of the ytterbium atom". In: *Journal of Physics B: Atomic, Molecular and Optical Physics* 43.7 (2010), p. 074011.

[44] V. A. Dzuba and V. V. Flambaum. "Calculation of nuclear-spin-dependent parity nonconservation in $s \to d$ transitions of Ba^+, Yb^+, and Ra^+ ions". In: *Physical Review A* 83 (5 May 2011), p. 052513.

[45] V. A. Dzuba and V. V. Flambaum. "Calculation of parity nonconservation in neutral ytterbium". In: *Physical Review A* 83 (4 Apr. 2011), p. 042514.

[46] V. A. Dzuba, V. V. Flambaum, and J. S. M. Ginges. "Calculation of parity and time invariance violation in the radium atom". In: *Physical Review A* 61 (6 May 2000), p. 062509.

[47] V. A. Dzuba, V. V. Flambaum, and C. Harabati. "Relations between matrix elements of different weak interactions and interpretation of the parity-nonconserving and electron electric-dipole-moment measurements in atoms and molecules". In: *Physical Review A* 84 (5 Nov. 2011), p. 052108.

[48] V. A. Dzuba, V. V. Flambaum, and I. B. Khriplovich. "Enhancement of P- and T-nonconserving effects in rare-earth atoms". In: *Zeitschrift für Physik D: Atoms, Molecules and Clusters* 1 (3 1986), pp. 243–245.

[49] V. A. Dzuba and J. S. M. Ginges. "Calculations of energy levels and lifetimes of low-lying states of barium and radium". In: *Physical Review A* 73 (3 Mar. 2006), p. 032503.

[50] N. H. Edwards et al. "Precise Measurement of Parity Nonconserving Optical Rotation in Atomic Thallium". In: *Physical Review Letters* 74.14 (Apr. 1995), pp. 2654–2657.

[51] C. R. Ekstrom et al. "Measurement of the electric polarizability of sodium with an atom interferometer". In: *Physical Review A* 51.5 (May 1995), pp. 3883–3888.

[52] D. English, V. V. Yashchuk, and D. Budker. "Spectroscopic Test of Bose-Einstein Statistics for Photons". In: *Physical Review Letters* 104.25 (June 2010), p. 253604.

[53] Farhad H. M. Faisal. *Theory of Multiphoton Processes*. Plenum Press, 1987.

[54] V. V. Flambaum. "Enhancement of parity and time invariance violation in the radium atom". In: *Physical Review A* 60 (4 Oct. 1999), R2611–R2613.

[55] V. V. Flambaum and I. B. Khriplovich. "P-odd nuclear forces: A source of parity violation in atoms". In: *Soviet Physics Journal of Experimental and Theoretical Physics* 52.5 (Nov. 1980). [*Zh. Eksp. Teor. Fiz.*, 79(5):1656, Nov 1980], pp. 835–839.

[56] V. V. Flambaum and D. W. Murray. "Anapole moment and nucleon weak interactions". In: *Physical Review C* 56.3 (Sept. 1997), pp. 1641–1644.

[57] V. V. Flambaum and O. P. Sushkov. "Possibility of observing parity nonconservation by measuring the nuclear anapole moment using the NMR frequency shift in a laser beam". In: *Physical Review A* 47.2 (Feb. 1993), R751–R754.

[58] E. N. Fortson, Y. Pang, and L. Wilets. "Nuclear-structure effects in atomic parity nonconservation". In: *Phys. Rev. Lett.* 65 (23 Dec. 1990), pp. 2857–2860.

[59] N. Fortson. "Possibility of measuring parity nonconservation with a single trapped atomic ion". In: *Physical Review Letters* 70.16 (Apr. 1993), pp. 2383–2386.

[60] Jerome I. Friedman and V. L. Telegdi. "Nuclear Emulsion Evidence for Parity Nonconservation in the Decay Chain $\pi^+ - \mu^+ - e^+$". In: *Physical Review* 105 (5 Mar. 1957), pp. 1681–1682.

[61] R. L. Garwin, L. M. Lederman, and M. Weinrich. "Observations of the Failure of Conservation of Parity and Charge Conjugation in Meson Decays: the Magnetic Moment of the Free Muon". In: *Physical Review* 105 (4 Feb. 1957), pp. 1415–1417.

[62] J. S. M. Ginges and V. V. Flambaum. "Violations of fundamental symmetries in atoms and tests of unification theories of elementary particles". In: *Physics Reports* 397.2 (2004), pp. 63–154.

[63] G. S. Giri et al. "Isotope shifts of the $6d\ ^2D_{3/2} - 7p\ ^2P_{1/2}$ transition in trapped short-lived $^{209-214}Ra^+$". In: *Physical Review A* 84 (2 Aug. 2011), p. 020503.

[64] E. Gomez et al. "Measurement method for the nuclear anapole moment of laser-trapped alkali-metal atoms". In: *Physical Review A* 75 (3 Mar. 2007), p. 033418.

[65] J. Guéna, M. Lintz, and M.-A. Bouchiat. "Measurement of the parity violating $6S-7S$ transition amplitude in cesium achieved within 2×10^{-13} atomic-unit accuracy by stimulated-emission detection". In: *Physical Review A* 71.4 (Apr. 2005), p. 042108.

[66] J. Guéna et al. "New Manifestation of Atomic Parity Violation in Cesium: A Chiral Optical Gain Induced by Linearly Polarized $6S-7S$ Excitation". In: *Physical Review Letters* 90.14 (Apr. 2003), p. 143001.

[67] J. R. Guest et al. "Laser Trapping of ^{225}Ra and ^{226}Ra with Repumping by Room-Temperature Blackbody Radiation". In: *Physical Review Letters* 98 (9 Feb. 2007), p. 093001.

[68] M. Gunawardena and D. S. Elliott. "Atomic Homodyne Detection of Weak Atomic Transitions". In: *Physical Review Letters* 98.4 (Jan. 2007), p. 043001.

[69] M. Gunawardena and D. S. Elliott. "Weak signal detection using coherent control". In: *Physical Review A* 76.3 (Sept. 2007), p. 033412.

[70] R.A. Harris and L. Stodolsky. "Quantum beats in optical activity and weak interactions". In: *Physics Letters B* 78.2-3 (1978), pp. 313–317.

[71] W. C. Haxton, C.-P. Liu, and M. J. Ramsey-Musolf. "Nuclear anapole moments". In: *Physical Review C* 65.4 (Mar. 2002), p. 045502.

[72] W. C. Haxton and C. E. Wieman. "ATOMIC PARITY NONCONSERVATION AND NUCLEAR ANAPOLE MOMENTS". In: *Annual Review of Nuclear and Particle Science* 51.1 (2001), pp. 261–293.

[73] J. H. Hollister et al. "Measurement of Parity Nonconservation in Atomic Bismuth". In: *Physical Review Letters* 46 (10 Mar. 1981), pp. 643–646.

[74] C. J. Hood, H. J. Kimble, and J. Ye. "Characterization of high-finesse mirrors: Loss, phase shifts, and mode structure in an optical cavity". In: *Physical Review A* 64 (3 Aug. 2001), p. 033804.

[75] C. J. Horowitz et al. "Parity violating measurements of neutron densities". In: *Physical Review C* 63.2 (Jan. 2001), p. 025501.

[76] M. A. Kadar-Kallen and K. D. Bonin. "Light-force technique for measuring polarizabilities". In: *Physical Review Letters* 68.13 (Mar. 1992), pp. 2015–2018.

[77] M. A. Kadar-Kallen and K. D. Bonin. "Uranium polarizability measured by light-force technique". In: *Physical Review Letters* 72.6 (Feb. 1994), pp. 828–831.

[78] I. B. Khriplovich. *Parity Nonconservation in Atomic Phenomena*. Gordon and Breach Science Publishers S.A., 1991.

[79] D. F. Kimball. "Parity-nonconserving optical rotation on the $6s6p\ ^3P_0 \rightarrow 6s6p\ ^1P_1$ transition in atomic ytterbium". In: *Physical Review A* 63.5 (Apr. 2001), p. 052113.

[80] D. F. Kimball et al. "Collisional perturbation of states in atomic ytterbium by helium and neon". In: *Physical Review A* 60 (2 Aug. 1999), pp. 1103–1112.

[81] M. G. Kozlov, D. English, and D. Budker. "Symmetry-suppressed two-photon transitions induced by hyperfine interactions and magnetic fields". In: *Physical Review A* 80.4 (Oct. 2009), p. 042504.

[82] M.G. Kozlov. "Manifestation of the nuclear anapole moment in the thallium $M1$ transitions". English. In: *Soviet Physics Journal of Experimental and Theoretical Physics Letters* 75 (11 2002). [*Pis'ma Zh. Eksp. Teor. Fiz.*, 75(11):651–654, 2002], pp. 534–538.

[83] T. D. Lee and C. N. Yang. "Question of Parity Conservation in Weak Interactions". In: *Physical Review* 104 (1 Oct. 1956), pp. 254–258.

[84] R. Loudon. *The Quantum Theory of Light*. Oxford University Press, 2000.

[85] M. J. D. Macpherson et al. "Precise measurement of parity nonconserving optical rotation at 876 nm in atomic bismuth". In: *Physical Review Letters* 67.20 (Nov. 1991), pp. 2784–2787.

[86] P. Mandal and M. Mukherjee. "Quantum metrology to probe atomic parity nonconservation". In: *Physical Review A* 82.5 (Nov. 2010), p. 050101.

[87] D. M. Meekhof et al. "High-precision measurement of parity nonconserving optical rotation in atomic lead". In: *Physical Review Letters* 71 (21 Nov. 1993), pp. 3442–3445.

[88] J. Mitroy, M. S. Safronova, and C. W. Clark. "Theory and applications of atomic and ionic polarizabilities". In: *Journal of Physics B: Atomic, Molecular and Optical Physics* 43.20 (2010), p. 202001.

[89] Atsuo Morinaga, Toshiharu Tako, and Nobuhiko Ito. "Sensitive measurement of phase shifts due to the ac Stark effect in a Ca optical Ramsey interferometer". In: *Physical Review A* 48.2 (Aug. 1993), pp. 1364–1368.

[90] A. T. Nguyen et al. "Search for parity nonconservation in atomic dysprosium". In: *Physical Review A* 56.5 (Nov. 1997), pp. 3453–3463.

[91] A.-T. Nguyen et al. "Search for PNC in atomic Dysprosium". In: *Parity Violation in Atoms and Electron Scattering*. Ed. by B. Frois and M. A. Bouchiat. World Scientific, 1999, p. 295.

[92] E. Noether. "Invariant variation problems". In: *Transport Theory and Statistical Physics* 1.3 (Sept. 1971). [*Nachr. D. König. Gesellsch. D. Wiss. Zu Göttingen, Math-Phys. Klasse, S.*, 235–257, 1918], pp. 186–207.

[93] P. L. Anthony *et al.* (SLAC E158 Collaboration). "Precision Measurement of the Weak Mixing Angle in Møller Scattering". In: *Physical Review Letters* 95 (8 Aug. 2005), p. 081601.

[94] S. G. Porsev, K. Beloy, and A. Derevianko. "Precision Determination of Electroweak Coupling from Atomic Parity Violation and Implications for Particle Physics". In: *Physical Review Letters* 102.18 (May 2009), p. 181601.

[95] S. G. Porsev, Yu. G. Rakhlina, and M. G. Kozlov. "Electric-dipole amplitudes, lifetimes, and polarizabilities of the low-lying levels of atomic ytterbium". In: *Physical Review A* 60.4 (Oct. 1999), pp. 2781–2785.

[96] S. G. Porsev, Yu. G. Rakhlina, and M. G. Kozlov. "Parity violation in atomic ytterbium". In: *Soviet Physics Journal of Experimental and Theoretical Physics Letters* 61.6 (1995). [*Pis'ma Zh. Eksp. Teor. Fiz.*, 61(6):449–453, 1995], pp. 459–63.

[97] S.G. Porsev, M.G. Kozlov, and Yu.G. Rakhlina. "Manifestation of nuclear spin dependent P odd electron-nucleon interaction in atomic ytterbium". In: *Hyperfine Interactions* 127 (1 2000). 10.1023/A:1012605414957, pp. 395–398.

[98] W. H. Press et al. *Numerical Recipes: The Art of Scientific Computing*. Third. Cambridge University Press, 2007.

[99] S. Rochester et al. "Measurement of lifetimes and tensor polarizabilities of odd-parity states of atomic samarium". In: *Physical Review A* 59.5 (May 1999), pp. 3480–3494.

[100] U. I. Safronova and M. S. Safronova. "Relativistic many-body calculations of the oscillator strengths, transition rates and polarizabilities in Zn-like ions". In: *Journal of Physics B: Atomic, Molecular and Optical Physics* 43.7 (2010), p. 074025.

[101] J. J. Sakurai. *Invariance Principles and Elementary Particles*. Princteon, 1964.

[102] J. E. Sansonetti and G. Nave. "Wavelengths, Transition Probabilities, and Energy Levels for the Spectrum of Neutral Strontium (Sr I)". In: *Journal of Physical and Chemical Reference Data* 39.3, 033103 (2010), p. 033103.

[103] A. Schäfer et al. "Prospects for an atomic parity-violation experiment in U^{90+}". In: *Physical Review A* 40.12 (Dec. 1989), pp. 7362–7365.

[104] Joel A. Silver. "Frequency-modulation spectroscopy for trace species detection: theory and comparison among experimental methods". In: *Applied Optics* 31.6 (Feb. 1992), pp. 707–717.

[105] Angom Dilip Singh and Bhanu Pratap Das. "Parity non-conservation in atomic Yb arising from the nuclear anapole moment". In: *Journal of Physics B: Atomic, Molecular and Optical Physics* 32.20 (1999), p. 4905.

[106] I. I. Sobelman. *Atomic Spectra and Radiative Transitions*. Springer-Verlag, 1992.

[107] J. E. Stalnaker et al. "Dynamic Stark effect and forbidden-transition spectral line shapes". In: *Physical Review A* 73.4 (Apr. 2006), p. 043416.

[108] J. E. Stalnaker et al. "Measurement of the forbidden $6s^2\ ^1S_0 \rightarrow 5d6s\ ^3D_1$ magnetic-dipole transition amplitude in atomic ytterbium". In: *Physical Review A* 66.3 (Sept. 2002), p. 031403.

[109] M. Takamoto et al. "An optical lattice clock". In: *Nature* 435 (Mar. 2005), pp. 321–324.

[110] M. L. Ter-Mikhaelyan. "Simple atomic systems in resonant laser fields". In: *Physics-Uspekhi* 40.12 (1997), pp. 1195–1238.

[111] K. Tsigutkin et al. "Observation of a Large Atomic Parity Violation Effect in Ytterbium". In: *Physical Review Letters* 103.7 (Aug. 2009), p. 071601.

[112] K. Tsigutkin et al. "Parity violation in atomic ytterbium: Experimental sensitivity and systematics". In: *Physical Review A* 81.3 (Mar. 2010), p. 032114.

[113] K. Tsigutkin et al. "Towards measuring nuclear-spin-dependent and isotopic-chain atomic parity violation in Ytterbium". In: *From Parity Violation to Hadronic Structure and more*. Springer, 2007.

[114] T. Udem. "Timekeeping: Light-insensitive optical clock". In: *Nature* 435 (May 2005), p. 291.

[115] D. A. Varshalovich, A. N. Moskalev, and V. K. Khersonskii. *Quantum Theory of Angular Momentum*. World Scientific, 1988.

[116] P. A. Vetter et al. "Precise Test of Electroweak Theory from a New Measurement of Parity Nonconservation in Atomic Thallium". In: *Physical Review Letters* 74.14 (Apr. 1995), pp. 2658–2661.

[117] L. W. Wansbeek et al. "Atomic parity nonconservation in Ra^+". In: *Physical Review A* 78 (5 Nov. 2008), p. 050501.

[118] R. B. Warrington, C. D. Thompson, and D. N. Stacey. "A New Measurement of Parity-Non-Conserving Optical Rotation at 648 nm in Atomic Bismuth". In: *Europhysics Letters* 24.8 (1993), p. 641.

[119] C. E. Wieman et al. “Asymmetric line shapes for weak transitions in strong standing-wave fields”. In: *Physical Review Letters* 58.17 (Apr. 1987), pp. 1738–1741.

[120] C. S. Wood et al. “Measurement of Parity Nonconservation and an Anapole Moment in Cesium”. In: *Science* 275.5307 (1997), pp. 1759–1763.

[121] C. S. Wood et al. “Precision measurement of parity nonconservation in cesium”. In: *Canadian Journal of Physics* 77.1 (1999), pp. 7–75.

[122] C. S. Wu et al. “Experimental Test of Parity Conservation in Beta Decay”. In: *Physical Review* 105 (4 Feb. 1957), pp. 1413–1415.

[123] J. Ye, H. J. Kimble, and H. Katori. “Quantum State Engineering and Precision Metrology Using State-Insensitive Light Traps”. In: *Science* 320.5884 (2008), pp. 1734–1738.

[124] Ya. B. Zel’dovich. “Parity Nonconservation in Electron Scattering and in other Effects in the First Order of the Weak Interaction Coupling Constant”. In: *Soviet Physics Journal of Experimental and Theoretical Physics* 9 (1959). [*Zh. Eksp. Teor. Fiz.*, 36:964, 1959], p. 682.

[125] Ya. B. Zel’dovich. “Prediction of anapole moments in nuclei”. In: *Soviet Physics Journal of Experimental and Theoretical Physics* 6 (1958). [*Zh. Eksp. Teor. Fiz.*, 33:1531, 1958], p. 1184.

Appendix A

Details of the Yb APV experiment

In this appendix, we derive the transition amplitudes relevant to the Yb APV experiment. Additionally, we present a characterization of the gradual decrease of the PBC finesse over time due to mirror degradation, and we derive the asymmetry correction factor due to phase mixing.

A.1 Derivation of transition amplitudes

The total Hamiltonian (before including light-atom interactions and assuming $\mathbf{B}$ is along $\hat{\mathbf{z}}$) can be written as

$$H = H_{\mathrm{A}} + H_{\mathrm{Z}} + H_{\mathrm{S}} + H_{\mathrm{APV}}, \tag{A.1}$$

where H_{A} is the atomic Hamiltonian and H_{Z}, H_{S}, and H_{APV} represent the contributions from the static magnetic field $\mathbf{B}$, the static electric field $\mathbf{E}$, and the parity non-conserving electroweak interaction, respectively. Here

$$H_{\mathrm{Z}} = -\boldsymbol{\mu} \cdot \mathbf{B} = g\mu_0 \mathbf{J} \cdot \mathbf{B} = g\mu_0 J_z B, \tag{A.2}$$

where $\boldsymbol{\mu} = -g\mu_0\mathbf{J}$ is the magnetic dipole moment of the atom, g is the Landé factor, μ_0 is the Bohr magneton, and $\mathbf{J}$ is the angular-momentum operator. Similarly,

$$H_{\mathrm{S}} = -\mathbf{d} \cdot \mathbf{E} = -d_i E_i, \tag{A.3}$$

where $\mathbf{d}$ is the atomic electric-dipole operator. Finally,

$$H_{\mathrm{APV}} = iH_0^{(0)}, \tag{A.4}$$

where $H_0^{(0)}$ is a scalar operator. Summation over repeated indices is assumed.

In the presence of a strong magnetic field, that is, when Zeeman splitting dominates Stark-shifts, it is useful to think of $H_1 \equiv H_{\mathrm{S}} + H_{\mathrm{APV}}$ as a perturbation to $H_0 \equiv H_{\mathrm{A}} + H_{\mathrm{Z}}$. In this case, the LS-coupled states $|^{2S+1}L_J; M\rangle$, such as $|^3D_1; M\rangle$ and $|^1S_0; 0\rangle$, are eigenstates

of the unperturbed Hamiltonian H_0. Then the first-order perturbation theory can be used to determine the eigenstates of the total Hamiltonian:

$$|\overline{a}\rangle = |a\rangle + \sum_{a'} \frac{|a'\rangle\langle a'|H_1|a\rangle}{\omega(a) - \omega(a')}, \tag{A.5}$$

where $\omega(a)$ is the energy of state $|a\rangle$. (Perturbed eigenstates are denoted using an overbar.)

The electric-dipole amplitude for the optical transition of interest is

$$A_{E1}(M) = \langle \overline{^3D_1; M}|(-\mathbf{d}\cdot\boldsymbol{\mathcal{E}})|\overline{^1S_0}\rangle \equiv A_{\rm s}(M) + A_{\rm pv}(M), \tag{A.6}$$

where

$$A_{\rm s}(M) = \sum_{a'} \left[\frac{\langle ^3D_1; M|\mathbf{d}\cdot\mathbf{E}|a'\rangle\langle a'|\mathbf{d}\cdot\boldsymbol{\mathcal{E}}|^1S_0\rangle}{\omega(^3D_1) - \omega(a')} + \frac{\langle ^3D_1; M|\mathbf{d}\cdot\boldsymbol{\mathcal{E}}|a'\rangle\langle a'|\mathbf{d}\cdot\mathbf{E}|^1S_0\rangle}{\omega(^1S_0) - \omega(a')} \right], \tag{A.7}$$

and

$$A_{\rm pv}(M) = \sum_{a'} \left[\frac{\langle ^3D_1; M|iH_0^{(0)}|a'\rangle\langle a'|\mathbf{d}\cdot\boldsymbol{\mathcal{E}}|^1S_0\rangle}{\omega(^3D_1) - \omega(a')} - \frac{\langle ^3D_1; M|\mathbf{d}\cdot\boldsymbol{\mathcal{E}}|a'\rangle\langle a'|iH_0^{(0)}|^1S_0\rangle}{\omega(^1S_0) - \omega(a')} \right]. \tag{A.8}$$

The Stark amplitude can be written as

$$A_{\rm s}(M) = T_{ij}\langle ^3D_1; M|U_{ij}|^1S_0\rangle, \tag{A.9}$$

where $T_{ij} = E_i\mathcal{E}_j$ and

$$U_{ij} = \sum_{a'} \frac{d_i|a'\rangle\langle a'|d_j}{\omega(^3D_1) - \omega(a')} + \frac{d_j|a'\rangle\langle a'|d_i}{\omega(^1S_0) - \omega(a')}. \tag{A.10}$$

Let $T_q^{(k)}$ and $U_q^{(k)}$ represent the irreducible spherical components of the tensors T_{ij} and U_{ij}. Then $T_{ij}U_{ij} = (-1)^q T_{-q}^{(k)} U_q^{(k)}$ and Eq. (A.7) becomes

$$\begin{aligned} A_{\rm s}(M) &= (-1)^q T_{-q}^{(k)} \langle ^3D_1; M|U_q^{(k)}|^1S_0\rangle \\ &= (-1)^q T_{-q}^{(k)} \frac{(^3D_1||U^{(k)}||^1S_0)}{\sqrt{3}} \langle 00; kq|1M\rangle \\ &= i\beta(-1)^q (\mathbf{E}\times\boldsymbol{\mathcal{E}})_{-q} \langle 00; 1q|1M\rangle. \end{aligned} \tag{A.11}$$

Here β is the vector Stark transition polarizability and defined by

$$\beta \equiv \frac{1}{\sqrt{6}}(^1S_0||U^{(1)}||^3D_1). \tag{A.12}$$

To derive Eq. (A.11), we used $\langle 00; kq|1M\rangle = \delta_{k1}\delta_{qM}$ and

$$T^{(1)}_{-q} = \sum_{q_1,q_2} \langle 1q_1; 1q_2|1-q\rangle E_{q_1}\mathcal{E}_{q_2} = (i/\sqrt{2})(\mathbf{E}\times\boldsymbol{\mathcal{E}})_{-q}. \tag{A.13}$$

For the parity-violating contribution to the $E1$ transition amplitude we can likewise write

$$A_{\rm pv}(M) = i\mathcal{E}_i\langle {}^3D_1; M|W_i|{}^1S_0\rangle, \tag{A.14}$$

where

$$W_i = \sum_{a'}\left[\frac{H^{(0)}_0|a'\rangle\langle a'|d_i}{\omega({}^3D_1)-\omega(a')} - \frac{d_i|a'\rangle\langle a'|H^{(0)}_0}{\omega({}^1S_0)-\omega(a')}\right]. \tag{A.15}$$

Let $\mathcal{E}^{(1)}_q$ and $W^{(1)}_q$ represent the spherical components of the vectors $\mathcal{E}_i$ and W_i, respectively. Then $\mathcal{E}_iW_i = (-1)^q\mathcal{E}^{(1)}_{-q}W^{(1)}_q$ and we have

$$\begin{aligned} A_{\rm pv}(M) &= i(-1)^q\mathcal{E}^{(1)}_{-q}\langle {}^3D_1; M|W^{(1)}_q|{}^1S_0\rangle \\ &= i(-1)^q\mathcal{E}^{(1)}_{-q}\frac{({}^3D_1||W^{(1)}||{}^1S_0)}{\sqrt{3}}\langle 00; 1q|1M\rangle \\ &= i\zeta(-1)^q\mathcal{E}^{(1)}_{-q}\langle 00; 1q|1M\rangle. \end{aligned} \tag{A.16}$$

Here ζ is given by

$$\zeta \equiv \frac{1}{\sqrt{3}}({}^3D_1||W^{(1)}||{}^1S_0). \tag{A.17}$$

A.2 Characterization of the PBC mirrors

The finesse of the cavity is measured using the cavity-ring-down method [1]. The laser beam is sent through a Pockels cell (Cleveland Crystals Inc. QX 1020 Q-Switch) and a polarizer before entering the cavity. The polarizer is aligned with the laser polarization so that the light is transmitted when there is no voltage applied to the Pockels cell. A high-voltage pulse generator is used to send a fast step signal (30-ns wavefront) to the Pockels cell which rotates the polarization of the light so that it is not transmitted through the polarizer. The laser frequency is locked to the resonance frequency of the cavity, and then the Pockels cell is switched into the non-transmitting state, causing a fast interruption of the laser power. The subsequent decay of the light inside the cavity is monitored with a fast photodiode (50-MHz bandwidth) measuring the power transmitted through the back mirror of the cavity. The signal is fit to an exponential decay. The decay time is related to the finesse of the cavity ($\mathcal{F}$) by

$$\mathcal{F} = \frac{\pi c}{L}\tau,$$

where c is the speed of light, L is the cavity length, and τ is the intensity decay time. An example of the PBC transmission signal and its fit are shown in Fig. A.1.

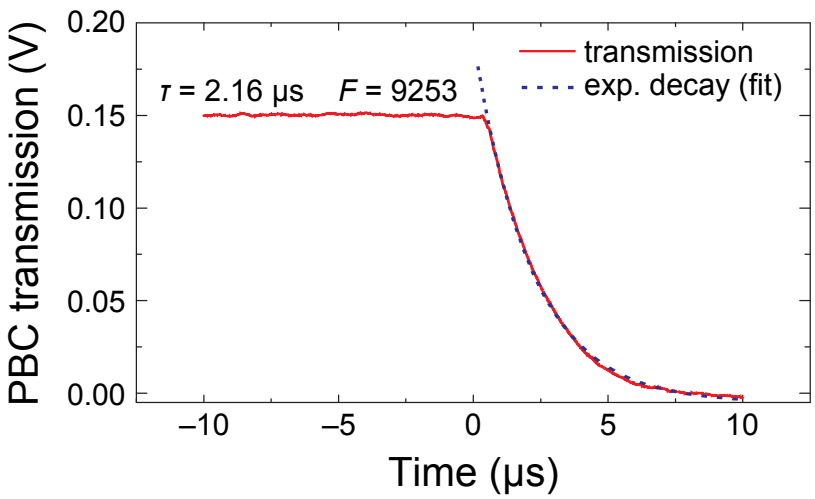

Figure A.1: Application of the cavity-ring-down method for the determination of the finesse of PBC.

Following the analysis discussed in [74], if we denote the transmission of mirrors 1 and 2 by T_1 and T_2, respectively, and the absorption+scatter loss per mirror as $l_{1,2} = (A+S)_{1,2}$, then the total cavity losses $\mathcal{L} = T_1 + T_2 + l_1 + l_2$ determine the finesse $\mathcal{F}$:

$$\mathcal{F} = \frac{2\pi}{T_1 + T_2 + l_1 + l_2}. \tag{A.18}$$

Information on the transmission of the mirrors discriminated from the A+S losses can be obtained using the measured value of the finesse and the power transmitted trough PBC, P_{tr}:

$$\frac{P_{tr}}{\epsilon P_{in}} = 4T_1T_2\left(\frac{\mathcal{F}}{2\pi}\right)^2, \tag{A.19}$$

where P_{in} is the input power, and ϵ is a mode-matching factor. For two arbitrary mirrors, for which neither $T_{1,2}$ nor $l_{1,2}$ are known the Eq. (A.18,A.19) do not provide a solution, since a number of variables exceeds the number of equations. Nevertheless, for two mirrors from the same coating run when one can assume that $T_1 = T_2 = T$ and $l_1 = l_2 = l$, the equations (A.18,A.19) become

$$\mathcal{F} = \frac{\pi}{T + l}.$$
$$\frac{P_{tr}}{\epsilon P_{in}} = 4T^2\left(\frac{\mathcal{F}}{2\pi}\right)^2,$$

and for known mode-matching factor ϵ the parameters of the mirrors (T and l) can be determined. The factor ϵ depends on the geometry of the cavity, and is assumed to stay

constant upon replacing of the mirrors, if the geometry of the input laser beam and the configuration of the PBC are unchanged. This gives the possibility to calibrate this factor by using a mirror set for which the transmission is known. We used for this purpose the mirror set purchased from Advanced Thin Films, Inc., for which reliable data on the transmission of the mirrors is provided by the supplier. By measuring the finesse of the PBC comprised of these mirrors and the ratio of the transmitted-to-input power, the mode-matching factor and the A+S mirror losses l are found. This set is not an actual mirror set that was used in the APV experiment, nevertheless, the parameters of other mirrors were determined by replacing one mirror in the "reference" set by the "test" mirror, parameters of which are sought. The geometry of the cavity was unchanged during the replacement. This tactic allows for the measurement of parameters of any arbitrary mirror.

A.3 Impact of the phase mixing effect on the harmonics ratio

Atoms undergo the $6s^2\,{}^1S_0 \to 5d6s\,{}^3D_1$ transition in the interaction region where they are illuminated by 408-nm light and are exposed to the static magnetic field and the oscillating electric field $E(t)$. Excited atoms then spontaneously decay from the $5d6s\,{}^3D_1$ state to the metastable $6s6p\,{}^3P_0$ state. The population of $6s6p\,{}^3P_0$ is proportional to the transition rate R_M for $M = 0, \pm 1$. Without loss of generality, we assume that the constant of proportionality is equal to one and we consider the case $M = 0$. For convenience, we define $R \equiv R(0)$.

The rate R is measured in the probe region. The probe region is located a distance $d \approx 20$ cm away from the interaction region. Therefore, an atom that arrives at the detection region at time t experienced an electric field with magnitude $E(t - d/v_z)$ in the interaction region, where v_z is the atom's speed and d/v_z is the amount of time required for the atom to travel a distance d.

Because some atoms travel faster or slower than others, the detection region is full of atoms that have each experienced a different electric field while in the interaction region. Each atom contributes to the total rate and hence the observed rate $\overline{R}$ is the thermal average of every contribution:

$$\overline{R}(t; \omega, d, v_{\mathrm{T}}) = \int_0^\infty R(t - d/v_z) f(v_z; v_{\mathrm{T}})\, dv_z, \tag{A.20}$$

where

$$f(v_z; v_{\mathrm{T}})\, dv_z = 2(v_z/v_{\mathrm{T}})^3 e^{-(v_z/v_{\mathrm{T}})^2} dv_z/v_{\mathrm{T}}, \tag{A.21}$$

is the probability for an atom to have speed between v_z and $v_z + dv_z$. Here $v_{\mathrm{T}} = \sqrt{2k_B T/m}$ is the thermal speed, $T \approx 873$ K is the oven temperature, and $m = 161$ GeV$/c^2$ is the atomic mass of Yb, yielding $v_{\mathrm{T}} = 2.9 \times 10^4$ cm/s.

It is convenient to introduce the dimensionless variables $x = v_z/v_{\rm T}$ and $\tau = \omega t$, and the dimensionless parameter $\alpha = \omega d/v_{\rm T}$. Then the average rate $\overline{R}(t;\omega,d,v_{\rm T}) \to \overline{R}(\tau;\alpha)$ depends only on the dimensionless quantities α and τ, and Eq. (A.20) becomes

$$\overline{R}(\tau;\alpha) = R_0 + R_1|I(\alpha)|\cos(\tau + \mathrm{Arg}[I(\alpha)]) + R_2|I(2\alpha)|\cos(2\tau + \mathrm{Arg}[I(2\alpha)]), \qquad \text{(A.22)}$$

with

$$I(\alpha) \equiv \int_0^\infty e^{-i\alpha/x} f(x;1)\,dx. \qquad \text{(A.23)}$$

Note that $|I(\alpha)| \to 0$ as $\alpha \to \infty$ whereas $|I(\alpha)| \approx 1$ when $\alpha < 1$. This places a limit on the modulation frequency: We require that $\omega < v_{\rm T}/d = 2\pi\times$ 230 Hz in order to avoid a significant decrease in signal.

The lock-in amplifier receives an input signal proportional to $\overline{R}$ and returns two output signals S_1 and S_2 corresponding to the first and second harmonic components, respectively. This process can be modeled as

$$\begin{aligned} S_n(\phi_n;\alpha) &= \frac{1}{\pi}\int_0^{2\pi} \overline{R}(\tau;\alpha)\cos(n\tau+\phi_n)\,d\tau \\ &= R_n|I(n\alpha)|\cos(\mathrm{Arg}[I(n\alpha)]+\phi_n), \end{aligned} \qquad \text{(A.24)}$$

where the phases $\phi_{1,2}$ of the lock-in amplifier are chosen to maximize the signals $S_{1,2}$. That is,

$$\phi_n = \phi_n(\alpha) \equiv -\mathrm{Arg}[I(n\alpha)]. \qquad \text{(A.25)}$$

Our measurement $\mathcal{S}$ is the ratio of the first- and second- harmonic signals:

$$\mathcal{S} = \frac{S_1(\phi_1;\alpha)}{S_2(\phi_2;\alpha)} = \frac{R_1|I(\alpha)|}{R_2|I(2\alpha)|} = \mathcal{A}\times C(\alpha), \qquad \text{(A.26)}$$

where $C(\alpha) \equiv |I(\alpha)|/|I(2\alpha)|$ is the *correction factor*. Therefore, we must further divide the ratio $\mathcal{S}$ of observed output signals by $C(\alpha)$ to measure the ratio $\mathcal{A}$.

The correction factor $C(\alpha)$ and the optimal lock-in phases $\phi_{1,2}(\alpha)$ inherit dependence on the modulation frequency ($\omega = 2\pi\times 76.2$ Hz), the distance between interaction and detection regions ($d \approx 20$ cm), and the oven temperature ($T \approx 873$ K) through the parameter α:

$$\alpha = \frac{\omega\, d}{\sqrt{2k_B T/m}} = 0.33(2), \qquad \text{(A.27)}$$

where the uncertainty in α is given by

$$\delta\alpha = \alpha\sqrt{(\delta T/2T)^2 + (\delta d/d)^2}, \qquad \text{(A.28)}$$

for $\delta T \approx 50$ K and $\delta d \approx 1$ cm. The correction factor can be computed numerically and has a value

$$C_0 = C(\alpha) = 1.028(3), \tag{A.29}$$

with uncertainty given by $\delta C_0 = |C'(\alpha)|\,\delta\alpha$. Likewise, the lock-in phases have the following values

$$\phi_{10} = \phi_1(\alpha) = 16(1)^\circ, \quad \phi_{20} = \phi_2(\alpha) = 33(2)^\circ, \tag{A.30}$$

where $\delta\phi_{n0} = |\phi_n'(\alpha)|\,\delta\alpha$.

In order to understand the impact of imperfect phase selections, we include the effects of slight deviations from the optimal phase $\phi_n(\alpha)$ by taking

$$\phi_n \to \phi_n(\alpha) + \varphi_n, \tag{A.31}$$

where $\varphi_n \approx 0$ represents a small deviation. Then the correction factor becomes

$$C(\alpha) \to \tilde{C}(\alpha, \varphi_1, \varphi_2) = C(\alpha) \times \frac{\cos(\varphi_1)}{\cos(\varphi_2)}, \tag{A.32}$$

and hence $\tilde{C}_0 = \tilde{C}(\alpha, 0, 0) = C(\alpha) = C_0$. The uncertainty in the correction factor becomes

$$\delta C_0 \to \delta\tilde{C}_0 = \sqrt{\delta C_0^2 + \delta\varphi_1^4 + \delta\varphi_2^4}, \tag{A.33}$$

where $\delta\varphi_n$ is the uncertainty in the deviation φ_n. To derive this expression, we estimated the partial uncertainty in $\tilde{C}_0$ due to φ_n by $\partial^2_{\varphi_n}\tilde{C}(\alpha, \varphi_1, \varphi_2)\,\delta\varphi_n^2$.

To estimate the uncertainty $\delta\varphi_n$, we assume that we are within about 1° of the optimal phase. This choice is consistent with the magnitude of the uncertainty in the optimal phases ϕ_{10} and ϕ_{20}. Therefore, we will take $\delta\varphi_n = \delta\phi_{n0}$ to be the accuracy with which we can select the lock-in phases. Then $\delta\varphi_1 = 0.02$, $\delta\varphi_2 = 0.03$, and

$$\delta\tilde{C}_0 = 0.0031 \approx 0.0029 = \delta C_0. \tag{A.34}$$

Hence small deviations (on the order of 1°) have a negligible effect on the uncertainty in the correction factor.

Appendix B

Details of the AC polarizability experiment

In this appendix, we present the frequency dependence of the dynamic polarizabilities and describe the system of equations used in the LSM numerical simulation.

B.1 Frequency dependence of dynamic polarizabilities

The ac polarizability α_ℓ of the state $|\ell\rangle = |\gamma JM\rangle$ is given by Eq. (3.9). The scalar, vector, and tensor polarizabilities depend on the light frequency ω in the following way [12, 13]:[1]

$$\alpha_0(\gamma J) = \frac{1}{3\hbar} \sum_{\ell' \neq \ell} \frac{|d_{\ell\ell'}|^2}{2J+1} F^+_{\ell\ell'}(\omega)\ \Phi_0(J, J'), \tag{B.1}$$

$$\alpha_1(\gamma J) = \frac{1}{2\hbar} \sum_{\ell' \neq \ell} \frac{|d_{\ell\ell'}|^2}{2J+1} F^-_{\ell\ell'}(\omega)\ \Phi_1(J, J'), \tag{B.2}$$

$$\alpha_2(\gamma J) = \frac{1}{3\hbar} \sum_{\ell' \neq \ell} \frac{|d_{\ell\ell'}|^2}{2J+1} F^+_{\ell\ell'}(\omega)\ \Phi_2(J, J'). \tag{B.3}$$

Here the summation is over all states $|\ell'\rangle = |\gamma' J' M'\rangle$ such that $|\ell\rangle$ and $|\ell'\rangle$ have opposite parity. The functions Φ_0, Φ_1 and Φ_2 are given by

$$\Phi_0(J, J') = \delta_{JJ'} + \delta_{J,J'+1} + \delta_{J,J'-1}, \tag{B.4}$$

$$\Phi_1(J, J') = -\frac{\delta_{JJ'}}{(J+1)} + \frac{J\,\delta_{J,J'+1}}{J+1} - \delta_{J,J'-1}, \tag{B.5}$$

[1] Reference [40] adopts a different convention for the Stark shift, and hence the ac polarizability. However, that work erroneously defines the ac polarizability according to Eqs. (B.1), (B.2), and (B.3) presented here. These equations are consistent with the convention for the ac Stark shift used in this dissertation, *i.e.*, Eq. (3.7), and are inconsistent with the convention followed in Ref. [40].

and

$$\Phi_2(J,J') = \frac{(2J-1)\delta_{JJ'}}{J+1} - \frac{J(2J-1)\delta_{J,J'+1}}{(J+1)(2J+3)} - \delta_{J,J'-1}, \tag{B.6}$$

where $\delta_{JJ'}$ is the Kronecker delta. We emphasize that $\Phi_1(J, J')$ differs from the expression found in Refs. [12, 13] by a factor of J. The reason for this discrepancy is that we follow the convention for which the vector polarizability of a stretched state ($M = J$) is $\alpha_1(\gamma J)$ instead of $J \times \alpha_1(\gamma J)$.

The frequency-dependent parts of Eqs. (B.1) through (B.3) are given by

$$F^{\pm}_{\ell\ell'}(\omega) = \frac{1}{\omega_{\ell'\ell} - \omega - i\Gamma_{\ell'}/2} \pm \frac{1}{\omega_{\ell'\ell} + \omega + i\Gamma_{\ell'}/2}. \tag{B.7}$$

Here $d_{\ell\ell'} \equiv (\gamma J||d^{(1)}||\gamma' J')$ is the reduced matrix element of the electric dipole operator and $d^{(1)}$ is the spherical tensor associated with the electric dipole moment. In the limit of large detuning from resonance ($|\omega_{\ell'\ell} \pm \omega| \gg \Gamma_{\ell'}$), the functions $F^{\pm}_{\ell\ell'}$ reduce to

$$F^{+}_{\ell\ell'} = \frac{2\omega_{\ell'\ell}}{(\omega^2_{\ell'\ell} - \omega^2)} \quad \text{and} \quad F^{-}_{\ell\ell'} = \frac{2\omega}{(\omega^2_{\ell'\ell} - \omega^2)}. \tag{B.8}$$

B.2 System of equations used in numerical model

For computational purposes, it is convenient to express Eqs. (3.30) and (3.34) as

$$\frac{d\boldsymbol{\rho}}{d\tau} = \mathbf{f}(\boldsymbol{\rho}, \tau), \quad \boldsymbol{\rho}(-\tau_0) = 0, \tag{B.9}$$

where $\tau_0 = 3/(S_3 u_\perp)$. Here $\boldsymbol{\rho} = (\rho_0, \ldots, \rho_5)$, $\rho_0 = \rho_{aa}$, $\rho_1 = \rho_{bb}$, $\rho_2 = \rho_{cc}$, $\rho_3 = \mathrm{Re}[\rho_{ga}]$, $\rho_4 = \mathrm{Im}[\rho_{ga}]$, $\rho_5 = \mathcal{F}$, and $\mathbf{f} = (f_0, \ldots, f_5)$. The components of $\mathbf{f}$ are given by

$$f_0 = -\rho_0 + \Omega\,\rho_4, \tag{B.10}$$

$$f_1 = -G_b\,\rho_1 + G_{ab}\,\rho_0, \tag{B.11}$$

$$f_2 = -G_c\,\rho_2 + G_{ac}\,\rho_0, \tag{B.12}$$

$$f_3 = -\frac{1}{2}\rho_3 - \Delta\rho_4, \tag{B.13}$$

$$f_4 = -\frac{1}{2}\rho_4 + \Delta\rho_3 - \frac{\Omega}{2}(2\rho_0 + \rho_1 + \rho_2 - 1), \tag{B.14}$$

$$f_5 = +G_b\,\rho_1, \tag{B.15}$$

where Ω and Δ are given by Eqs. (3.31) and (3.32), respectively. To derive Eq. (B.9), we eliminated the population ρ_{gg} of the ground state from the OBE using the conservation of probability: $\sum_n \rho_{nn} = 1$. The fluorescence defined in Eq. (3.34) is given by

$$\mathcal{F}(\boldsymbol{\xi}, \mathbf{u}) = \rho_5(\tau_0; \boldsymbol{\xi}, \mathbf{u}). \tag{B.16}$$

Thus the fluorescence can be obtained by numerically solving the system of equations (B.9), as described in the text.

Appendix C

Derivation of transition amplitudes for the AOS

In this appendix, we derive amplitudes for $E1$-$M1$ and induced $E1$-$E1$ $J_i = 0 \to J_f = 0$ transitions. We use the following convention for the Wigner-Eckart theorem (WET). Let T_k be an irreducible tensor of rank k with spherical components T_{kq} for $q \in \{0, \pm 1, \ldots, \pm k\}$. Then the WET is [106]

$$\langle J_2 M_2 | T_{kq} | J_1 M_1 \rangle = (J_2 || T_k || J_1) \frac{\langle J_1 M_1; kq | J_2 M_2 \rangle}{\sqrt{2J_2 + 1}}, \tag{C.1}$$

where $(J_2||T_k||J_1)$ is the reduced matrix element of T_k and $\langle J_1 M_1; kq | J_2 M_2 \rangle$ is a Clebsch-Gordan coefficient.

The amplitude for the $E1$-$M1$ transition is [53]

$$\begin{aligned} A_{E1-M1} = {} & A_{E1-M1}(1,2) + A_{E1-M1}(2,1) \\ & + A_{M1-E1}(1,2) + A_{M1-E1}(2,1), \end{aligned} \tag{C.2}$$

where

$$A_{E1-M1}(j, j') = \langle f | (\hat{\mathbf{k}}_{j'} \times \boldsymbol{\epsilon}_{j'}) \cdot \boldsymbol{\mu} \frac{|n\rangle\langle n|}{\omega_{ni} - \omega_j} \boldsymbol{\epsilon}_j \cdot \mathbf{d} | i \rangle, \tag{C.3}$$

and

$$A_{M1-E1}(j, j') = \langle f | \boldsymbol{\epsilon}_{j'} \cdot \mathbf{d} \frac{|a\rangle\langle a|}{\omega_{ai} - \omega_j} (\hat{\mathbf{k}}_j \times \boldsymbol{\epsilon}_j) \cdot \boldsymbol{\mu} | i \rangle, \tag{C.4}$$

for $j, j' = 1, 2$. Here $\boldsymbol{\mu}$ and $\mathbf{d}$ are the magnetic- and electric-dipole moments of the atom, and summation over the magnetic sublevels of the intermediate states $|n\rangle$ and $|a\rangle$ is implied.

$E1$-$E1$ transitions are induced by mixing of the states $|n\rangle$ and $|a\rangle$ due to the electroweak interaction and, in the presence of a static electric field, the Stark effect. The perturbed states $|n\rangle + \chi|a\rangle$ and $|a\rangle - \chi^*|n\rangle$ act as intermediate states for the two paths that contribute to the induced $E1$-$E1$ amplitude. Here χ is a small dimensionless parameter that depends on

the details of the perturbing Hamiltonian. The amplitude for the induced $E1$-$E1$ transition is [53]

$$A_{E1-E1} = A_{E1-E1}(1,2) + A_{E1-E1}(2,1), \tag{C.5}$$

where

$$A_{E1-E1}(j,j') = \langle f|\boldsymbol{\epsilon}_{j'}\cdot\mathbf{d}\left[\frac{\chi|a\rangle\langle n|}{\omega_{ni}-\omega_j} - \frac{|a\rangle\langle n|\chi}{\omega_{ai}-\omega_j}\right]\boldsymbol{\epsilon}_j\cdot\mathbf{d}|i\rangle. \tag{C.6}$$

Like for Eqs. (C.3, C.4), summation over the magnetic sublevels of states $|n\rangle$ and $|a\rangle$ is implied.

When the mixing of $|n\rangle$ and $|a\rangle$ is due to the electroweak interaction alone, the perturbation parameter is given by $\chi = \chi_{\rm W}$ where

$$\chi_{\rm W} = \frac{\langle a|H_{\rm NSD}|n\rangle}{\omega_{na}} = \frac{i}{\sqrt{3}}\frac{\Omega_{an}}{\omega_{na}}, \tag{C.7}$$

for $J_a = J_n$ and $M_a = M_n$. Here Ω_{an} is a real parameter related to the reduced matrix element of $H_{\rm NSD}$ by $(J_a||H_{\rm NSD}||J_n) = i\Omega_{an}$. The factor of i preserves time reversal invariance [78].

In the presence of a static electric field $\mathbf{E}$, the perturbation parameter becomes $\chi = \chi_{\rm W} + \chi_{\rm S}$, where $\chi_{\rm W}$ is given by Eq. (C.7) and

$$\chi_{\rm S} = \frac{\langle a|H_{\rm S}|n\rangle}{\omega_{na}} = -\frac{d_{an}E_q^*}{\omega_{na}}\frac{\langle J_nM_n;1q|J_aM_a\rangle}{\sqrt{2J_a+1}}, \tag{C.8}$$

where d_{an} is the reduced matrix element of the electric-dipole operator. Here $H_{\rm S} = -\mathbf{d}\cdot\mathbf{E}$ is the Stark Hamiltonian, E_q is the qth spherical component of $\mathbf{E}$, $E_q^* = (-1)^q E_{-q}$, and $q = M_a - M_n$. In this case, $A_{E1-E1} = A_{\rm w} + A_{\rm s}$, where $A_{\rm w} \propto \chi_{\rm W}$ and $A_{\rm s} \propto \chi_{\rm S}$ are the amplitudes of the transitions induced by the electroweak interaction and Stark effect, respectively.

For a general $J_i \to J_f$ transition, the Stark-induced $E1$-$E1$ amplitude may have contributions from each of the irreducible tensors that can be formed by the three vectors $\boldsymbol{\epsilon}_1$, $\boldsymbol{\epsilon}_2$, and $\mathbf{E}$. There are seven such tensors: one of rank 0, three of rank 1, two of rank 2, and one of rank 3. However, for a $J_i = 0 \to J_f = 0$ transition, only the rank-0 tensor contributes. This tensor is [115]

$$T_{00} = \sum_{\lambda,q}\langle 1\lambda;1q|00\rangle\{\boldsymbol{\epsilon}_1\otimes\boldsymbol{\epsilon}_2\}_{1\lambda}E_q = -\frac{i}{\sqrt{6}}\mathbf{E}\cdot(\boldsymbol{\epsilon}_1\times\boldsymbol{\epsilon}_2), \tag{C.9}$$

where

$$\{\boldsymbol{\epsilon}_1\otimes\boldsymbol{\epsilon}_2\}_{1\lambda} = \sum_{\mu,\nu}\langle 1\mu;1\nu|1\lambda\rangle\epsilon_{1\mu}\epsilon_{2\nu} = \frac{i}{\sqrt{2}}(\boldsymbol{\epsilon}_1\times\boldsymbol{\epsilon}_2)_\lambda \tag{C.10}$$

is the irreducible tensor of rank 1 formed by $\boldsymbol{\epsilon}_1$ and $\boldsymbol{\epsilon}_2$. Here $\lambda,\ q,\ \mu,\ \nu = 0,\ \pm 1$ are the spherical components of $\{\boldsymbol{\epsilon}_1 \otimes \boldsymbol{\epsilon}_2\}_1$, $\mathbf{E}$, $\boldsymbol{\epsilon}_1$, and $\boldsymbol{\epsilon}_2$, respectively. The Stark-induced transition amplitude is

$$A_{\rm s} = i[\xi(\omega_1) - \xi(\omega_2)][\mathbf{E} \cdot (\boldsymbol{\epsilon}_1 \times \boldsymbol{\epsilon}_2)]. \tag{C.11}$$

The coefficient $\xi(\omega_j)$ can be expressed in terms of reduced electric-dipole matrix elements by applying the WET to Eq. (C.5) with $\chi = \chi_{\rm S}$ and comparing the result to Eq. (C.11). This procedure yields

$$\xi(\omega_j) = \frac{1}{3\sqrt{6}} \frac{d_{fa}\, d_{an}\, d_{ni}}{\omega_{na}} \left(\frac{1}{\omega_{ni} - \omega_j} - \frac{1}{\omega_{ai} - \omega_j} \right). \tag{C.12}$$

The Stark effect may also cause the final state $|f\rangle$ to mix with nearby opposite-parity $J = 1$ states. In this case, Eq. (C.11) is still valid, but Eq. (C.12) must be modified to account for additional admixtures of states.

Expressions (4.3) and (4.44) for the amplitudes of the $E1$-$M1$ and electroweak interaction-induced $E1$-$E1$ transitions are derived by direct application of the WET to Eqs. (C.2) and (C.5). The Stark-induced $E1$-$E1$ amplitude in Eq. (C.11) reduces to expression (4.20) when $|\Delta| \ll |\omega_{na}|$ and $|\Delta| \ll |\omega_2 - \omega_{ni}|$.

Appendix D

Derivation of transition amplitudes for the DPS

In this appendix, we derive amplitudes for induced $E1$-$E1$ $J = 0 \to 1$ transitions between opposite parity states.

D.1 Bose-Einstein statistics selection rules

Here we provide a brief review of BES selection rules for $J = 0 \to 1$ transitions driven by degenerate ($\omega_1 = \omega_2 \equiv \omega$), co-propagating ($\mathbf{k}_1 = \mathbf{k}_2 \equiv \mathbf{k}$) photons [34]. Since the only transitions of relevance are of this type, they are referred to as simply "degenerate transitions" without cumbersome qualifiers. We ignore hyperfine interaction (HFI) effects by assuming that there is zero nuclear spin.

It must be possible to write the absorption amplitude A for a degenerate transition in terms of the only quantities available: the polarizations of the two photons, $\boldsymbol{\epsilon}_1$ and $\boldsymbol{\epsilon}_2$; the final polarization of the atom in its excited $J = 1$ state, $\boldsymbol{\epsilon}_e$; and the photon momentum $\mathbf{k}$. With the requirement of gauge invariance of the photons ($\boldsymbol{\epsilon}_{1,2} \cdot \mathbf{k} = 0$), only three forms of A are possible:

$$A_a \propto (\boldsymbol{\epsilon}_1 \times \boldsymbol{\epsilon}_2) \cdot \boldsymbol{\epsilon}_e; \tag{D.1a}$$

$$A_b \propto (\boldsymbol{\epsilon}_1 \cdot \boldsymbol{\epsilon}_2)(\boldsymbol{\epsilon}_e \cdot \mathbf{k}); \tag{D.1b}$$

$$A_c \propto [(\boldsymbol{\epsilon}_1 \times \boldsymbol{\epsilon}_2) \cdot \mathbf{k}](\boldsymbol{\epsilon}_e \cdot \mathbf{k}). \tag{D.1c}$$

Amplitudes A_a and A_c are odd under photon interchange, and hence vanish because photons obey BES. However, amplitude A_b is even and may yield a nonzero absorption amplitude. In the case of degenerate transitions between atomic states of the same total parity, A_b vanishes because it is odd under spatial inversion. Hence degenerate transitions between like-parity states are forbidden by BES selection rules[1]. However, degenerate transitions may be allowed when the initial and final states are of opposite parity.

[1] Parity-conserving perturbations, such as the Zeeman effect or the hyperfine interaction, may induce

When $\boldsymbol{\epsilon}_1 = \boldsymbol{\epsilon}_2 \equiv \boldsymbol{\epsilon}$, as would be the case if the photons were absorbed from the same laser beam, the degenerate transition amplitude reduces to $A_b \propto (\boldsymbol{\epsilon}\cdot\boldsymbol{\epsilon})\mathbf{k}\cdot\boldsymbol{\epsilon}_e$. Therefore, the amplitude of a degenerate transition between opposite parity states is

$$A_b = i(\boldsymbol{\epsilon}\cdot\boldsymbol{\epsilon})\mathcal{Q}k_{-M}(-1)^M, \tag{D.2}$$

where $k_{-M}(-1)^M$ is the projection of $\hat{\mathbf{k}}$ onto the spin of the excited atom and the factor of i ensures time reversal invariance.

D.2 Wigner-Eckart theorem

We use the following convention for the Wigner-Eckart theorem (WET). Let T_k be an irreducible tensor of rank k with spherical components T_{kq} for $q \in \{0, \pm1, \ldots, \pm k\}$. Then the WET is [106]

$$\langle J_2 I F_2 M_2 | T_{kq} | J_1 I F_1 M_1\rangle = \frac{(J_2 I F_2 || T_k || J_1 I F_1)}{\sqrt{2F_2+1}}\langle F_1 M_1; kq | F_2 M_2\rangle, \tag{D.3}$$

where $(J_2 I F_2 || T_k || J_1 I F_1)$ is the reduced matrix element of T_k and $\langle F_1 M_1; kq | F_2 M_2\rangle$ is a Clebsch-Gordan coefficient. If T_k commutes with the nuclear spin $\mathbf{I}$, then its reduced matrix element satisfies [106]

$$\frac{(J_2 I F_2 || T_k || J_1 I F_1)}{\sqrt{2F_2+1}} = (-1)^{J_2+I+F_1+k}(J_2||T_k||J_1)\times\sqrt{2F_1+1}\begin{Bmatrix} J_2 & F_2 & I \\ F_1 & J_1 & k\end{Bmatrix}, \tag{D.4}$$

where $(J_2||T_k||J_1)$ is the reduced matrix element of T_k in the decoupled basis, and the quantity in the curly braces is a $6j$ symbol.

D.3 $E1$-$M1$ and $E1$-$E2$ transition amplitudes

In the following, summation over the magnetic sublevels M_n of the intermediate state is implied. The $E1$-$M1$ and $E1$-$E2$ transition amplitudes are

$$\begin{aligned} A_{b_1} &= 2\langle f|[(\mathbf{k}\times\boldsymbol{\epsilon})\cdot\boldsymbol{\mu}]\frac{|n\rangle\langle n|}{\Delta}(\boldsymbol{\epsilon}\cdot\mathbf{d})|i\rangle \\ &= i\left(\frac{2\mu_{fn}d_{ni}}{3\sqrt{2}\Delta}\right)k_{-M}(-1)^M\langle F_i M_i; 1q|F_f M_f\rangle, \end{aligned} \tag{D.5}$$

and

$$\begin{aligned} A_{b_2} &= \langle f|[i\{\mathbf{k}\otimes\boldsymbol{\epsilon}\}_2\cdot\mathbb{Q}]\frac{|n\rangle\langle n|}{\Delta}(\boldsymbol{\epsilon}\cdot\mathbf{d})|i\rangle \\ &= i\left(\frac{Q_{fn}d_{ni}}{2\sqrt{15}\Delta}\right)k_{-M}(-1)^M\langle F_i M_i; 1q|F_f M_f\rangle, \end{aligned} \tag{D.6}$$

degenerate transitions between like-parity states via two mechanisms: splitting of the intermediate state into non-degenerate sublevels, and mixing of the final state with nearby like-parity $J \neq 1$ states [81].

respectively. Here $\boldsymbol{\mu}$, $\mathbf{d}$, and $\mathbb{Q}$ are the magnetic dipole, electric dipole, and electric quadrupole moments of the atom.To derive Eqs. (D.5) and (D.6), we have assumed $\boldsymbol{\epsilon}\cdot\boldsymbol{\epsilon} = 1$, as is the case for linear polarization, and we have omitted a common factor of $(-1)^{I-F_f}$. Equations (4.29) and (4.31) follow from the definition $A_{\rm pc} \equiv A_{b_1} + A_{b_2}$.

D.4 Induced $E1$-$E1$ transitions

$E1$-$E1$ transitions may be induced by mixing of the states $|f\rangle$ and $|a\rangle$ due to both the electroweak interaction and Stark effect. The final state of the transition is the perturbed state $|f\rangle + \chi^*|a\rangle$, where χ is a small dimensionless parameter that depends on the details of the perturbing Hamiltonian. The amplitude for the induced $E1$-$E1$ transition is [53]

$$A_{E1-E1} = \chi\langle a|\boldsymbol{\epsilon}\cdot\mathbf{d}\frac{|n\rangle\langle n|}{\omega_{ni}-\omega}\boldsymbol{\epsilon}\cdot\mathbf{d}|i\rangle. \tag{D.7}$$

Here $\mathbf{d}$ is the electric-dipole moment of the atom and summation over the hyperfine levels and magnetic sublevels of the states $|n\rangle$ and $|a\rangle$ is implied.

In Eq (D.7), the quantity $\langle a|\cdots|i\rangle$ is the amplitude of the allowed degenerate two-photon $i \to a$ transition. It can be expressed as the contraction of two irreducible tensors:

$$\langle a|\boldsymbol{\epsilon}\cdot\mathbf{d}\frac{|n\rangle\langle n|}{\omega_{ni}-\omega}\boldsymbol{\epsilon}\cdot\mathbf{d}|i\rangle = \sum_{k,q}\{\boldsymbol{\epsilon}\otimes\boldsymbol{\epsilon}\}^*_{kq}\langle a|T_{kq}|i\rangle, \tag{D.8}$$

where

$$\{\boldsymbol{\epsilon}\otimes\boldsymbol{\epsilon}\}_{kq} = \sum_{\mu,\nu}\langle 1\mu;1\nu|kq\rangle\epsilon_\mu\epsilon_\nu, \tag{D.9}$$

is the tensor of rank $k = 0, 2$ formed by the dyadic product of $\boldsymbol{\epsilon}$ with itself, and T_{kq} is a tensor whose matrix elements we wish to express in terms of those of the dipole moment $\mathbf{d}$. Neglecting hyperfine splitting of the intermediate state, T_k commutes with $\mathbf{I}$. Then, since $J_i = 0$, we have

$$\langle a|T_{kq}|i\rangle = (-1)^{I-F_a+k}\frac{(J_a||T_k||J_i)}{\sqrt{2J_a+1}}\langle F_iM_i;kq|F_fM_f\rangle, \tag{D.10}$$

for $k = J_a$ and $q = M_a - M_i$. Using the WET to simplify the left-hand side of Eq. (D.8), we find

$$(J_a||T_k||J_i) = \frac{1}{\sqrt{3}}\frac{d_{an}d_{ni}}{\Delta}, \tag{D.11}$$

where $d_{fa} = (J_f||d||J_a)$ is the reduced matrix element of the electric dipole operator. When $k \neq J_a$, the matrix element $\langle a|T_{kq}|i\rangle$ vanishes. Therefore, only the tensor $\{\boldsymbol{\epsilon}\otimes\boldsymbol{\epsilon}\}_k$ of rank $k = J_a$ contributes to the $i \to a$ transition. Note that the tensor of rank $k = 1$ satisfies $\{\boldsymbol{\epsilon}\otimes\boldsymbol{\epsilon}\}_{1q} \propto (\boldsymbol{\epsilon}\times\boldsymbol{\epsilon})_q \equiv 0$, and hence the $J_i = 0 \to J_a = 1$ transition has zero amplitude, consistent with more general selection rules for degenerate two-photon transitions [34].

When the mixing of $|f\rangle$ and $|a\rangle$ is due to the electroweak interaction alone, the perturbation parameter is given by $\chi = \chi_{\rm W}$, where

$$\chi_{\rm W} = \frac{\langle f|H_{\rm NSD}|a\rangle}{\omega_{fa}} \equiv \frac{i\Omega_{fa}}{\omega_{fa}}, \tag{D.12}$$

for $F_a = F_f$ and $M_a = M_f$. Equations (4.44) and (4.30) follow from the definitions $\zeta_k \equiv (\Omega_{fa}/\omega_{fa})(J_a||T_k||J_i)/\sqrt{2k+1}$ for $k = J_a = 0, 2$.

In the presence of a static electric field $\mathbf{E}$, the perturbation parameter becomes $\chi = \chi_{\rm W} + \chi_{\rm S}$, where $\chi_{\rm W}$ is given by Eq. (D.12) and

$$\chi_{\rm S} = \frac{\langle f|H_{\rm S}|a\rangle}{\omega_{fa}}, \tag{D.13}$$

where $H_{\rm S} = -\mathbf{d}\cdot\mathbf{E}$ is the Stark Hamiltonian. In this case, $A_{E1-E1} = A_{\rm w} + A_{\rm s}$, where $A_{\rm w} \propto \chi_{\rm W}$ and $A_{\rm s} \propto \chi_{\rm S}$ are the amplitudes of the transitions induced by the electroweak interaction and Stark effect, respectively.

For a general $J = J_i \to J_f$ transition, the Stark-induced $E1$-$E1$ amplitude may have contributions from each of the irreducible tensors that can be formed by combining $\{\boldsymbol{\epsilon}\otimes\boldsymbol{\epsilon}\}_0 \propto (\boldsymbol{\epsilon}\cdot\boldsymbol{\epsilon})$ or $\{\boldsymbol{\epsilon}\otimes\boldsymbol{\epsilon}\}_2$ with $\mathbf{E}$. There are four such tensors: one each of ranks 2 and 3, and two of rank 1. However, for $J = 0 \to 1$ transition, only the rank-1 tensors contribute. These tensors are [115]:

$$\{\mathbf{E}\otimes\{\boldsymbol{\epsilon}\otimes\boldsymbol{\epsilon}\}_0\}_{1q} = -\frac{1}{\sqrt{3}}(\boldsymbol{\epsilon}\cdot\boldsymbol{\epsilon})E_q \tag{D.14}$$

and

$$\{\mathbf{E}\otimes\{\boldsymbol{\epsilon}\otimes\boldsymbol{\epsilon}\}_2\}_{1q} = \sqrt{\frac{1}{15}}[E_q - 3(\boldsymbol{\epsilon}\cdot\mathbf{E})\epsilon_q]. \tag{D.15}$$

Stark mixing of $|f\rangle$ with $|a\rangle$ gives rise to a Stark-induced amplitude whose dependence on applied fields is described by either the tensor in Eqs. (D.14) or the one in Eq. (D.15) depending on whether $J_a = 0$ or $J_a = 2$. The corresponding amplitudes are given by Eqs. (4.37) and (4.50), and the parameters ξ_0 and ξ_2 can be expressed in terms of the reduced dipole matrix elements by applying the WET to Eq. (D.7) with $\chi = \chi_{\rm S}$. This procedure yields Eqs. (4.38) and (4.51).